Numerical analysis of the head covers deflection and the leakage flow in the guide vanes of high head Francis turbines

Sølvi Eide

Department of Energy and Process Engineering,
Norwegian University of Science & Technology
Trondheim, Norway

This thesis is submitted to the Norwegian University of Science & Technology in partial fulfilment of the Ph.D. degree.

June 22, 2004

Abstract

This thesis includes a brief presentation of the different losses developed in high head Francis turbines, where special attention is paid to the losses in the guide vanes due to the head covers deflection. The different factors determining the extent of the leakage flow are thoroughly examined. Also, since the guide vane facing plate and the head covers are exposed to serious wear due to the presence of sand particles in a high accelerating flow, efficiency measurements of sand eroded and repaired turbines are presented. In addition, results from efficiency measurements of Francis turbines with different clearance gaps are included to underline the severity of the clearance gap between the covers and the guide vanes.

The thesis presents a numerical approach to calculate the head covers deflection. And the scope of this work is to develop a simplified 2-D model, which calculates the head covers deflection within a certain order of accuracy. Thus a 3-D modelling of the head covers deflection is also included with the purpose of validating the 2-D modelling.

Furthermore, a discussion of the efficiency with respect to the design of the head covers is performed to describe the potential of increasing the hydraulic efficiency by altering the design method.

Also, a numerical computation of the leakage flow in the guide vanes due to the head covers deflections, is presented to better visualize the effect from the clearance gap between the head cover and guide vane facing plate. Also, to underline the severity of large clearance gaps, the guide vane has been modeled with four different sized clearance gaps. Finally, an analytical interpretation of the leakage flow is included to evaluate the numerical calculation of the leakage flow.

Acknowledgements

The work presented in this thesis has been performed at the Hydro Power Laboratory, Department of Energy and Process Engineering at the Norwegian University of Science and Technology (NTNU).

I would like to express my sincere thanks to supervisor professor Hermod Brekke for initiating this study and for giving valuable guidance throughout the entire study.

I also wish to thank Ph.D Per-Egil Skåre at Sintef Energy Research and Hans Aunemo at GE Hydro for valuable guidance and suggestions concerning the work. In addition, Eirik Bøkko at Kværner, Gisle Rangnes and Henning Lysaker at Ge Hydro have been very helpful in providing the necessary data and technical drawings needed to fulfill the work, and must be thanked. I would also like to thank Harald Hulaas and Geir Brænd at Sveco Grøner for including me in efficiency measurements on site.

I am grateful to my former and present colleagues at the Hydropower laboratory. They have been of great importance with valuable comments and suggestions concerning my work as well as contributing to a very good social environment, which gave inspiration to carry through the work. Big thanks goes to: Professor Torbjørn Nielsen, Morten Kjeldsen, Ole Gunnar Dahlhaug, Jan Tore Billdal, Arne Kjølle, Peter Chapple, Gotfred Berntsen, Anna L. Martinsen, Åshild Rian, Kjell Roger Finserås, Roar Vennatrø, Pingju Li, Bhola Thapa, Thomas Vekve, Abdel-Ilah Rhrich, Øyvind Haave, Silja Strømme, Kristin Pettersen, Øyvind Antonsen, Wenche Johansen, Joar Grilstad, Ellef Bakken, Trygve Opland and Bård Brendastrø.

Finally, I would like to thank The Research Council of Norway (NFR) for funding the project.

Nomenclature

Symbol	Description	Unit
H	Net available head, in water column	[m]
H_{st}	Gross pressure drop, in water column	[m]
H_{Stag}	Stagnation pressure, in water column	[m]
H_s	Suction head, in water column	[m]
$*H$	Height of the head covers	[m]
h	Pressure head, in water column	[m]
h_{st}	Static pressure head, in water column	[m]
h_c	Cool water pressure, in water column	[m]
j	Loss, in water column	[m]
c	Absolute velocity	[m/s]
w	Relative velocity	[m/s]
u	Circumferential velocity of the runner	[m/s]
z	Altitude	[m]
g	Gravity constant	[m/s^2]
E	Specific hydraulic energy	[J/kg]
Q	Flow rate	[m^3/s]
c_p	Specific heat	[J/kgK]
T	Temperature	[K]
r	Radius	[m]
D	Diameter	[m]
M	Torque	[Nm]
M_h	Torque from the hydraulic pressure	[Nm]
B	Height of the runner blade	[m]
n	Rotational speed of runner	[rpm]
p	Pressure	[N/m^2]
E	E-module	[N/m^2]
X	Number of ribs	[-]
t	Thickness of ribs	[m]

R_c	Centre of mass	[m]
Δz	Vertical translation	[m]
C	Centre of mass in figure 3–1	[-]
F_L	Force	[N]
l	Length of circular arc	[m]
F_t	Tangential force	[N]
F_r	Radial force	[N]
Re	Reynolds number	[-]
U	Longitudinal velocity	[m/s]
u^+	Dimensionless longitudinal velocity	[-]
U_τ	Friction velocity	[m/s]
y^+	Dimensionless distance from the wall	[-]
V	Velocity	[m/s]
L	Characteristic length scale	[m]
P	Power	[W]
d	Derivative	[-]
N	Number of pole pairs	[-]
r_c	Radius which denotes the end of the layrinth seal	[m]
K	Constant in equation 2.6	[m^2/s]
f	Net frequency	[rad/s]
k	Turbulent kinetic energy	[m^2/s^2]
x, y, z	Cartesian coordinates	[-]

Greek letters	Description	Unit
α	Inlet angle	[°]
β	Outlet angle	[°]
ρ	Density	[kg/m^3]
ρ_c	Variable in figure 3–1	[m]
η_h	Hydraulic efficiency	[-]
ω	Angular velocity of turbine runner	[rad/s]
θ	Angle	[°]
ε_r	Radial strain	[-]
ε_t	Tangential strain	[-]
ε	Turbulence dissipation rate	[-]
σ_r	Radial tension	[N/m^2]

σ_t	Tangential tension	[N/m^2]
μ	Viscosity coefficient	[Ns/m^2]
υ	Kinematic viscosity	[m^2/s]
φ	Angle of deflection	[^{o}]
τ_w	Wall shear stress	[N/m^2]
ζ	Loss coefficient	[-]
δ	Partial derivative	[-]
Δ	Finite segment	[-]

Subscripts Description

1	Inlet of the runner
2	Outlet of the runner
3	Outlet of the draft tube
Leak	Leakage
Nom	Nominal
i, o	Inner and outer

Abbreviations

FEM	Finite Element Method
CFD	Computational Fluid Dynamics
H.W	Head water
T.W	Tail Water

Introduction

The most common water turbines today are Kaplan, Francis and Pelton. The Francis and Kaplan turbines are reaction turbines, where both the drop in pressure from inlet to outlet and the impulse forces from changes in the direction of the relative velocity vectors, develop mechanical energy. The Pelton turbine, on the other hand, develops mechanical energy solely from the impulse forces created by the changes of direction of the velocity vectors. The choice between these turbines is first of all based on the net head and total flow. However, the final choice depends on several additional parameters such as price, efficiency, sand erosion and time of repair. The Francis turbine holds the highest peak efficiency, and the efficiency curve is also rather steep. Accordingly, the Francis turbine is best suited for continuous operation at or around peak efficiency. As opposed to the Francis turbine, both Pelton and Kaplan turbines possess a quite flat efficiency curve, and is better suited for variable load operation.

The water power plants are initially designed to give a continuous production at best efficiency point. But the last few years there has been a change in this production pattern. A continuous expansion of electrical cables to neighbour countries is defining a new marked for the water power industry, where the price of electricity is the most important parameter in governing the production pattern. This involves a more fluctuating and demanding production pattern. The water power plants operate at full load, best efficiency point as well as at part load, all depending on the electricity price, and at the expense of the utilization factor. As mentioned, the Francis turbine exhibits a quite steep efficiency curve, and

is therefore poorly suited for variable load operations, which in many cases characterize the production pattern today. This fact makes it even more important to aim for a better efficiency at part load for Francis turbines. The challenge is to improve the efficiency outside best efficiency point without suffering a loss in peak efficiency.

The losses in a Francis turbine constitute roughly of leakage flow, friction loss and impact loss. The total loss in a high head Francis turbine lies between 5-6% at peak efficiency. In which the leakage loss in the guide vanes amounts to 1.5%, and therefore constitutes to a rather large part of the total loss developed in a Francis turbine. This leakage flow does not only disturb the main flow in the guide vanes, but it also disturbs the flow in the runner. The leakage flow in the guide vanes arises due to the head covers deflection, which increases the gap between the guide vanes and the head cover, when it is pressurized. The extension of the gap is mainly a function of the net head and the stiffness of the head and bottom covers, but it is also significantly influenced by erosion due to presence of sand particles in the flow. The leakage flows through the gap from the pressure side to the suction side, disturbing the main flow at the suction side and consequently reduces the efficiency.

To improve the hydraulic efficiency by develop a new runner design involves complicated flow analysis to account for the interaction between the stay vanes, guide vanes and runner blades. However, since the loss in the guide vanes is highly dependent on the extent of the clearance gap between the guide vanes and the covers, there is a large potential to increase the hydraulic efficiency by simply increasing the stiffness of the covers. And thus allow for a smaller deflection of the covers. And since this improvement does not involve the complicated runner design, it is relatively easy to perform.

In order to emphasis the potential efficiency increase due to the reduced leakage, it is necessary to gain insight into the physics that govern the loss mechanism. A valuable tool in this process will be a proper numerical approach that will give accurate results without the demand of high computer power. When the loss mechanism is fully emphasized, the basis of increasing the efficiency is made.

Contents

Abstract iii

Acknowledgements v

Nomenclature vii

Introduction xi

1 Hydraulic losses in Francis turbines 1
- 1.1 The hydraulic efficiency 1
- 1.2 Losses in a Francis runner 3
- 1.3 Leakage flow in the guide vanes 8
  - 1.3.1 Pressure side and suction side 10
  - 1.3.2 The clearance gap 13
- 1.4 Concluding remarks 17

2 Numerical modelling of the head covers deflection 21
- 2.1 The forces acting on the head cover 22
  - 2.1.1 Static pressure distribution in the guide vane region 22
  - 2.1.2 Static pressure across the pump plate 25
  - 2.1.3 Static pressure distribution across the labyrinth seal 27
- 2.2 The 3-D numerical approach 28
  - 2.2.1 Modelling in Algor 28
  - 2.2.2 The results from the 3-D analysis 30
- 2.3 The 2-D numerical approach 36
  - 2.3.1 The stiffness of the 2-D model 37
  - 2.3.2 Results from the 2-D computation 37
- 2.4 Discussion of the numerical results 39
  - 2.4.1 2-D versus 3-D 40
  - 2.4.2 Dependence on the design 40

3 Design of covers 47
3.1 Stress in head and bottom cover 47
3.2 The Reynolds number 52
3.3 The stiffness of the head cover related to the efficiency 53
3.4 Deformation in terms of deflection and translation 54
3.4.1 The angle of deflection 54
3.4.2 The vertical translation 57
3.5 Remarks 60

4 Numerical modelling of the flow in guide vanes 63
4.1 Computational domain 63
4.2 Mesh 64
4.3 Boundary conditions 68
4.4 Flow condition & The solver setup 70
4.4.1 The Reynolds number 71
4.1.2 Determining turbulence parameters 75
4.2 Remarks 75

5 Results from the numerical modelling of the leakage flow 77
5.1 Results 78
5.1.1 The characteristic of the leakage flow 78
5.1.2 Comparison of the flow in the different clearance gaps 83
5.2 Validation 90
5.2.1 Convergence 90
5.2.2 Mesh 91
5.2.3 Solver 91
5.3 Analytical interpretation 94
5.3.1 Flow between two fixed plates 94
5.3.2 Shear stress in the clearance gap 98
5.4 Concluding remarks 103

6 Conclusions 105

7 Further work 107

Bibliography 109

A Paper presented at IAHR 2002 I

B Paper presented at IAHR 2004 XIII

List of figures

1–1 Energy trade at a hydro power plant. Figure from [1]..... 2
1–2 Loss distribution in a high head Francis turbine. Figure from [2]. 3
1–3 Secondary flow in the spiral casing. Figure from [3]. 4
1–4 Velocity diagram. Figure from [1]. 6
1–5 Contra rotation at full load and pro rotation at part load. Figure from [6]. 8
1–6 A principal sketch of the leakage flow in the guide vanes. Figure from [2]. 9
1–7 Energy conversion in a Francis turbine. Figure from [6]. 11
1–8 Pressure side and suction side. 12
1–9 Dry clearance between the guide vane and bottom cover. Figure from [1]. 13
1–10 Efficiency test with different clearance gaps. Figure from [8]. 14
1–11 Efficiency of sand eroded and repaired turbine. Figure from [2]. 16
1–12 Efficiency of a sand eroded and repaired turbine. Figure from [8]. 17
1–13 Efficiency measurements of a Francis turbine with and without sealing strip between the guide vanes and head cover. Figure from [2]. 18
2–1 Sketch of the lower plate of a head cover, illustrating the region where the guide vanes are confined. 22
2–2 A submerged turbine, illustrating the definition of the available head, H, and the suction head, Hs. Figure from [1]. 23
2–3 Velocity diagram of the flow in the guide vane channel. 24
2–4 Sketch of the lower plate of a head cover, illustrating the region

where the pump plate is confined..... 25
2–5 Pressure distribution across the pump plate..... 26
2–6 Sketch of the lower plate of a head cover, illustrating the region where the labyrinth seal is confined. 28
2–7 Two different mesh resolutions of 1/3 of a 2-D geometry, where the red part illustrates the region where the rib is located. 29
2–8 Mounting of the head cover to the stay ring. Figure from [1]..... 30
2–9 A sketch of the lower plate of a head cover illustrating the inner and outer radius of the guide vane shaft..... 31
2–10 The vertical displacement of the head covers at the outer and inner radius plotted versus the individual height of the head covers.. 31
2–11 The vertical displacement of the head covers at the inner radius plotted against the individual heights of the head covers, when prestressing is assumed. 33
2–12 Tension plot of the bottom surface of a random selection of head covers. 34
2–13 Magnitude displacement of the three first head covers in figure 2–12. 35
2–14 A displaced and indisplaced head cover. 36
2–15 The vertical displacement of the head covers at the outer and inner radius plotted versus the individual height of the head covers.. 38
2–16 Tension distribution from a 2-D computation. 38
2–17 Magnitude displacement of the same head covers as referred to in figure 2–16. 39
2–18 Displacement ratio between the 3-D and 2-D results. 40
2–19 Head cover with cylinder on the left and without cylinder on the right..... 42
2–20 Cylinder connected to the rib..... 42
2–21 Displacement ratio of the head covers in group 1. 43
2–22 Displacement ratio of the head covers in group 2. 44
2–23 Head cover with cylinder placed between the ribs. 45
3–1 Pressurized head cover illustrating the deformation of an infinite element. Figure from [3]. 48
3–2 Deformation of an element due to the deflection of the head cover. Figure from [3]..... 48

3–3 The relation between the radial and the tangential force, when the head cover is regarded as a ring. 50
3–4 Efficiency plotted against the Reynolds number. 53
3–5 The efficiency at full load plotted against the stiffness, $*H/H_{Nom}$, of the head cover. 54
3–6 Angle of deflection. 55
3–7 The deflection of the head cover plotted against the efficiency at full load. 56
3–8 Displacement at the outer radius plotted against the efficiency at full load. 57
3–9 Displacement at the inner radius plotted against the efficiency at full load. 58
3–10 The vertical displacement at the inner radius plotted against the relative stiffness, $*H/H_{Nom}$. 59
3–11 The vertical translation of a large and a small head cover. 60
4–1 Subdivisions of the near-wall region. Figure from [19]. 65
4–2 Grid resolution of the guide vane cascade. 67
4–3 Grid resolution of the stay vane cascade. 68
4–4 Computational domain of the guide vane cascade. 70
5–1 Vector plot of the magnitude velocity in the clearance gap of 1 mm. 78
5–2 Static pressure contour in the middle of the guide vane channel. 79
5–3 Guide vane shaft at the suction side and pressure side. 80
5–4 Cross flow at the suction side of the trailing edge, 1 mm. 81
5–5 Vector plot of the magnitude velocity in the middle of the 1 mm clearance gap. 81
5–6 Flow pattern 2.5 mm from the head cover, 1 mm clearance gap.. 82
5–7 Flow condition in the middle of the guide vane channel, 1 mm gap. 83
5–8 Vector plot of the magnitude velocity in the 0.25 mm clearance gap. 84
5–9 Vector plot of the magnitude velocity in the 4 mm clearance gap. 84
5–10 Flow condition 2.5 mm from the head cover, 0.25 mm clearance. 85
5–11 Flow condition 5 mm from the head cover, 4 mm clearance. 85

5–12 Particle traces coloured by velocity magnitude in respectively 0.25 mm and 1 mm clearance gap. 87
5–13 Particle traces coloured by velocity magnitude in respectively 2 mm and 4 mm clearance gap. 87
5–14 Velocity distribution in the 0.25 mm clearance gap on the left and 1 mm on the right. 88
5–15 Velocity distribution in the 2 mm clearance gap on the left and 4 mm clearance gap on the right. 88
5–16 Relative leakage flow plotted against the size of the clearance gap. 90
5–17 Particle traces coloured by velocity magnitude. Spalart-Allmaras on the left and k-ε model on the right. 92
5–18 Development of the magnitude velocity of the first particle drop, close to the guide vane shaft. 93
5–19 Development of the magnitude velocity of the second particle drop. 93
5–20 Development of the magnitude velocity of the third particle drop, close to the outlet of the guide vane. 94
5–21 Incompressible viscous flow between two fixed plates. 95
5–22 Sketch of a head cover illustrating the region where the shear stress is considered. 98
5–23 Static pressure distribution in the clearance gap..... 99
5–24 Calculated shear stress at the left and the shear stress obtained from the numerical calculation at the right..... 100
5–25 The ratio between the numerical shear stress and the second analytical calculation. 101
5–26 The x-velocity at respectively path 1 and path 2. 101
5–27 The y-velocity at respectively path 1 and path 2. 102
5–28 The z-velocity at respectively path 1 and path 2. 102

List of tables

4-1 Reynolds number in the different clearance gaps. 73

1 Hydraulic losses in Francis turbines

This chapter presents the different losses developed in high head Francis turbines. Hence the loss in generator and the head losses in pipelines and penstock will not be included in this presentation. The main objective is to emphasize one loss in particular, namely the leakage flow in the guide vanes, which contributes to a rather substantial part of the total loss developed in a Francis turbine.

The crucial factors which determine the extent of the leakage will be thoroughly discussed, and preventive steps to reduce this leakage will also be presented.

1.1 The hydraulic efficiency

The hydraulic turbine efficiency is defined as the ratio between the utilized energy and the available energy. The available energy is established by subtracting the total energy at the outlet of the draft tube from the total energy at the inlet of the runner. However, to get a better visual impression of the correlation between the energy trade and the losses developed in a hydro power plant, a principal sketch of a power plant illustrating the different losses is given in figure 1–1.

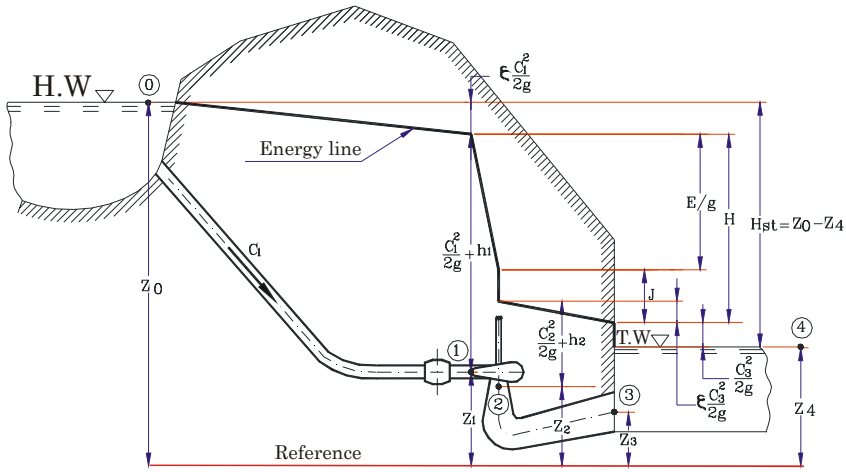

Figure 1–1: Energy trade at a hydro power plant. Figure from [1].

And by considering figure 1–1, the following expression of the available head is obtained:

$$H = \left(\frac{c_1^{\,2}}{2g} + h_1 + z_1\right) - \left(\frac{c_3^{\,2}}{2g} + h_3 + z_3\right) \tag{1.1}$$

Thus the final expression of the hydraulic efficiency is obtained from the following equation:

$$\eta_h = \frac{E}{gH} \tag{1.2}$$

Where the definition of the output, E, only accounts for the loss developed in the turbine and the loss in the draft tube due to back flow. By employing this definition, the head loss in the penstock and pipe lines due to friction and the outlet loss as the flow enters the draft tube are neglected. From figure 1–1 one can also relate the static pressure, H_{st}, to the available net head, H:

$$H = H_{st} - \zeta_1 \frac{c_1^2}{2g} - \frac{c_3^2}{2g} \tag{1.3}$$

The static pressure, H_{st}, is defined as the height difference between the head water and the tail water. The second term on the right hand of equation 1.3 corresponds to the head loss in the pipe lines and penstock, and the third term describes the outlet loss in the draft tube.

1.2 Losses in a Francis runner

In general, the loss developed in a high head Francis runner lies between 5-6% at best efficiency point [2]. The distribution of this loss from the spiral casing to the outlet of the runner is illustrated in figure 1–2.

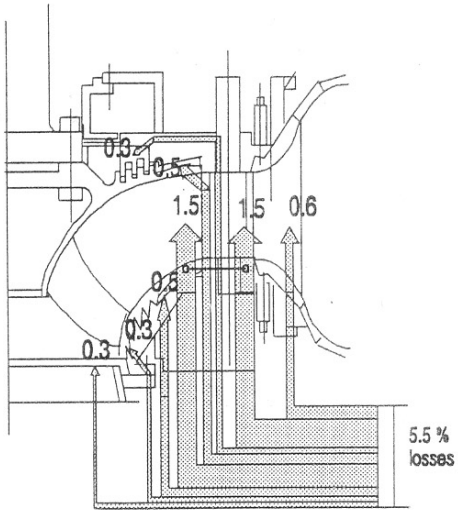

Figure 1–2: Loss distribution in a high head Francis turbine. Figure from [2].

The loss illustrated at the outer right in figure 1–2 corresponds to the loss developed in the spiral casing and the stay vane cascade. The flow condition in the spiral casing is a bit complex due to the viscosity along the wall. The viscosity sets up a boundary layer, which consumes energy from the

water to maintain its existence. Thus the static pressure in this region is lower than in the friction less region outside the boundary layer. This induces a secondary flow, because the water will flow from the higher pressure region to the lower pressure region in the boundary layer, as illustrated in figure 1–3. Unless the secondary flow is considered, it will propagate further through the stay vane and guide vane and worsen the flow field. But in most cases today a special design of the stay ring, as illustrated in figure 1–3, prevents the secondary flow to propagate further through the stay vane cascade. Still, at best efficiency point a loss of approximately 0.6% is developed in the spiral casing and in the stay vane cascade. This loss mainly consists of friction loss due to the roughness of the surface and impact loss due to the secondary flow at the inlet of the stay vane.

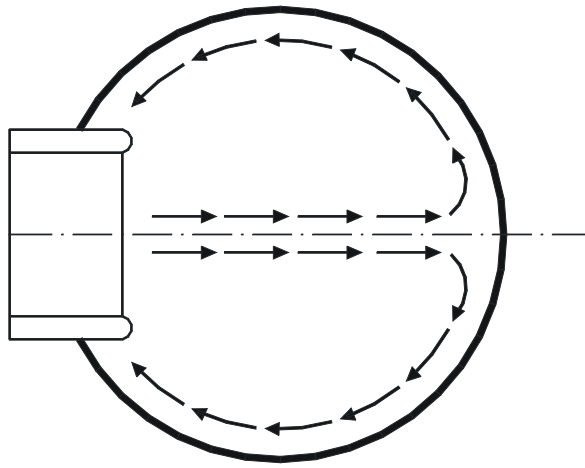

Figure 1–3: Secondary flow in the spiral casing. Figure from [3].

As the flow accelerates through the guide vane cascade, the efficiency is reduced by another 1.5% due to the leakage flow between the guide vane facing plate and the covers. There is also a leakage flow in upper and lower labyrinth seal which reduces the turbine efficiency by a total of 0.6% at best efficiency point.

The disc friction loss of 0.5%, on both sides of the runner, is due to the friction from the water between the stationary and rotational parts of the run-

ner. The friction force develops a moment in the opposite direction of the rotational speed, and consequently reduces the turbine efficiency.

Loss due to the existence of friction between the flow and surface of impact is often related to an increased temperature of the flow. In this particular case, a part of the available energy is used to increase the temperature of the water between the rotational and stationary parts, instead of being utilized by the runner. According to the law of convection, the relation between the required effect and the increased temperature is expressed in terms of the specific heat [4]:

$$j = \rho Q C_p \Delta T \tag{1.4}$$

However, numerous experiments have shown that any loss in power can also be related to the rotational speed in third potence [5]:

$$j = \zeta n^3 \tag{1.5}$$

Also, in the actual runner the friction between the water and the surface of impact further reduces the hydraulic efficiency. However, the hydraulic efficiency is obviously also quite sensitive to the direction of the relative velocity, w_1, at the inlet of the runner, because a bad inflow angle causes heavy impact losses. Considering the extent of the impact loss and the frictional loss in the runner at best efficiency point, the efficiency is further reduced by approximately 1.5%. However, at operation above peak load the inlet angle, α_1, has to be increased to allow for a larger flow. And as can be seen from figure 1–4, this alters the direction of the relative velocity at the inlet of the runner, resulting in an increased impact loss. This is also the case at operation below best efficiency point, where the inlet angle has to be decreased to obtain a lower flow. Compared to the relative velocity at best efficiency point, the reduction of the inlet angle causes the relative velocity to deflect towards the right, while an increased inlet angle causes the relative velocity to deflect to the left as can be seen by regarding the velocity diagram in figure 1–4.

Strictly theoretical, one can achieve a better adjustment between the relative velocity and the shaping of the runner blade, by changing the tangential velocity of the runner. And since the tangential velocity, u is related to the rotational speed, $n = 30u/\pi \cdot r$, which again is related to the net frequency, $f = N \cdot n/30$, it is impossible to change the tangential velocity with-

out altering the net frequency. However, since the turbine runs a synchronic generator, which is connected to a network with constant frequency, it is not feasible to obtain a different tangential velocity.

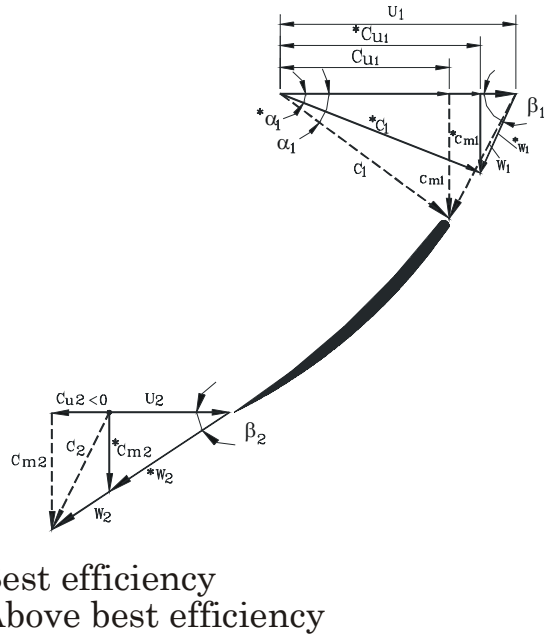

Figure 1–4: Velocity diagram. Figure from [1].

Furthermore, figure 1–2 indicates a loss at the outlet of the runner. The outlet of the runner is connected to a draft tube, with the sole purpose of converting the specific velocity energy to specific pressure energy. This is achieved by an increasing cross section towards the outlet of the draft tube. But, the actual outlet loss connected to the increasing cross section is not included in the definition of the hydraulic efficiency.

The loss developed in the draft tube due to back flow, is however considered when the hydraulic efficiency is calculated. And this loss is indicated at the outlet of the runner in figure 1–2. The loss due to the back flow in the draft tube is established according to the following formula:

$$j = \zeta \frac{c_3^2}{2g} \tag{1.6}$$

At best efficiency the loss developed in the draft tube reads approximately 0.3%.

However, at operation outside best efficiency point an additional loss is developed at the outlet of the runner. This loss is related to the development of swirl flow at off cam operation. The swirl flow origins as the value of the tangential absolute velocity, c_{u2}, attains a value different from zero. And by regarding figure 1–4 one can see that the absolute velocity, c_{u2}, has increased from zero at best efficiency point to a non zero value at full load. Also, by regarding figure 1–3, one can see that c_{u2} is negative and thus directed in the opposite direction of the circumferential speed, u_2, causing a contra rotation of the flow in the draft tube.

At part load a similar situation occurs when the inlet angle is reduced to obtain a lower flow. However, in this case the c_{u2} component is directed in the same direction as the circumferential runner velocity, causing a pro rotation of the flow in the draft tube, as shown in figure 1–5.

The swirl flow at the outlet of the runner is rotational energy which has not been converted to mechanical energy and therefore not been utilized by the runner[1], causing a reduction in the efficiency. The actual value of the rotational energy in water column is calculated according to the following formula:

$$j = c_{u2}^2 / (2g) \tag{1.7}$$

1. See chapter 1.3 for a further explanation of conversion of energy.

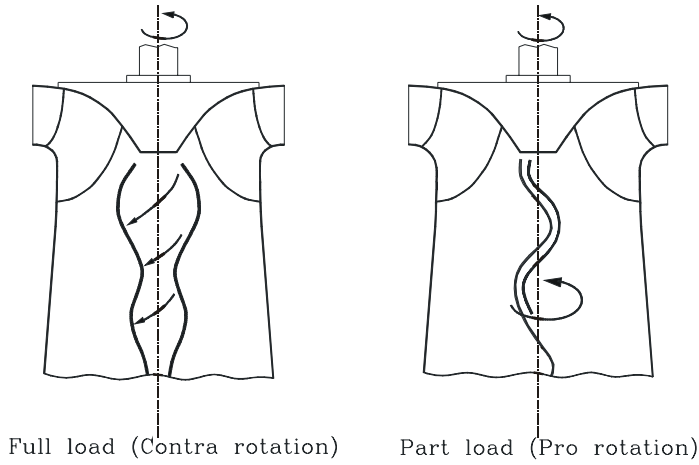

Figure 1–5: Contra rotation at full load and pro rotation at part load. Figure from [6].

The loss in efficiency due to the rotational velocity, c_{u2}, at the outlet of the runner can also be seen by regarding the definition of the hydraulic efficiency given in equation 1.8:

$$\eta_h = \frac{1}{gH}(c_{u1}u_1 - c_{u2}u_2) \tag{1.8}$$

From this equation one can clearly see that when c_{u2} equals zero the highest possible efficiency is achieved.

1.3 Leakage flow in the guide vanes

According to figure 1–2 the losses due to the leakage flow in the guide vanes represent a substantial part of the total loss in a high head Francis turbine. The leakage flows from the pressure side to the suction side and disturbs the main flow in the guide vane channel as illustrated in figure 1–6. The leakage flow also causes swirl flow at distinct regions in the clearance gap. This swirl flow has shown to induce heavy erosion on the facing

plates [7], as will be discussed later in this chapter. In addition, the leakage flow never enters the runner channel and therefore this part of the total flow is not utilized by the runner and the efficiency is reduced accordingly.

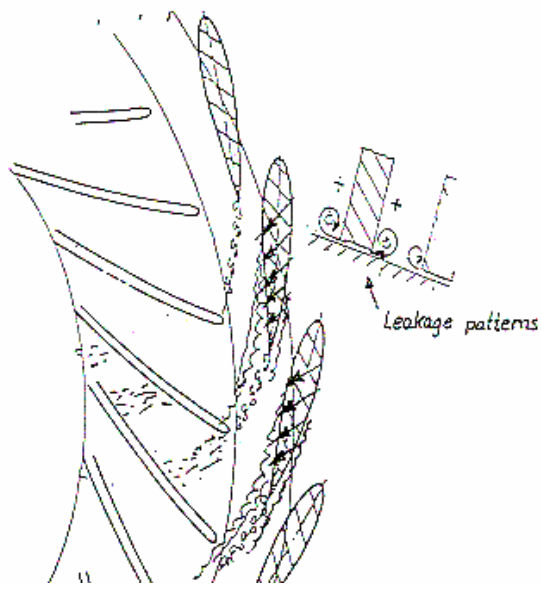

Figure 1–6: A principal sketch of the leakage flow in the guide vanes. Figure from [2].

However, the increased vortex flow and the disturbance of the main flow due to the leakage are found to have a greater impact on the efficiency than the actual loss of water. As mentioned above, the secondary flow disturbs the main flow in the guide vane cascade. But the secondary flow also influences the main flow at the inlet region of the runner vane, causing a bad inflow angle which induces impact losses at the inlet of the runner. Obviously, this flow condition reduces the hydraulic efficiency. However, since this loss is detected in the runner it is commonly defined as a loss which origins in the runner, despite the fact that the loss is actually caused by the leakage flow in the guide vanes. The loss distribution in figure 1–2 is no exception to this definition. Hence if the origin of the losses were to be accounted for in figure 1–2, the loss of 1.5% in the runner should be lower corresponding to an increased loss in the guide vanes. In other words, the

loss due to the leakage flow in the guide vane contributes to an even larger part of the total loss developed in the turbine.

The leakage flow is governed by the pressure difference between the suction side and pressure side, and by the extent of the gap between the guide vanes and the head and bottom cover.

1.3.1 Pressure side and suction side

The pressure difference between the pressure side and the suction side is closely connected to the development of rotational flow in the guide vanes. The rotational flow is recognized as the tangential component of the absolute velocity, denoted c_u. In order to understand the importance of obtaining a rotation of the flow, one has to consider the torque acting on the runner. The derived expression of the torque, M, acting on the runner is obtained from a closed volume consideration of a runner channel [6]:

$$\vec{M} = \rho Q(c_{u1}r_1 - c_{u2}r_2) \tag{1.9}$$

And as suggested above, equation 1.9 substantiates the importance of obtaining a rotation of the flow entering the runner channel, as the only velocity which contributes to the energy conversion in the runner is the tangential component of the absolute velocity. In equation 1.9 the terms involving the tangential component of the absolute velocity and the radius define the swirl flow. Thus in addition to regulate the flow entering the runner, the main purpose of the guide vane is to develop and obtain a swirl flow at the inlet of the runner.

As the importance of the existence of the swirl flow in the guide vane is emphasized a further investigation of the flow condition through a Francis runner is performed. And in order to illustrate the energy conversion, a diagram of the flow condition in the turbine from inlet guide vane to outlet draft tube is shown in figure 1–7.

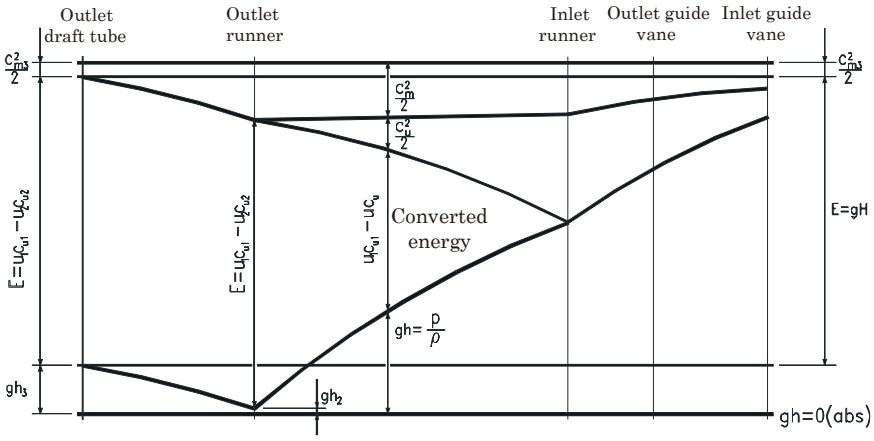

Figure 1–7: Energy conversion in a Francis turbine. Figure from [6].

From figure 1–7 one can see that the meridian velocity increases towards decreasing radius, as is expected according to the law of continuity. And due to the increasing value of the total absolute velocity as the water flows towards decreasing radius, the pressure energy must decrease according to Bernoulli equation. However, the development of the rotational energy places restriction to the design and orientation of the guide vanes. In figure 1–8 an axial view of a Francis turbine is illustrated to point out the orientation of the guide vanes compared to the runner vanes position at an open position of the guide vanes.

Furthermore, consider two points located at two different radii in the guide vane channel, as also shown in figure 1–8. Based on the prior discussion of the energy conversion through the guide vane, one can easily conclude that the pressure at point one must be higher than the pressure at point two, because point one is located at a larger radius than point two. Hence the pressure difference between the two points will pull the water at point one towards point two, giving rise to a secondary flow across the guide vane facing plate. Point one and two is respectively located at the so called pressure side and suction side of the guide vane.

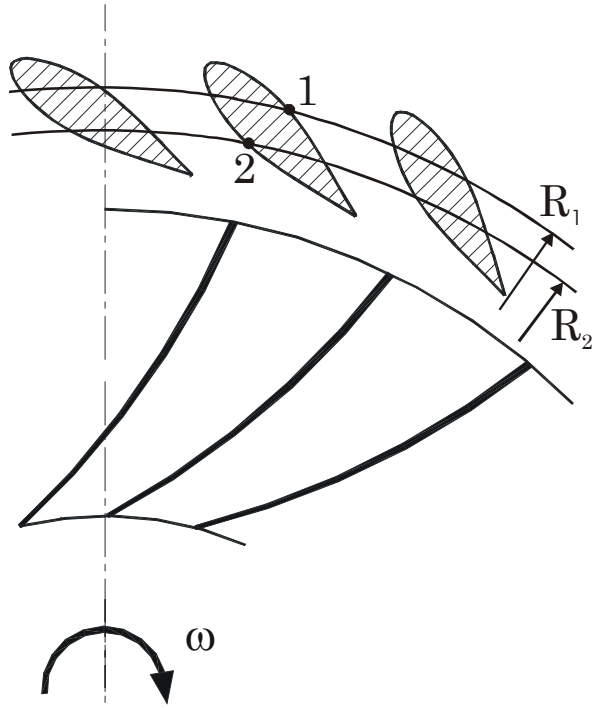

Figure 1–8: Pressure side and suction side.

Also, when the guide vanes lie in a different angle then the stay vanes the non-uniform velocity profile at the inlet of the guide vane is further amplified. Thus the pressure difference between the pressure side and suction side increases and accelerates the leakage flow.

Previous efficiency measurements, illustrated in figure 1–10 through figure 1–13, clearly show that the major losses in efficiency due to the clearance gap in the guide vanes occur for small guide vane openings. These measurements illustrate a higher improvement of the efficiency at part load compared to full load, when the clearance gap is decreased.

One reason to this is found by studying the pressure distribution across the guide vanes at different guide vane openings. At closed guide vanes the entire energy is converted to pressure energy, thus the velocity energy is

zero. Hence the pressure energy decreases by increasing guide vane openings. This means that the relative leakage flow through the guide vane clearance gap increases by decreasing guide vane opening, because the pressure drop across the guide vane profile is higher at smaller openings than at larger openings. The guide vanes are also positioned over a larger sand eroded area at part load compared to full load. Also, small guide vane openings form narrow channels with rough sand eroded surfaces, where high frictional losses occur from the high velocities. In addition, the leakage flow in the guide vanes also amounts to a larger part of the available energy at part load.

1.3.2 The clearance gap

When the head and bottom covers and the guide vanes are designed they are originally made with a certain clearance gap, as shown in figure 1–9, to prohibit grinding when the turbine is not pressurized.

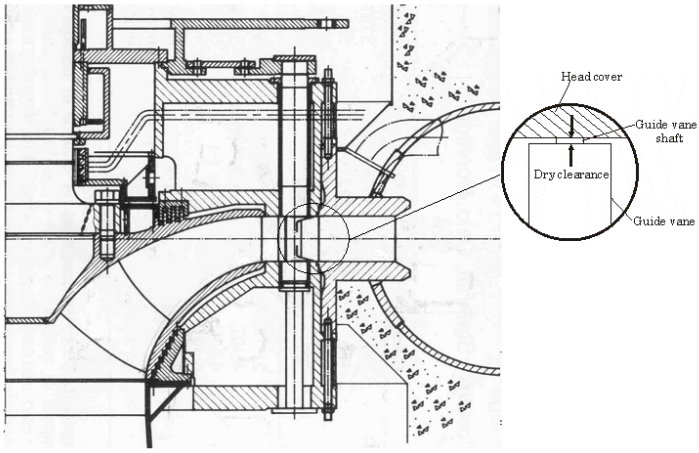

Figure 1–9: Dry clearance between the guide vane and bottom cover. Figure from [1].

But when the turbine is pressurized the originally gap, and hence the leakage flow increase. The efficiencys dependence on the extent of the clearance gap is clearly illustrated in figure 1–10, where the results from efficiency measurements at three different clearance gaps are presented.

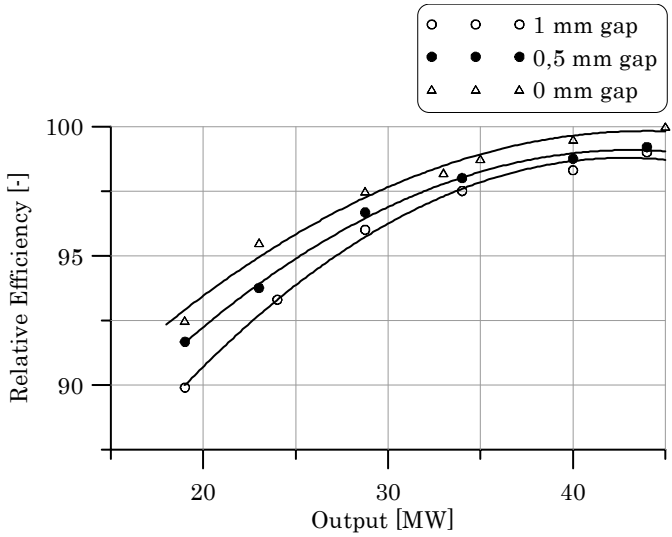

Figure 1–10: Efficiency test with different clearance gaps. Figure from [8].

From figure 1–10 one can see that at part load, the efficiency is decreased by approximately 2.5% as the size of the clearance gap is increased from 0 mm to 1 mm.

In general, the gap between the head cover and guide vane is highly dependent on the net head, but it is also influenced by the dimensions and the wear of the machinery. Especially high head Francis turbines are exposed to serious wear from sand erosion due to the high velocities and accelerations. The wear of the machinery caused by sand particles in the flow can make an uneven increased gap surface between the head covers and guide vanes, and further increase the gap.

In general, the presence of particles in a water flow usually cause abrasive degradation of hydraulic machinery components exposed to the flow. The deterioration of these parts may result in considerable reduction of performance and reliability of the water power plant. The higher number of repair periods due to the wear also decreases the total energy production. Consequently, abrasion should be considered and taken into account already at the design stage of the covers.

Wear due to abrasion primarily depends on the material of the exposed surface and the properties of the particles in the flow, such as geometrical shape, size and hardness. And the actual abrasive process on a surface is determined by the relative velocity and impact angle of the particle as it hits the surface [9]. The particle motion is further governed by the local flow pattern. As flow patterns significantly change within a turbine, knowledge of the local flow pattern is vital in order to predict the potential hydro abrasive wear. In particular, the abrasive wear is highly sensitive to vortex flow.

In the guide vane cascade one will find the highest acceleration and the highest absolute velocity in a Francis turbine. Correspondingly, the guide vane cascade is highly exposed to serious wear from sand erosion. In particular, the erosion of the facing plates underneath the edges of the guide vanes is enhanced by the vortex lines caused by the leakage flow. The wear from sand erosion further increases the clearance gap, which again enhances the vortex flow in the guide vanes and subsequently the erosion is further accelerated.

The clearance gap due to the water pressure alone, is minimal compared to the increased clearance gap when the guide vanes are subjected to sand erosion. The interaction between the erosion and the swirl flow is in fact bringing the extent of the clearance gap to a new level, where erosion of several millimetres has been observed [8]. Erosion due to the leakage flow has been detected on the suction side due to heavy vortex flow, but in addition wear at the inlet of the pressure side and at the outlet of the suction side has been observed due to local separation and turbulence [9].

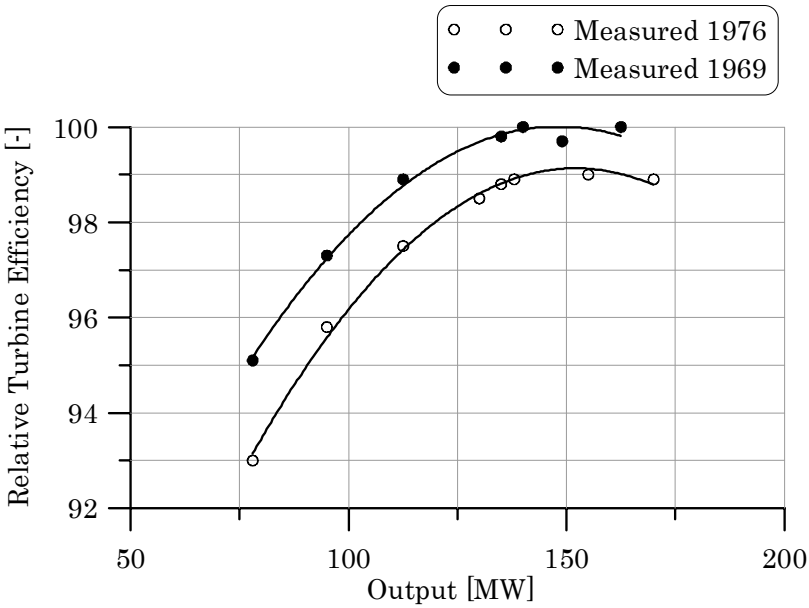

Figure 1–11: Efficiency of sand eroded and repaired turbine. Figure from [2].

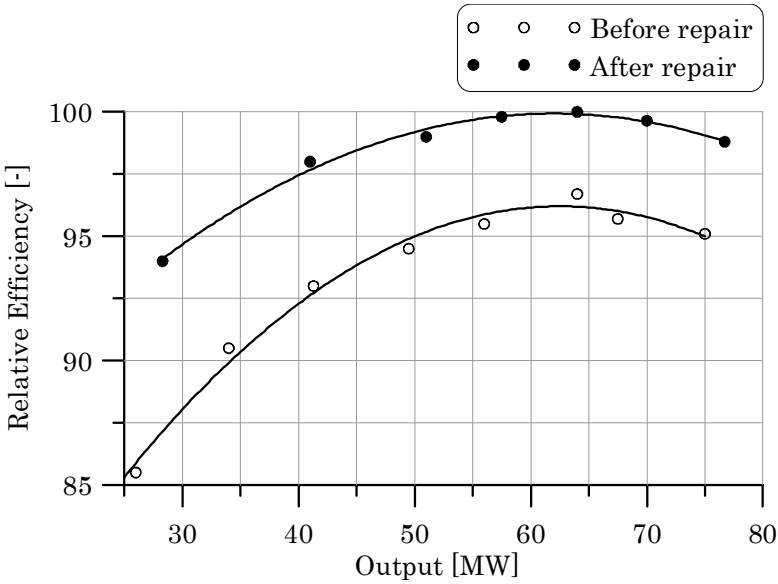

Figure 1–12: Efficiency of a sand eroded and repaired turbine. Figure from [8].

In figure 1–11 and figure 1–12 results from measurements of the efficiency of sand eroded and repaired turbines are presented to substantiate the importance of keeping the erosion on a minimum level. In figure 1–12 an improvement of 6-7% is achieved at part load as the turbine has been repaired. All in all, these results show that there are a lot to gain by avoiding erosion or at least do the proper repairs as heavy erosion are detected.

1.4 Concluding remarks

The loss in the guide vanes due to the leakage flow has been proven to consist of a rather substantial part of the total loss in a high head Francis turbine. Also, a great increase of the efficiency has been proven as the clearance gap between the covers and the guide vane facing plates has been reduced. Also measurements of sand eroded and repaired turbines have shown a great potential of increasing efficiency as the erosion is diminished. To minimize the degree of erosion smoothest possible accelera-

tion, reduction of the clearance gap between the guide vanes and the facing plates is recommended in general. But when the erosion is a fact, installation of guide vane seals in order to prevent the leakage flow will also reduce the erosion until the turbulence and secondary flow erosion have created a waviness surface between the seals and the facing plates. In figure 1–13 a plot of the efficiency with and without sealing strips is presented, and proves a substantial increase of the efficiency as sealing strips are employed.

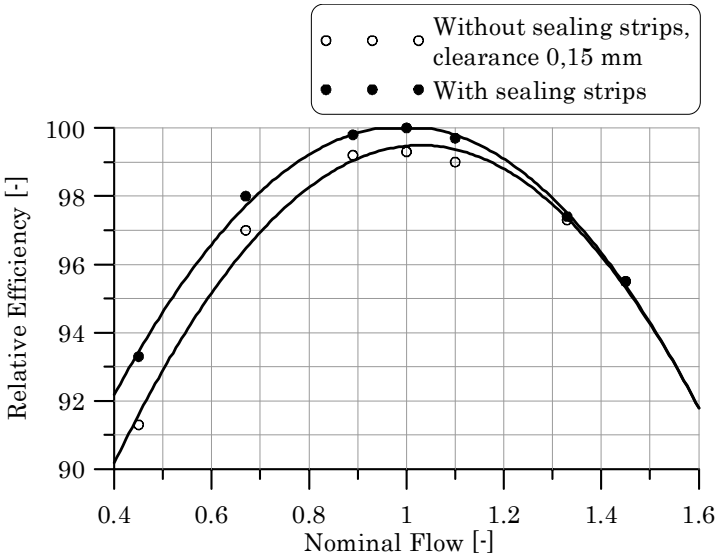

Figure 1–13: Efficiency measurements of a Francis turbine with and without sealing strip between the guide vanes and head cover. Figure from [2].

In addition, a careful choice of the stay vane outlet angles bringing the guide vane in a neutral position at the normal operation point is an important feature in order to achieve a uniform velocity profile at the inlet of the guide vanes.

Nevertheless, the best preventive step is to use materials with a certain hardness and particular the ceramic materials, or coatings on the material to avoid erosion of the surface. A lot of research has been directed towards the hardness of ceramic coatings and stainless steel [10]. And as an example the use of a ceramic coating of the guide vanes has been developed for

high head Francis turbines. It should however be emphasized that for a new turbine, because of the small clearance, one must be careful when coating the facing plates in order to obtain the necessary tolerances and surface finish.

In addition to choose the most suitable material, the choice of dimensions of the head and bottom cover is crucial to keep the gap below a certain critical value to avoid the large vortex flow, which induces erosion and further gap increase. By considering the severity of the leakage flow already at the design stage one can prevent or at least reduce unexpected costs from repairs and loss in production due to the secondary flow across the guide vane facing plate.

It should also be mentioned that there have been performed some experiments with tracks on the facing plates in order to break down the energy which leads the leakage from the pressure side towards the suction side [2].

The results presented in this chapter are the basis and the motivation for a further investigation of the head covers deflection due to the water pressure.

2 Numerical modelling of the head covers deflection

This chapter introduces a method to calculate the head covers deflection, when pressurized, by the use of the commercial software program Algor. Algor calculates current parameters like stress and displacement by the use of the Finite Element Method (FEM). The finite element method is a numerical procedure for analyzing structures and also continua. The differential equations, which describe the physical problem, are assumed to hold over a certain region. This region is divided into smaller parts, so-called finite elements. And instead of seeking approximations that hold directly over the entire region, the approximation is carried out over each element. And as the behaviour of all elements is established, these elements are patched together to form the entire region. Thus an approximate solution for the behaviour of the entire body is obtained [11].

A numerical computation of 20 different head covers has been completed, and the results are presented in this chapter. Furthermore, the head covers in questions are made by the same manufactures in order to rule out any differences due various design procedure. And even though the bottom cover is disregarded in this computation, the static pressure from the water obviously causes a similar deflection of the bottom cover. And the total clearance gap between the guide vane and covers increases accordingly. One should also bear in mind the fact that the additional translation due to the stay rings deformation is not included in this work. In any given design problem it is valuable to easily make changes of the geometry and effi-

ciently establish the significant results due to this change. And compared to a 3-D computation, the preliminary work involving a 2-D computation is much simplified, along with the heavily reduced computing time. Consequently, the main objective of this work is to develop a numerical 2-D approach which calculates the head covers deflection within a certain order of accuracy. Thus a 3-D modelling of the head covers deflections are also performed with the sole purpose of validating the accuracy of the 2-D approach.

2.1 The forces acting on the head cover

To simulate the head covers deflection one has to calculate the static pressure acting on the head cover. The static pressure decreases towards decreasing radius. However, the dependency on the radius is somewhat different in the guide vane cascade than across the pump plate. Accordingly, the guide vane cascade and the runner cascade have to be considered separately when the static pressure distribution is derived. In addition, the pressure drop across the labyrinth seals deviates from both the pressure development in the guide vane and across the pump plate. Thus additional calculation has to be derived concerning the pressure distribution across the labyrinth seals.

2.1.1 Static pressure distribution in the guide vane region

The region were the guide vanes are located is indicated by a thick solid line in figure 2–1.

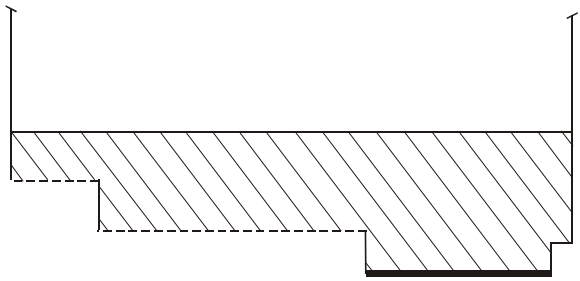

Figure 2–1: Sketch of the lower plate of a head cover, illustrating the region where the guide vanes are confined.

The purpose of the guide vane is to regulate the flow direction and the amount which flows towards the runner channel. According to the continuity equation the water in the guide vanes is accelerated as it moves towards a smaller radius. Consequently, a larger part of the net head is converted to velocity energy and the static pressure is reduced accordingly. Furthermore, no work is generated in the guide vane, which means that the entire static pressure is maintained and acts on the head cover. Consequently, the static pressure is simply obtained by subtracting the dynamic pressure from the stagnation pressure:

$$h_{St} = H_{Stag} - \frac{c^2}{2g} \tag{2.1}$$

The net or available head is only defined as the height difference between the head water level and tail water level minus the head loss in the pipe lines and the outlet loss in the draft tube. Accordingly, the submerging of the turbine, as shown in figure 2–2, is disregarded. Thus the stagnation pressure is defined as the summation of the net head and the submerging of the turbine.

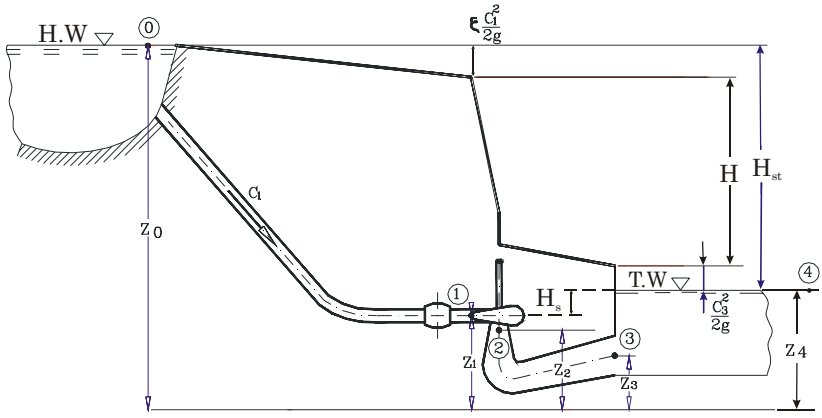

Figure 2–2: A submerged turbine, illustrating the definition of the available head, H, and the suction head, H_s. Figure from [1].

Furthermore, the value of the absolute velocity, c is calculated by means of the meridian velocity, c_m.

$$c = \frac{c_m}{\sin\alpha} \tag{2.2}$$

Whereas the meridian velocity is a function of the flow and is calculated according to equation 2.3:

$$c_m = \frac{Q}{2 \cdot \pi \cdot r \cdot B} \tag{2.3}$$

It should however be noted that the inlet angle, α, attains a constant value throughout the entire guide vane cascade, due to the constant swirl flow in the guide vane cascade[1].

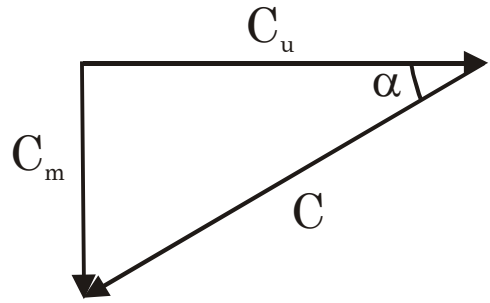

Figure 2–3: Velocity diagram of the flow in the guide vane channel.

The swirl flow may be expressed in terms of the meridian velocity, as can be read from figure 2–3. And the following expression is derived:

$$c_u \cdot r = \frac{c_m}{\tan\alpha} \cdot r = C \tag{2.4}$$

And by replacing the meridian velocity in equation 2.4 by the expression given in equation 2.3 the following relation is obtained:

1. The swirl flow, $c_u \cdot r$, attains a constant value because no forces are transferred in the guide vanes.

$$\frac{Q}{2 \cdot \pi \cdot r \cdot B \cdot \tan\alpha} \cdot r = \frac{Q}{2 \cdot \pi \cdot B \cdot \tan\alpha} = Const \qquad (2.5)$$

And since the value of Q/2πB in equation 2.5 amounts to a constant for a given geometry, α also must equal a constant value to fulfil the requirement of a constant swirl flow throughout the guide vane cascade.

Anyway, all the quantities on the right hand side of equation 2.3 are known factors, and the static pressure distribution may be established according to equation 2.1.

2.1.2 Static pressure across the pump plate

The region, in which part of the pump plate is confined, is illustrated by the thick solid line in figure 2–4.

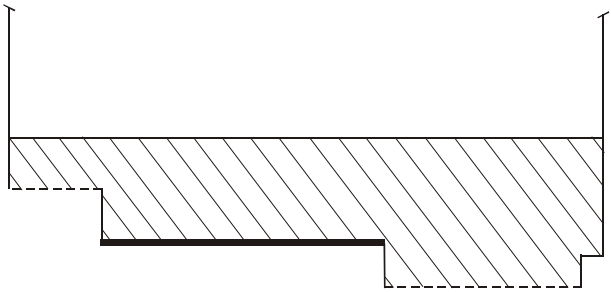

Figure 2–4: Sketch of the lower plate of a head cover, illustrating the region where the pump plate is confined.

As mentioned, the calculation of the static pressure distribution across the pump plate is somewhat different than in the guide vane region. As opposed to the guide vane channel, the pressure and velocity energy is converted to mechanical energy as the water flows towards the outlet of the runner. The mechanical energy is further transferred to the runner shaft, and work is generated accordingly. Consequently, a substantial part of the static pressure is utilized by the runner and does effect the head cover. And in order to establish the pressure distribution in this region an infinite fluid element is considered, as shown in figure 2–2.

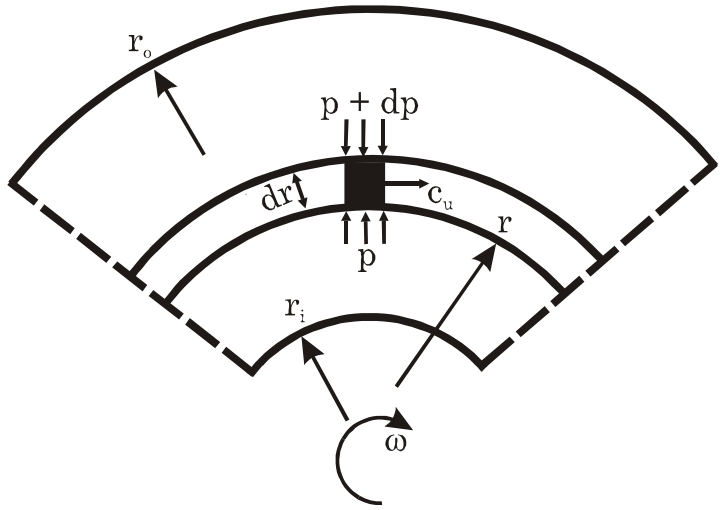

Figure 2–5: Pressure distribution across the pump plate.

According to Newtons second law the equilibrium of forces acting on the element are established as followed:

$$dp = \rho dr \frac{c_u^2}{r} \tag{2.6}$$

In equation 2.6 the term ρdr denotes the mass of the infinite fluid element and the second term, c_u^2/r, denotes the centripetal acceleration. And by dividing equation 2.6 by ρg, the pressure distribution is obtained in terms of meter water column:

$$\frac{\partial h}{\partial r} dr = \frac{c_u^2}{gr} dr \tag{2.7}$$

Numerous measurements have shown that the tangential component of the absolute velocity between the cover and the pump plate, lies between 0.5u-0.55u, where u is the circumferential velocity of the runner [6]. Also,

since the velocity of the runner can be expressed in terms of the angular velocity, $u = r \cdot \omega$, the following relation is derived:

$$\frac{\partial h}{\partial r} = \frac{K^2 \omega^2 r}{g} \tag{2.8}$$

where K lies between 0.5-0.55. The static pressure distribution is then extracted from equation 2.8 by integrating from inlet runner to the current radius:

$$\int_{h_i}^{h_1} dh = \frac{K^2 \omega^2}{g} \int_{r_i}^{r_1} r dr \Rightarrow h_1 - h = \frac{K^2 \omega^2}{2g} (r_1^2 - r_i^2) \tag{2.9}$$

The value of the static pressure, h_1, at the inlet of the runner is retrieved from the earlier calculation of the pressure distribution in the guide vane region. Accordingly, the pressure distribution from the inlet of the runner to the labyrinth seals can be found by solving equation 2.9 with respect to the unknown pressure, h. The pressure drop across the labyrinth seals on the other hand, develops in a more linear manner, and an additional pressure calculation has to be performed.

2.1.3 Static pressure distribution across the labyrinth seal

As opposed to the guide vanes and the pump plate the labyrinth seal is confined to a rather small area, as shown by the thick solid line in figure 2–6.

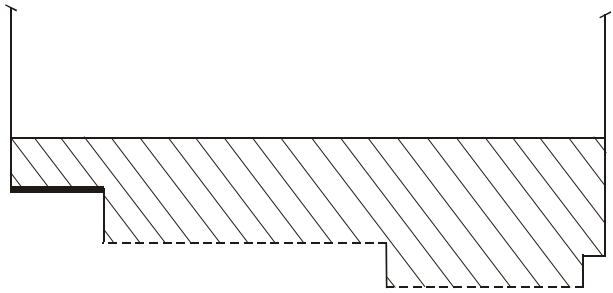

Figure 2–6: Sketch of the lower plate of a head cover, illustrating the region where the labyrinth seal is confined.

As mentioned, the pressure across the labyrinth seal drops in a more linear manner, and is a function of the radius until it attains the value of the cooling water pressure at the end of the seal:

$$h_{i+1} = h_i - \left(\frac{h_i - h_c}{r_i - r_c}\right) \cdot (r_i - r_{i+1}) \qquad (2.10)$$

And in accordance with equation 2.10 the pressure distribution across the labyrinth seals is then established.

2.2 The 3-D numerical approach

A presentation of the approach concerning the 3-D modelling is presented below, where the grid resolution and the boundary conditions are thoroughly accounted for.

2.2.1 Modelling in Algor

Two of the considered head covers are solid, while the rest of the head covers are made with ribs equal to the number of guide vanes. And since the non-solid head covers are made of 24 ribs, 1/24 of the entire head cover is modelled to give an axe symmetrical geometry. Correspondingly, a segment representing $360^o/\ 24 = 15^o$ of the geometry is modelled.

The demand of a fine mesh to get reliable results is diminished due to the fact that no large stress gradients are expected, apart from the region just around the connection to the stay ring. Nevertheless, two different mesh resolutions have been generated to substantiate this assumption. An example of the two different grid resolutions are shown in figure 2–7, where the finest mesh constitutes of twice as many grid cells as the coarse mesh. The results from the different mesh resolutions are compared, and resulted in a difference between 0-5 percent. However, when a mesh is refined with twice as many grid cells, then if the differences in results lie between 0-10 percent, a need for a refined mesh is superfluous [12]. Accordingly, the coarse mesh is chosen in order to reduce the computing time, but still maintaining the accuracy of the results.

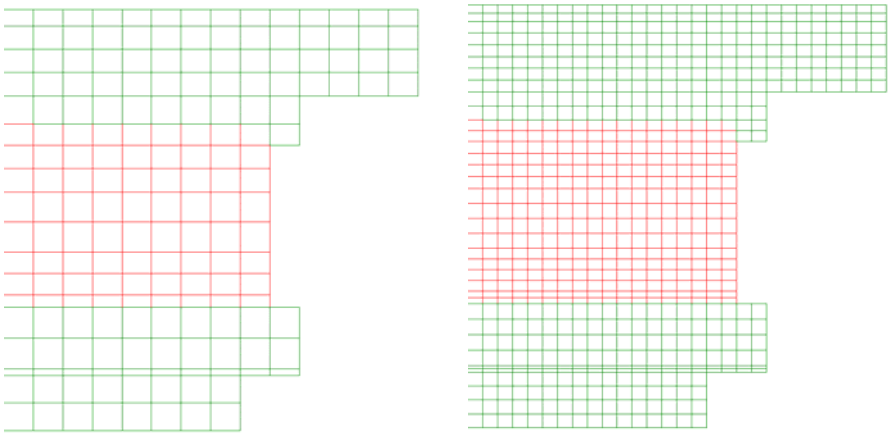

Figure 2–7: Two different mesh resolutions of 1/3 of a 2-D geometry, where the red part illustrates the region where the rib is located.

The head cover is connected only to the stay ring, at the outer part of the head cover, as shown in figure 2–8. The head cover is coloured in red and the stay ring is coloured in blue. And since the bearing has to absorb the entire water pressure, large tensions are expected in this area. The actual bearing is accounted for by employing a boundary condition at the outer part of the head cover, which only allows for translation in the radial direction. The importance of making the right boundary is underlined in Sølvi Eide et.al [13].

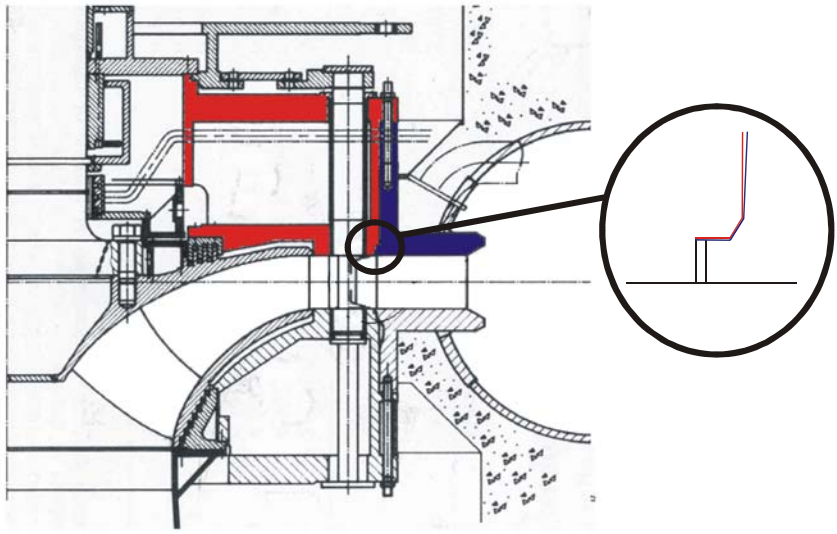

Figure 2–8: Mounting of the head cover to the stay ring. Figure from [1].

Since the 15 degree segment of the head cover represents an axe symmetrical part of the geometry, the cross section which separate two adjacent segments must be linked to each other by periodic conditions. But in Algor it is not possible to just define a periodic surface. Thus in order to simulate and obtain the periodic condition a boundary, only allowing for translation in the z-direction, is applied at the cross section.

Subsequently, the pressure distribution and the material properties are implemented, and Algor calculates deformations and stresses due to the static pressure acting on the head cover.

2.2.2 The results from the 3-D analysis

The region where the guide vanes are located is confined to approximately 1/3 of the head cover, as illustrated in figure 2–8. Thus only the displacement of this part of the head cover is of interest, when considering the leakage flow in the guide vanes. And in this particular case the translation at both the inner and outer radius of the shaft bolt is retrieved to obtain the

actual deflection of the head covers. The location of these points is illustrated in figure 2–9.

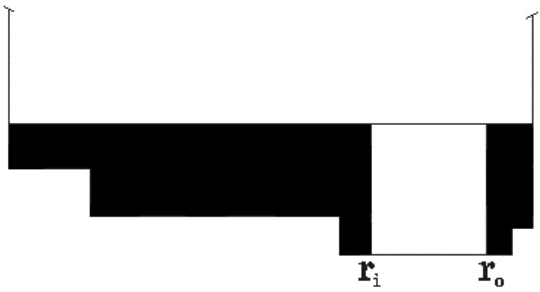

Figure 2–9: A sketch of the lower plate of a head cover illustrating the inner and outer radius of the guide vane shaft.

And from now on, the points representing the inner and outer radius of the guide vane shaft are only referred to as the inner and outer radius. The results from the 3-D numerical computation are presented in figure 2–10, where the absolute displacement at the inner and outer point is plotted versus the individual heights of the head covers.

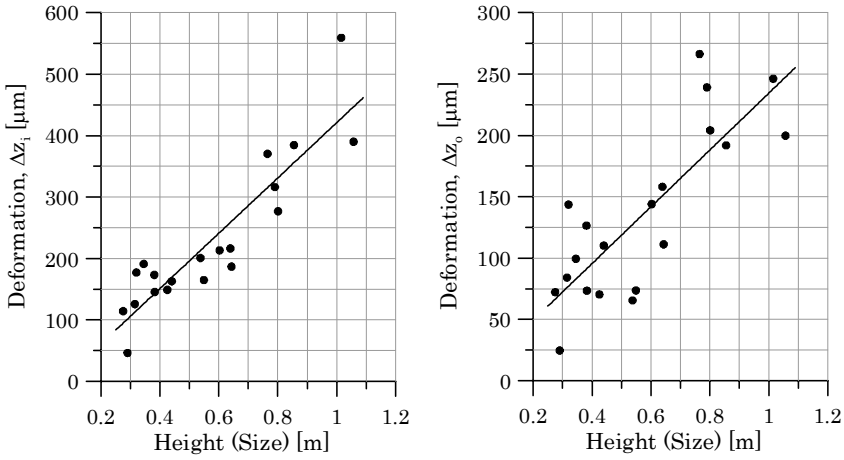

Figure 2–10: The vertical displacement of the head covers at the outer and inner radius plotted versus the individual height of the head covers.

The plot in figure 2–10 states that the absolute translation tends towards a linear behaviour with respect to the height of the head covers. Accordingly, the relative translation, defined as the ratio between the absolute translation and the height of the head covers, approaches a constant value. The solid line in figure 2–10 is a linear trend line, which is added to better illustrate the linear behaviour of the current plot.

The head covers, which are regarded in this thesis are connected to the stay ring at the upper part of the head cover, as illustrated in figure 2–8. And this geometry can cause quite large deformations, as illustrated in figure 2–10.

The deformation can be reduced if the head cover is prestressed against a facing flange on the stay ring at the bottom of the head cover, as illustrated in the enlarged part of figure 2–8. In this case the deformation at the outermost radius of the head cover is reduced to zero. However, during pressurizing and depressurizing of the turbine the prestressed surfaces will slide against each other, and thus the surfaces will gradually be worn down. This problem can be solved by a conical connection between the head cover and the stay ring.

In this work, prestressing of the covers has not been considered when the head covers deformations have been modelled. However, since the deformation at the outer region of the head cover should be zero with the right prestressing, the deformation obtained at the outer radius of the guide vane shaft has been subtracted from the deformation obtained at the inner radius. Thus the vertical deformation as the head covers are assumed prestressed is obtained.

Since the outer radius of the guide vane shaft is quite close to the region where the head covers have been prestressed, it is acceptable to employ the deformation at the outer radius of the guide vane shaft. The result is presented in figure 2–11 and shows a considerable decrease of the vertical deformation compared to the result in figure 2–11, which are based on no pre stressing and tightening of the covers. Thus there is a lot to gain by doing the proper prestressing. But in many cases this prestressing is avoided due to the high costs, which are involved in this procedure.

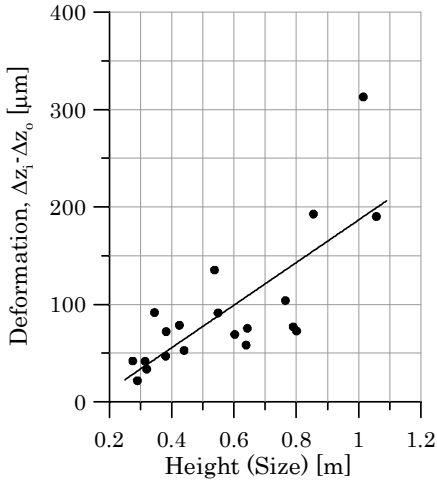

Figure 2–11: The vertical displacement of the head covers at the inner radius plotted against the individual heights of the head covers, when prestressing is assumed.

Furthermore, to substantiate the assumption of low pressure gradients, a tension contour of six pressurized head covers are shown in figure 2–12. The colour range in figure 2–12 is simply added to clarify which colours represent low tension and which represent high tensions. However, the absolute values attached to the colour range differ in each individual case. Also, the corresponding net head and volume flow is given for each individual head cover.

Only the tension at the bottom surface of the head cover is illustrated in figure 2–12. And as can be seen, the largest pressure gradients appear at the bearing, where the entire static pressure is absorbed. The low tension region in the middle of the surface, represented by the pink colour, indicates the increased strengthening of the geometry due to the ribs. And with the exception at the bearing, the tension gradient is quite low throughout the entire head cover.

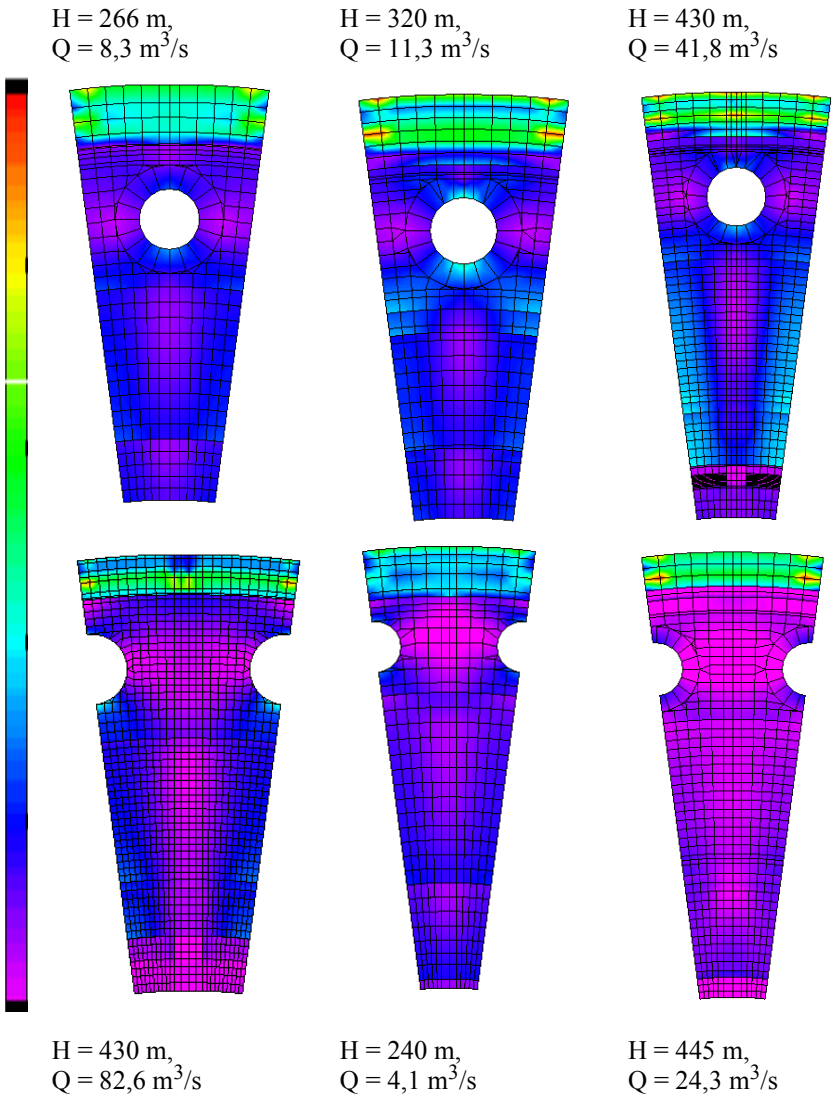

Figure 2–12: Tension plot of the bottom surface of a random selection of head covers.

Also, in figure 2–13 a contour plot of the magnitude displacement of the three upper head covers in figure 2–12 is shown.

.

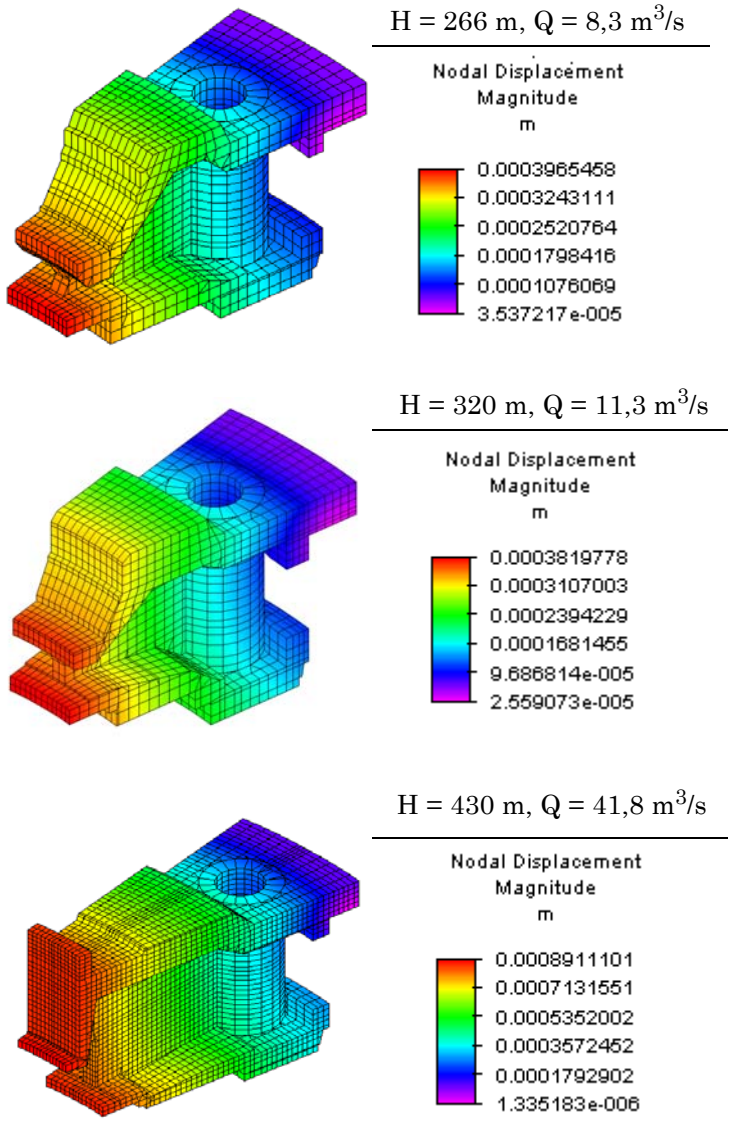

Figure 2–13: Magnitude displacement of the three first head covers in figure 2–12.

This plot indicates a linear behaviour of the displacement with respect to the radius, where the displacement increases with decreasing radius.

In order to get a visual feel of the deflection, the natural course of the displacement including the indisplaced state of the head cover is illustrated in figure 2–14. The green contours indicate the head cover prior to the pressurization. In this figure the actual displacement is scaled with a factor of 5 in order to improve the illustration. And as can be seen from this figure the entire head cover deflects a certain angle, φ, which will be further investigated in chapter 3.

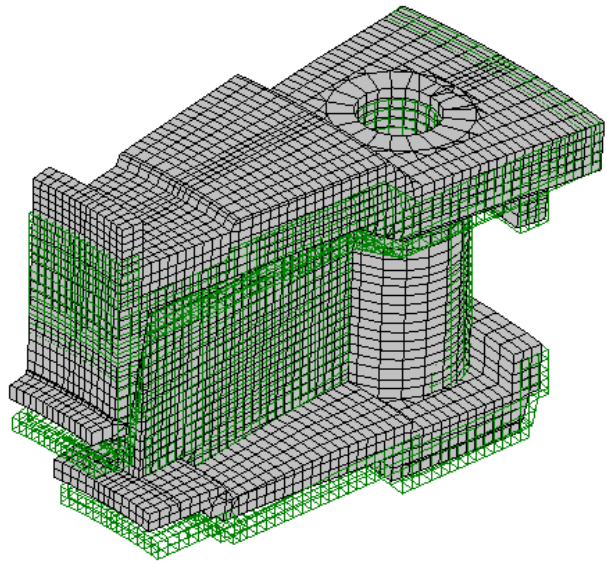

Figure 2–14: A displaced and indisplaced head cover.

2.3 The 2-D numerical approach

As mentioned in the last section most of the regarded head covers are not solid, but actually made with ribs equal to the amount of guide vanes. And in order to develop a complete 3-D model, which represented an axe symmetrical part of the head cover, a 15 degree segment had to be established.

Thus it seems impossible to develop a 2-D geometry, which represents an axe symmetrical part of the actual head cover. However, the challenge lies in obtaining an overall stiffness of the 2-D model corresponding to the actual stiffness of the 3-D geometry. And this can partially be achieved by manipulating the stiffness of the region where the ribs are located.

2.3.1 The stiffness of the 2-D model

As shown in figure 2–14, the ribs, with a certain thickness, are located in between two solid plates. And in order to establish a 2-D geometry with a stiffness corresponding to the actual stiffness of the 3-D geometry, a soft area is introduced in the 2-D model in the region where the ribs are located. This soft area is modelled with a somewhat lower E-module than the rest of the geometry, which is modelled with the E-module of the actual material. The calculation of the E-module of the soft region is based on how large part of the circumference the ribs occupy at certain radius, corresponding to the centre of mass:

$$E_{2-D,\,Soft} = \frac{X \cdot t}{2 \cdot \pi \cdot r_a} \cdot E_{3-D} \tag{2.11}$$

In addition, the hole where the guide vane shaft is running through is not included in the 2-D model, accordingly the 2-D model has a higher stiffness than the 3-D model in this region. Consequently, large simplifications are made when the 2-D model is developed. And the consequence from these substantial simplifications is important to emphasize in order to give a proper estimate of the actual displacement, based on the 2-D computations.

2.3.2 Results from the 2-D computation

In figure 2–15 the results from the 2-D computation are presented, and similar to the 3-D results, the magnitude displacement at the inner and outer radius are retrieved and plotted against the individual heights of the head covers. And in accordance with the 3-D results, the displacement increases linearly with increasing height of the head covers.

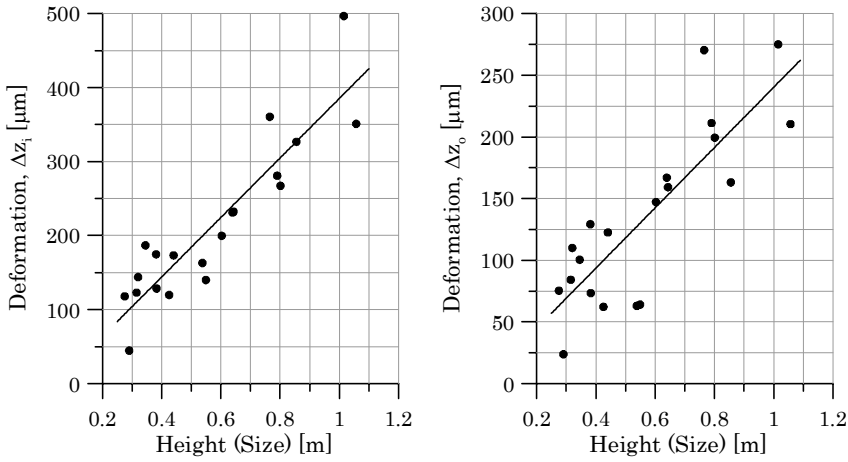

Figure 2–15: The vertical displacement of the head covers at the outer and inner radius plotted versus the individual height of the head covers.

Also, in figure 2–16 a tension contour of two head covers from the 2-D modelling is shown.

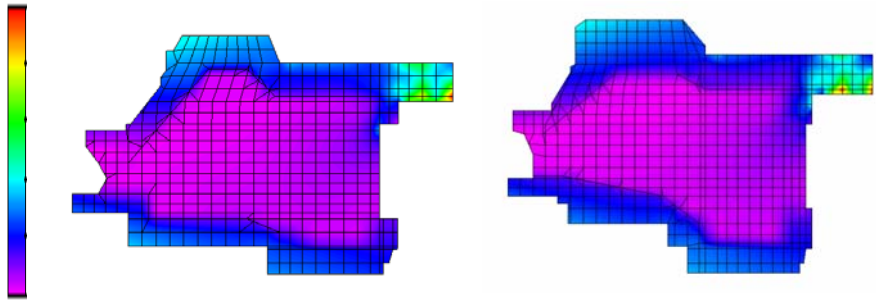

Figure 2–16: Tension distribution from a 2-D computation.

And in accordance with the 3-D results, the characteristic low tension gradient is present, with the exception at the bearing where the tension gradient is rather large due to the absorbance of the water pressure.

In addition, a contour plot of the magnitude displacement of the same head covers as shown in figure 2–16 is given in figure 2–17.

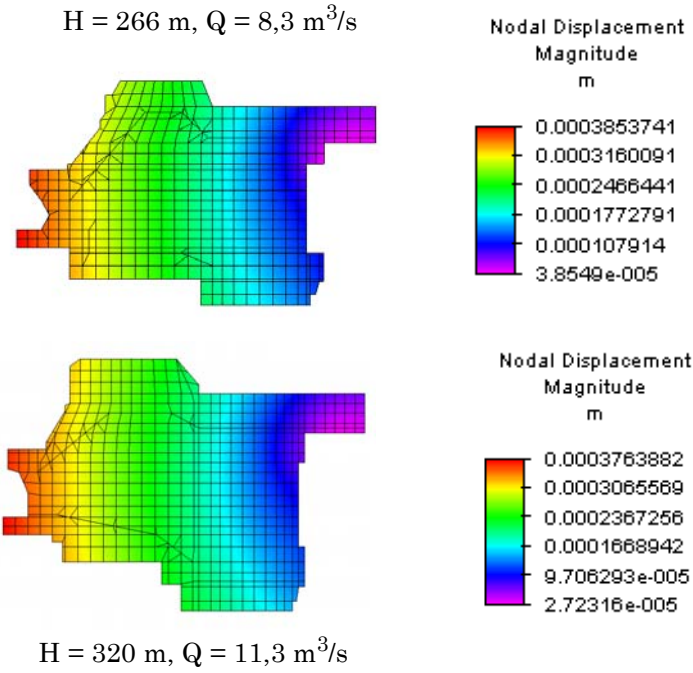

Figure 2–17: Magnitude displacement of the same head covers as referred to in figure 2–16.

Also this plot is in accordance with the results from the 3-D modelling. Hence the displacement increases linearly with decreasing radius.

However, in order to establish the accuracy of the 2-D results, a further investigation and comparison of the results from the different modelling approach are made in the following section.

2.4 Discussion of the numerical results

The main objective is to find a relation between the 3-D results and the 2-D results, in order to develop a reliable 2-D numerical approach with an appropriate error estimate.

2.4.1 2-D versus 3-D

Accordingly, the ratio between the translation results from the 2-D simulation and the 3-D simulation is calculated and presented in figure 2–18. It seems like the ratio roughly lies between 0.8-1.25. In the authors opinion this is a quiet high order of accuracy, especially when regarding the extensive assumptions which is made when the 2-D model is established. However, based on a further examination of the geometry, an attempt to improve the accuracy of the 2-D analysis is made.

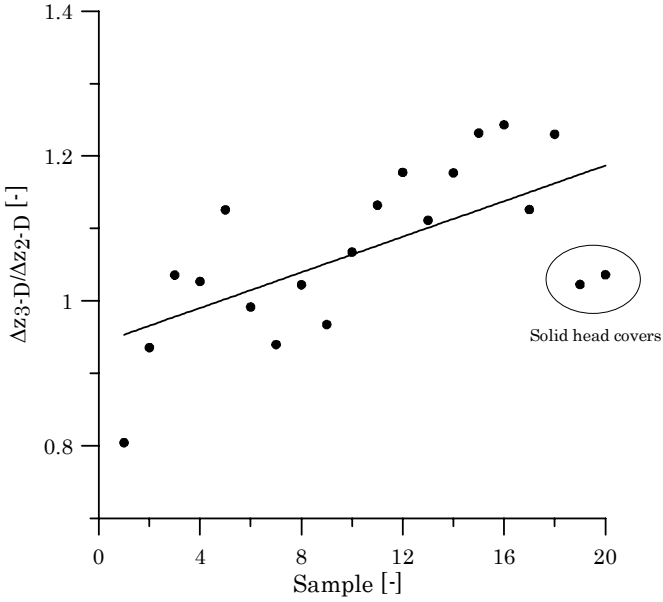

Figure 2–18: Displacement ratio between the 3-D and 2-D results.

2.4.2 Dependence on the design

To achieve a proper and accurate estimate of the displacement, based on the 2-D results, it is vital to understand the consequence of any simplification made when the 2-D model is developed. In this thesis some of the results presented show a quite large ratio between the 3-D and the 2-D computation. And this is not a surprising result regarding the extensive simplification which are made when the 2-D model is developed. However, many of the 2-D computations were in quite good accordance with the 3-D

results. And this scattering in results makes it difficult to estimate the head covers deflection with a high order of accuracy, based solely on the 2-D computation.

As pointed out earlier, the simplification of the ribs and the negligence of the bolt hole when the 2-D model is made, causes an obvious deviation between the 3-D and the 2-D results. And some extent of scattering in the ratio, depending on the design of the ribs and the dimensions of the hole, are also expected. But are there different fundamental design characteristics, which are the main source of the largest scattering?

Initially, the head covers were divided into solid and non-solid head covers, with the main purpose of dividing the head covers into different groups based on the resemblance between the 2-D and 3-D model. The ratio between the 3-D and the 2-D results of the solid head covers are expected to be low due to the high degree of similarity between the 2-D and 3-D model. The analysis of the solid head covers reported a higher displacement of the 3-D model than the 2-D model, corresponding to a ratio between 1.022-1.035. This can be explained by the fact that the bolt hole was neglected in the 2-D model, corresponding to an increased stiffness of the 2-D model compared to the 3-D model.

But in addition, an attempt to further divide the non-solid head covers into additional groups, based on its design, was performed with the intention of gathering head covers with similar ratio in one group. And a further analysis of the head covers geometry has shown that there are two special design which stand out, and which might be the reason for this great scatter in the ratio. Almost one half of the head covers are made with a cylinder surrounding the guide vane shaft, while the second half is made without this strengthening cylinder, as illustrated in figure 2–19.

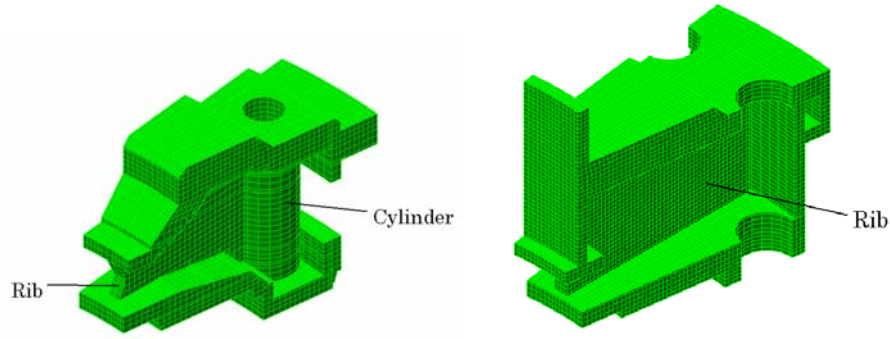

Figure 2–19: Head cover with cylinder on the left and without cylinder on the right.

The cylinders are connected to the ribs and are therefore regarded as an extension of the actual rib, corresponding to the diameter of the cylinder. The horizontal dotted lines in figure 2–20 illustrates the extension of the ribs, and from this figure one can see that approximately 1/2 of the cylinder is thereby considered when the stiffness of the soft area is calculated.

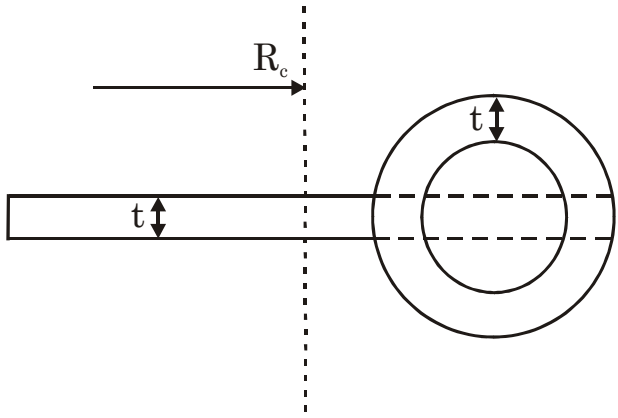

Figure 2–20: Cylinder connected to the rib.

Thus the cylinders are only partially accounted for when the 2-D model is made. In other words, the 2-D model is softer than the actual 3-D model due to the partially negligence of the surrounding cylinder. On the other hand, the 2-D model is also strengthen due to the negligence of the hole for the guide vane shaft. The interaction between these approximations is hard to predict. But by dividing the non-solid head covers into these two additional groups has made the internal scattering of the ratio between the 3-D and the 2-D results less, as shown in figure 2–21 and figure 2–22.

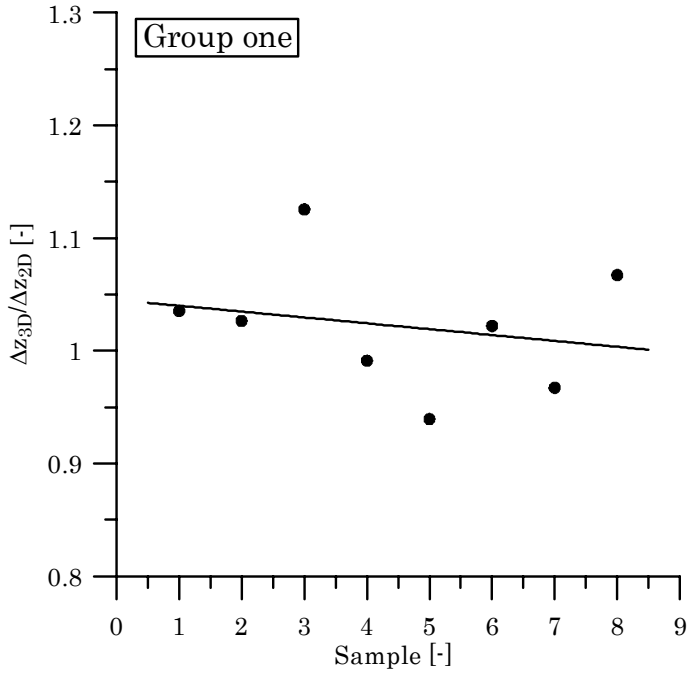

Figure 2–21: Displacement ratio of the head covers in group 1.

In figure 2–21 the ratio between the absolute displacement of the 3-D and 2-D computation is plotted. This plot is restricted to the head covers made with cylinders. And as can be seen from figure 2–21, the ratio in this group now only differs between approximately 0.95-1.15. As pointed out earlier, in this group it is hard to predict whether the 3-D or 2-D computations give the highest translations. This is because the partially neglected cylinder decreases the stiffness of the 2-D model, while the negligence of the bolt

hole increases the stiffness of the 2-D model compared to the 3-D model. Consequently, the final stiffness of the 2-D model depends on the extent of the individual simplification.

However, in the second group with no cylinder surrounding the guide vane shaft, only the bolt hole is not considered when the 2-D model is established. Thus the displacement results from the 3-D modelling are expected to exceed the displacement results obtained from the 2-D modelling. The ratio between the 3-D and the 2-D result is plotted in figure 2–22, and are in good accordance with the above assumption, as the ratio is confined only to 1.1-1.25.

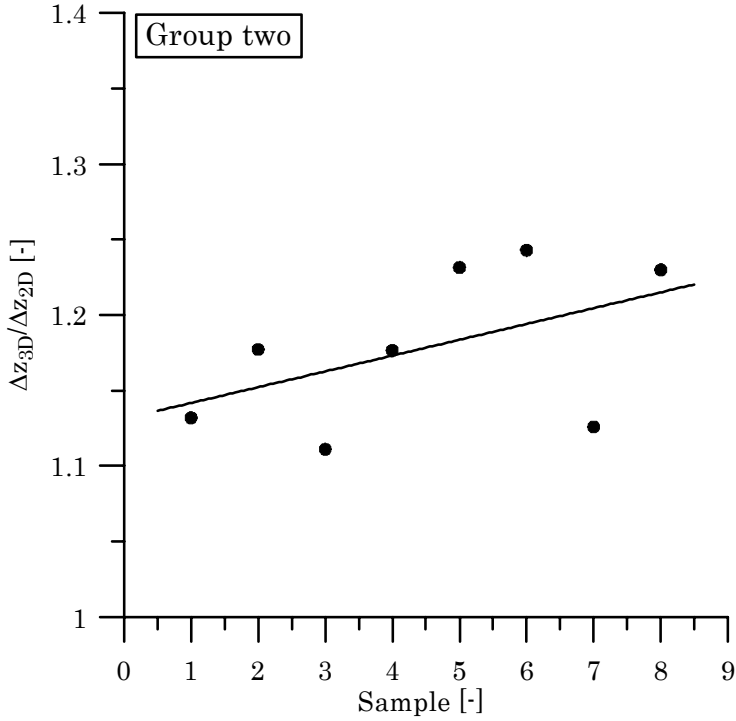

Figure 2–22: Displacement ratio of the head covers in group 2.

In addition to these two main classifications of the non-solid head covers, there are two other head covers which have a somewhat different design, which can not be represented by either of these two groups. These two head

covers also have a cylinder surrounding the guide vane shaft, but the placing of the guide vane shaft, and thus the cylinder, is different.

In this case the cylinders are placed between the ribs, as illustrated in figure 2–23.

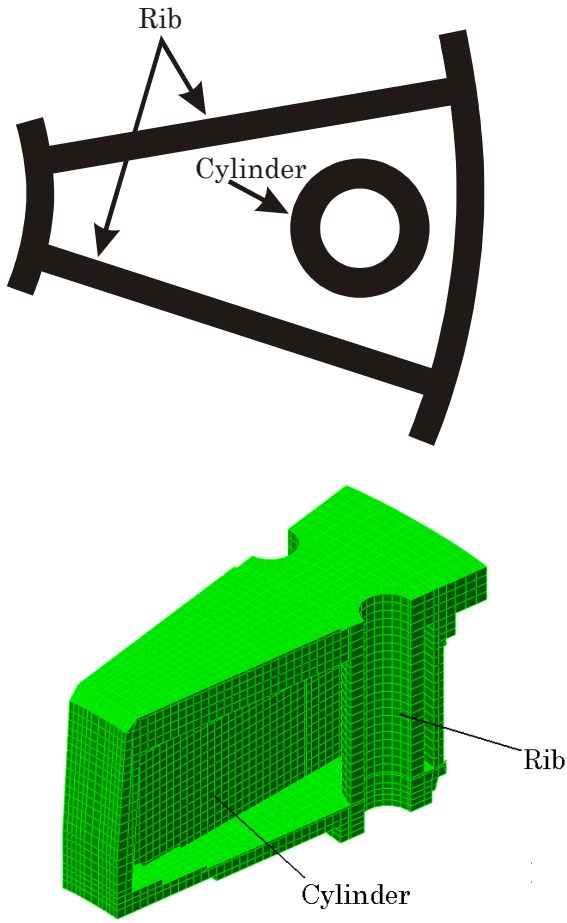

Figure 2–23: Head cover with cylinder placed between the ribs.

And since the cylinder is not a part of the rib, the cylinder is not considered when the E-module of the soft area is calculated. Correspondingly, the 2-D model representing this head cover design attains a lower overall stiff-

ness than the original 3-D model, when disregarding the absence of the shaft hole. However, the results from the numerical computation reported a higher translation of the 2-D model compared to the 3-D model, in both cases. These results underline that the decreased stiffness of the 2-D model due to the negligence of the cylinder is not balanced by the increased stiffness due to the absence of the shaft hole. This is not a surprising result when regarding the size of the cylinder compared to the extent of the neglected hole.

Based on these results one really can understand the importance and the advantage of distinguish between different kinds of design, when a simplified 2-D model is developed. Accordingly, a proper and more reliable estimate of the actual deflection, based on the 2-D result, is obtained. Anyway, a further investigation of the head covers deflection with respect to the design of the head covers is performed in the following chapter.

3 Design of covers

The guide vanes and the runner blades lie in between the head and bottom cover, and the main purpose of the covers are to keep the turbine together. Consequently, the covers must be quiet stiff to minimize the deformation due to the water pressure. The design of the covers is often based on an analytical calculation of the covers deflection. And this chapter presents the basis for such a simplified analytical method, which calculates the deflection of the covers due to the water pressure. Furthermore, a discussion of the design based on the FEM results is performed to emphasize any potential efficiency increase due to improved design of the covers.

3.1 Stress in head and bottom cover

The head and bottom covers are exposed to a substantial static pressure from the flow, causing a deflection of the covers. The total force acting on the head and bottom cover is absorbed by the bolts, which anchor the covers to the stay ring.

In figure 3–1 a principal sketch of a head cover is drawn to illustrate the deformation of the head cover due to the deflection. An element at distance ρ from the centre of mass is deflected, causing a radial displacement, Δr, of the element. In figure 3–2, a more detailed sketch of the actual displacement is shown to better obtain the relation between the external moment from the water pressure and the resulting angle of deflection.

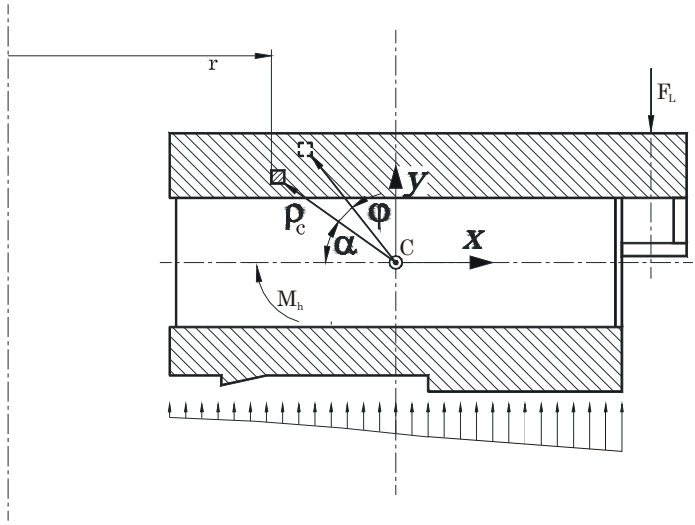

Figure 3–1: Pressurized head cover illustrating the deformation of an infinite element. Figure from [3].

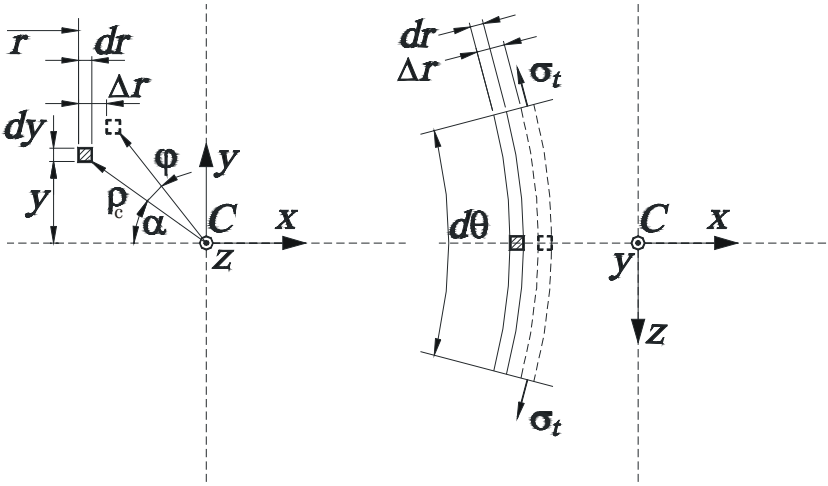

Figure 3–2: Deformation of an element due to the deflection of the head cover. Figure from [3].

As the cover is deflected, an element of the cover is displaced some angle, φ, which contributes to a radial movement Δr. And according to figure 3–2 the following relationship can be made:

$$\Delta r = \varphi\rho\sin\alpha = \varphi y \tag{3.1}$$

Furthermore, the radial strain is derived by the following relation:

$$\varepsilon_r = \frac{\Delta r}{r} = \frac{\varphi y}{r} \tag{3.2}$$

The radial strain generates a tangential strain. And in figure 3–2 a segment dθ of the entire head cover is considered. Hence the length of the circular arc, which defines the circumference of the segment is given by l = rdθ. Hence the tangential strain obtained from the chain rule reads [14]:

$$\varepsilon_t = \frac{\Delta l}{l} = \frac{\Delta r \cdot d\theta + r \cdot \Delta(d\theta)}{r \cdot d\theta} \tag{3.3}$$

Since the cover only experience radial deformation, the value of the tangential deformation, Δ (dθ), equals zero. Thus based on equation 3.3 the radial strain equals the tangential strain, $\varepsilon_t = \varepsilon_r$. The tangential stress is then calculated by means of Hook's law [15]:

$$\sigma_t = E\varepsilon_t = \frac{E\varphi y}{r} \tag{3.4}$$

Consider an infinite element with length dr and height dy, then the tangential force yields:

$$dF_t = \sigma_t \cdot dr \cdot dy \tag{3.5}$$

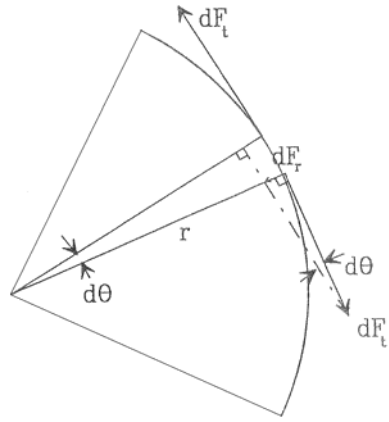

Figure 3–3: The relation between the radial and the tangential force, when the head cover is regarded as a ring.

The correlation between the radial and the tangential force can be derived by considering figure 3–3, where $d\theta << 1$. Thus $\tan\theta = \theta$ [14]. Hence the radial force on an infinite element with tangential extension then yields:

$$dF_r = dF_t \cdot d\theta = \sigma_t \cdot dr \cdot dy \cdot d\theta \tag{3.6}$$

The radial force establishes a moment about the center of mass and is given by:

$$dM_h = ydF_r = \sigma_t y dr dy d\theta = \frac{E\varphi y^2}{r} dr dy d\theta \tag{3.7}$$

The value of the total moment acting on a certain extension, $\theta = [0, 2\pi/Z]$ of the cover is found by integrating equation 3.7:

$$M_h = \int_0^{\frac{2\pi}{Z}} \int_{r_i}^{r_y} \int_{y_1}^{y_2} \frac{E\varphi y^2}{r} dy dr d\theta \tag{3.8}$$

Since the cover is not continues in the y-direction the integral with respect to y is replaced with a summation sign, and the final expression is then given by:

$$M_h = \frac{2\pi E\varphi}{3Z} \sum_{i=1}^{n} \int_{r_{ii}}^{r_{iy}} \frac{(y^3_{i2} - y^3_{i1})}{r} dr \tag{3.9}$$

And by use of some mathematical relations the angle of deflection can be found from the following expression [16]:

$$\varphi = \frac{3M_h Z}{2\pi E \sum_{i=1}^{n} \left((y^3_{i2} - y^3_{i1}) \ln\left(\frac{r_2}{r_1}\right)\right)} \tag{3.10}$$

The accuracy of this equation is well accepted when the following condition is fulfilled [14]:

$$\frac{r_y}{r_i} < 1{,}5 \tag{3.11}$$

This analytical calculation is based on ring deformations and thus neglects the shear and bend deformation of the covers, but when the shear and bend stresses are accounted for the actual deflection is 1.5-2 times higher than the result obtained from the simplified stress calculation [17]. A final numerical calculation is usually carried out by means of a finite element method.

It should however be mentioned that the disturbance from the leakage flow in the guide vanes reduces the efficiency even more for high head Francis turbines compared to low head Francis turbines. This is most likely due to the fact that the height of the guide vanes in high head turbines is much lower than for a low head turbine. Correspondingly, the leakage flow disturbs a larger part of the main flow. The long runner blades in high head Francis turbine also make the runner more sensitive to local disturbances. In addition, the guide vane opening for a high head Francis turbine is also smaller than for a low head turbine, making the pressure difference between pressure side and suction side larger than for a low head turbine [2].

Accordingly, the design criteria of the covers for high head an low head turbines differs. As a rule when designing the covers the angle of deflection for high head Francis turbines should be less than $5 \cdot 10^{-4}$ radians, but for low head Francis turbines it is sufficient to keep the deflection below $8 \cdot 10^{-4}$ radians [3].

In general, one can say that according to the design criteria the deflection should decrease with increasing unit size. In the following sub-chapters a discussion of the efficiency and the deflection with respect to unit size is performed to fully examine the presented design criteria. However, since the design criteria depends on the size of the turbines, a parameter describing the size has to be introduced. And in this case the Reynolds number is employed to express the dimensions of the regarded turbines.

3.2 The Reynolds number

I order to distinguish between the different sized turbines, the Reynolds number is often employed. The Reynolds number for a Francis turbine is a function of the outlet diameter of the runner and the velocity at the outlet of the runner:

$$Re = \frac{v_2 \cdot D_2}{\nu} \tag{3.12}$$

According to equation 3.12 the Reynolds number increases by increasing unit size. The Reynolds number of the 20 Francis turbines referred to in this thesis is calculated, and plotted against the best efficiency in figure 3–

4. The plot clearly indicates that the efficiency increases by increasing Reynolds number. Thus the efficiency increases by increasing unit size. This relation can be explained by comparing the friction loss in a small and large Francis turbine unit. Since a larger percentage of the flow in a small runner is in contact with the surface than in a larger runner, the friction loss in percentage is higher in a smaller unit than in a larger unit.

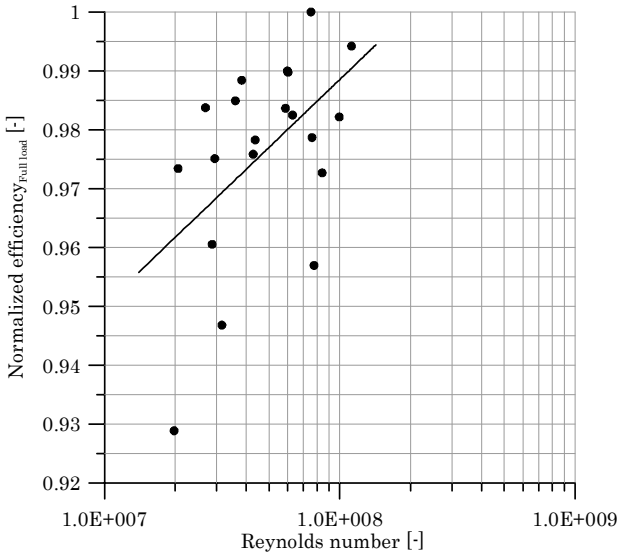

Figure 3–4: Efficiency plotted against the Reynolds number.

3.3 The stiffness of the head cover related to the efficiency

In figure 3–5 the efficiency at full load is plotted against the stiffness of the head covers. However, the turbines referred to in this thesis have speed numbers in the range of 0.25 - 0.3. And to account for the different speed numbers, the stiffness of the head cover is defined as the ratio between the height of the head cover and the nominal head, $*H/H_{Nom}$. The plot in figure 3–5 shows an increasing stiffness as the efficiency increases. Thus the stiffness increases with increasing unit size, which is in accordance with the design criteria. However, since the angle of deflection is often the basis

when the covers are dimensioned, a further examination of this parameter is performed.

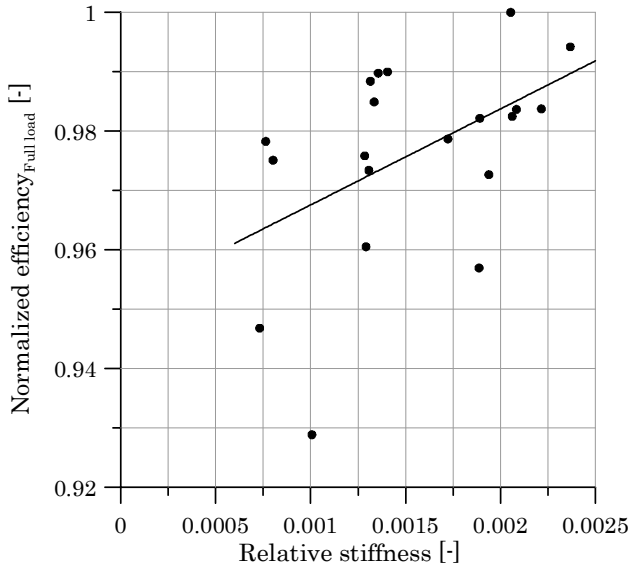

Figure 3–5: The efficiency at full load plotted against the stiffness, $*H/H_{Nom}$, of the head cover.

3.4 Deformation in terms of deflection and translation

As a prolonging of the examination of the angle of deflection, a further analysis of the actual translation in terms of the vertical displacement is also included in this chapter.

3.4.1 The angle of deflection

The angle of deflection is calculated from the translation data recovered from the finite element analysis. And to better understand the geometrical relation between the translation and the angle of deflection, a sketch relating the deflection and the vertical translation is drawn in figure 3–6.

$$\varphi = \operatorname{atan}\left(\frac{\Delta z_i - \Delta z_o}{R_o - R_i}\right) \tag{3.13}$$

But since the value of $(\Delta z_i - \Delta z_o)/(R_o - R_i) << 1$, the angle of deflection can be written as [14]:

$$\varphi = \frac{\Delta z_i - \Delta z_o}{R_o - R_i} \tag{3.14}$$

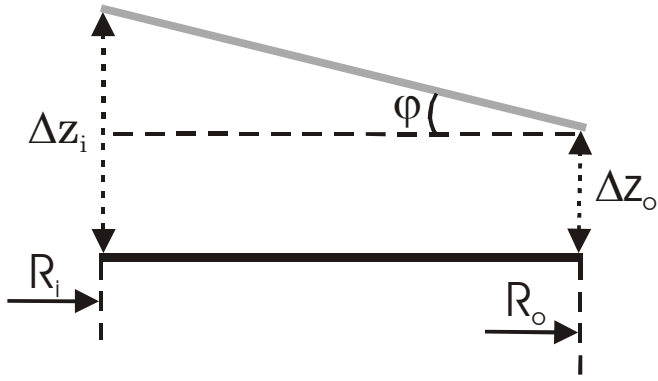

Figure 3–6: Angle of deflection.

The black solid line in figure 3–6 represents the head cover before it has been pressurized, whereas the gray solid line represents the head cover as it has experienced a deformation due to the water pressure.

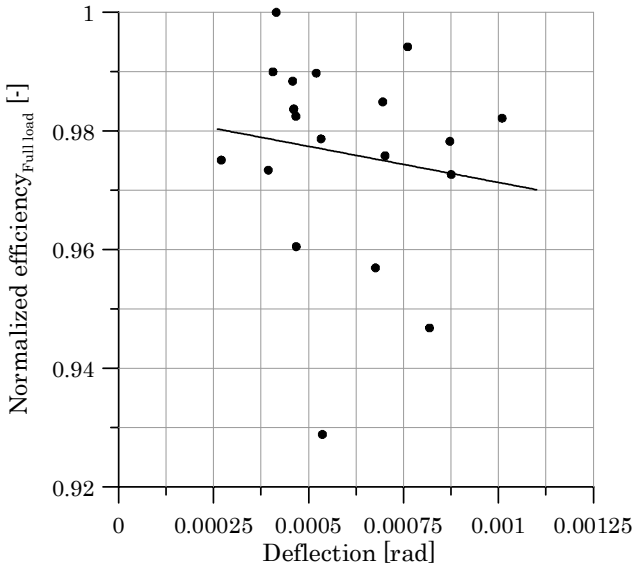

Figure 3–7: The deflection of the head cover plotted against the efficiency at full load.

As mentioned in chapter 3.1, the criteria when designing the head and bottom cover is based on the maximum allowable angle of deflection. And figure 3–7[1] shows a tendency of decreasing angle of deflection as the efficiency increases, which supports the idea of obtaining a lower acceptable angle of deflection as the unit size increases. However, by considering equation 3.14 and figure 3–6 one can conclude that a head cover may experience a low angle of deflection, although the vertical translation is large. Thus the angle of deflection does not describe the actual extent of the clearance gap, as opposed to the vertical translation. And since the design criteria is based on the maximum allowable angle of deflection, a further examination of the actual translation is performed in the following chapter.

1. In figure 3–7 a linear trend line is added to better visualize the tendency of the plot.

3.4.2 The vertical translation

In order to disprove or corroborate the suspicion of a large translation even if the angle of deflection is well within the acceptable limits, the absolute translation in both the outer and inner radius is plotted against the efficiency in respectively figure 3–8 and figure 3–9. And although the angle of deflection decreases with increasing efficiency, the displacement in terms of the vertical translation, increases with increasing efficiency. Thus the translation increases with increasing unit size.

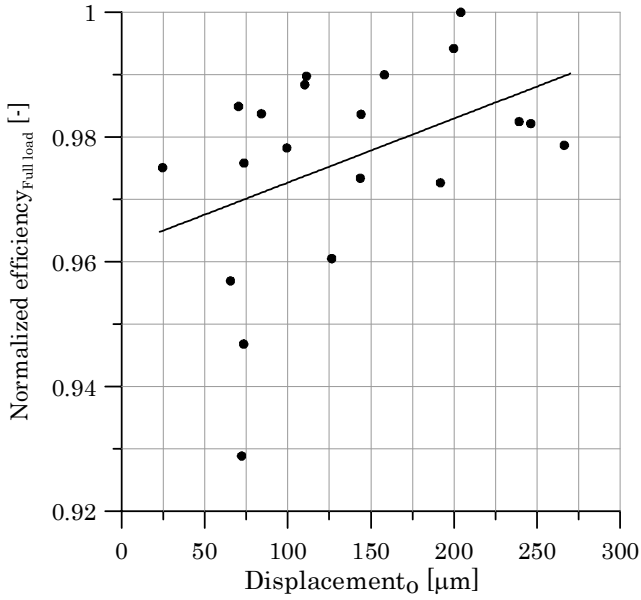

Figure 3–8: Displacement at the outer radius plotted against the efficiency at full load.

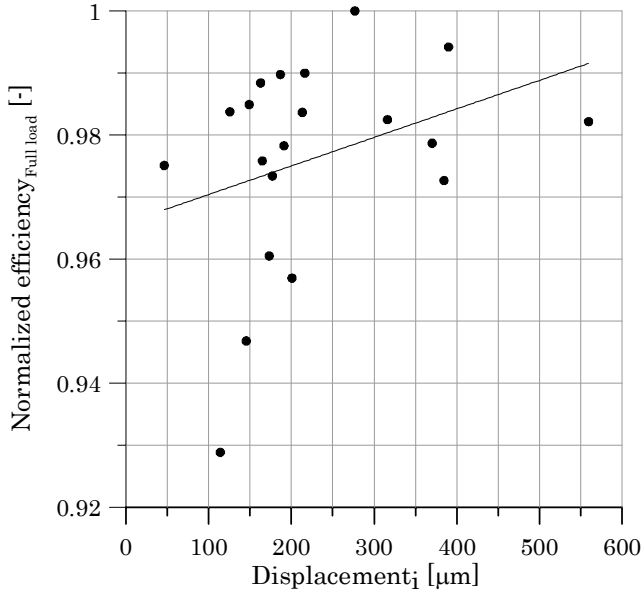

Figure 3–9: Displacement at the inner radius plotted against the efficiency at full load.

The vertical displacement at the inner radius is also plotted against the relative stiffness of each individual head covers in figure 3–10. And even though the relative stiffness of the head covers increases with increasing unit size, as shown in figure 3–5, this plot also obviously states that the vertical displacement increases with increasing unit size, as opposed to the angle of deflection. This result is not surprising, when regarding the results from chapter 2.2.2, where the translation was found to increase linearly with increasing height of the individual head covers.

In figure 3–4 the plot states that the efficiency increases with increasing unit size. And the fact that the efficiency increases as the vertical deformation increases might seem as a contradiction. But one must also bear in mind the decreased friction loss as the turbine unit increases.

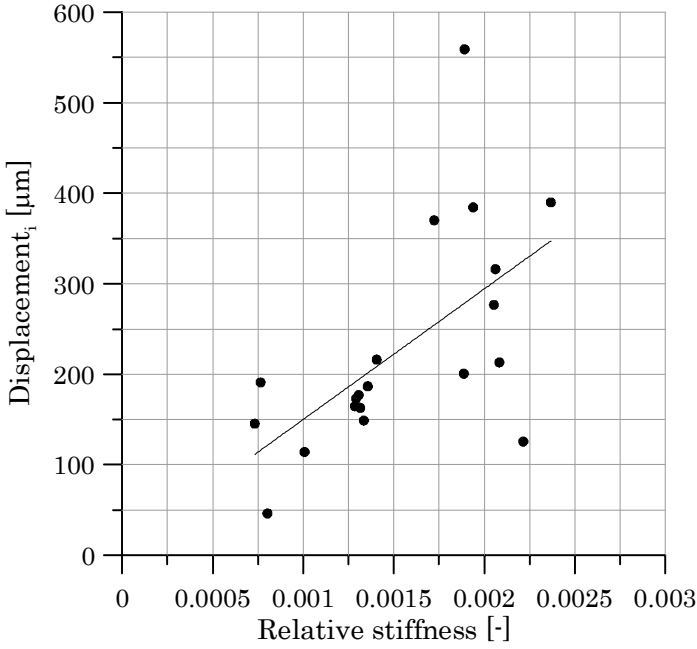

Figure 3–10: The vertical displacement at the inner radius plotted against the relative stiffness, $*H/H_{Nom}$.

Thus far only the displacements at the inner and outer point have been regarded. And the plots of the displacement at these points have clearly indicated an increasing displacement with increasing unit size. However, in figure 3–11 the vertical deformation across the entire head cover of to two different sized units is plotted against the normalized radius. The reason for this is to better visualize the actual extent of the entire clearance gap in the guide vane region of different sized turbines.

And to distinguish between the different sized turbines the Reynolds number is employed, as indicated in figure 3–11. Also, in this case the radius is reduced with respect to the largest radius of the individual head covers. The plot in figure 3–11 shows that the vertical translation follows a strictly linear behaviour with respect to the radius, as was indicated in figure 2–13. The angle of deflection of the large and small head cover is respectively

$7.1 \cdot 10^{-4}$ and $8.2 \cdot 10^{-4}$. And most importantly, this plot illustrates that the clearance gap of the larger unit is quite substantial compared to the smaller unit, despite the fact that the smaller head cover exhibits a larger angle of deflection.

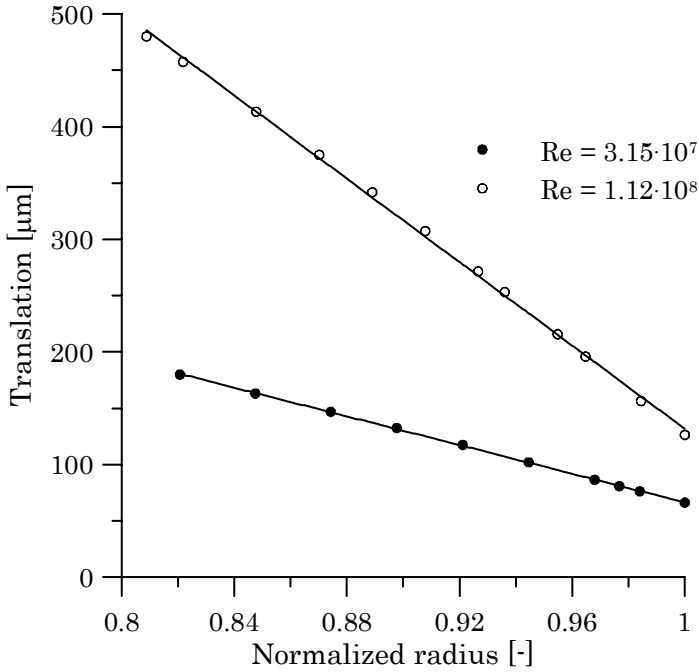

Figure 3–11: The vertical translation of a large and a small head cover.

3.5 Remarks

The results from the finite element computation report a decreasing angle of deflection with increasing unit size, in accordance with the design criteria. However, a further investigation of the deflection angle, φ, has shown that it does not describe the actual size of the clearance gap. The deflection parameter is more or less a relative size, which does not describe the actual height of the clearance gap. Thus the angle of deflection is not a determinant factor in emphasizing the extent of the leakage flow. And according to equation 3.14, it was established that a head cover may experience a low

angle of deflection although the vertical translation is quite substantial. Thus a further investigation of the absolute translation was conducted to rule out the possibility of an increasing translation with increasing unit size. And the further examination was quite conclusive, reporting an increasing translation with increasing unit size. Consequently, the potential leakage flow increases with increasing unit size, in conflict with the original design philosophy.

The design philosophy was based on the fact that the leakage flow in a large unit disturbs a larger part of the main flow, due to the low height of the guide vanes. Also, the long blades make the flow more sensitive to the leakage flow. Finally, it was also mentioned that the smaller guide vane openings in a high head Francis turbine increase the pressure difference between the pressure side and suction side. Thus the consequence of a clearance gap is more severe for a large unit compared to a smaller unit.

By regarding the vertical translation instead of the angle of deflection, an increase of the turbine efficiency is realistic due to a restriction based on the actual size of the clearance gap. Also, the vertical translation at the radius corresponding to z_0, has proven to be quite large when prestressing of the head covers have not been employed. Thus in addition to consider increased stiffness of the larger units it is also crucial to do the proper prestressing on order to keep the deformation on an acceptable level.

However, a numerical computation of the leakage flow in the guide vanes is presented in the next two chapters in order to emphasize how sensitive the leakage flow is to the extent of the clearance gap. Thus indicating the degree of importance of reducing the clearance gap to improve the flow condition in the guide vane and runner.

4 Numerical modelling of the flow in guide vanes

This chapter presents the modelling approach concerning a numerical calculation of the leakage flow in the guide vanes. The commercial software program Fluent 6.0 is employed to carry out the computation. The analysis of the flow in the stay vane is not well documented in this chapter, because the main focus is the flow condition in the guide vanes. But the modelling of the flow in the stay vanes is based on the same fundamental principal as the modelling of the flow in the guide vanes. However, some imperative details concerning the computation of the flow in the stay vane are presented for the purpose of credibility.

4.1 Computational domain

In order to establish a reasonable velocity profile at the inlet of the guide vanes, a computation of the flow in the stay vane is included. A numerical simulation of the flow through the stay vane and guide vane cascade is normally conducted without including the spiral casing and the runner vane. This is not an ideal approach since the boundary conditions are not well defined at the inlet of the stay vane nor at the outlet of the guide vane. Especially the boundary conditions at the outlet of the guide vane are difficult to decide due to the influence from the runner vane as it rotates. This interaction between the rotating runner blades and the stationary guide vanes gives rise to an unsteady flow in the cascade between the outlet of

the guide vane and the inlet of the runner vane. Furthermore, only one guide vane channel is modelled due to symmetry. Also, only half of the guide vane has been considered for the model generation, because all boundary conditions imposed at the inlet do not exhibit any variation over the span.

The leakage flow in the guide vanes is the problem of interest. And since the mesh resolution of the model is limited by the Central Processing Unit (CPU) of the computer, the guide vane and the stay vane have been computed separately in order to achieve a higher mesh resolution in the guide vane cascade. However, the physical presence of the stay vane will obviously influence the flow condition at the inlet of the guide vane. Thus this interaction is not accounted for as the guide vane and stay vane are computed separately. But since the scope of this work is to emphasize how sensitive the leakage is to the extent of the clearance, this modelling approach is believed to be sufficient at this level.

4.2 Mesh

In the near-wall region the solution variables change with large gradients, and therefore a high mesh resolution of this region is imperative in order to predict the flow conditions. The turbulent flows are highly influenced by the presence of walls, where the mean velocity field is effected through the no-slip condition that has to be satisfied at the wall [18]. However, the turbulence is also effected by the presence of viscous damping near the wall, which reduces the tangential velocity fluctuations. In general, the near-wall modelling significantly impacts the validity of the numerical solutions in this region. Therefore, accurate resolution of the mesh in the near-wall region increases the precision of the predictions of the wall-bounded turbulent flows. And in order to verify the computed flow condition, a wall parameter is introduced to validate the chosen mesh-resolution at the wall:

$$y^+ \equiv \rho u_\tau y / \mu \tag{4.1}$$

The y variable in equation 4.1 denotes the distance from the wall to the nearest grid node, thus a large y value corresponds to a low resolution of the near-wall region, equivalent to a large y^+ value. Since y^+ depends on geometrical factors as well as flow conditions, it is difficult to obtain the correct value of y+ before any solutions have been produced. Correspondingly, the first grid generation has to rely on estimates only, and after a

completed computation a proper estimate of y^+ can be found. If the value of y^+ is not satisfactory, another simulation with a different grid resolution is performed.

The near-wall region can be subdivided into three layers, corresponding to the viscous sublayer in the innermost region, the fully turbulent layer at the outer region and the interim region between the viscous sublayer and the fully turbulent-layer. In the viscous sublayer the flow is almost laminar, and the viscosity plays a dominant role in momentum, heat and mass transfer. In the turbulent-layer the turbulence obviously plays a major role. In the transition zone between these two layers the viscosity and the turbulence are equally important. In figure 4–1 the different subdivisions are illustrated by plotting the velocity profile in the different subdivision.

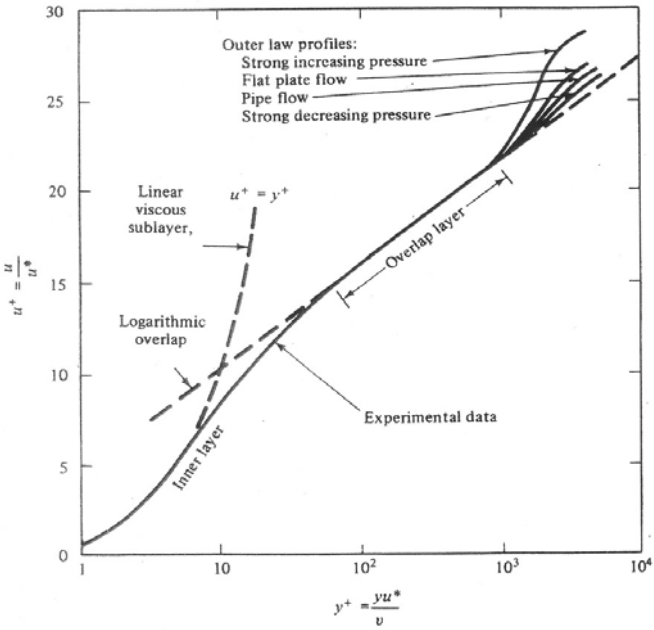

Figure 4–1: Subdivisions of the near-wall region. Figure from [19].

These velocity profiles are calculated according to the linear law in the near wall region, the logarithmic law in the outer part and the overlap law in the overlap region [20].

In figure 4–1, data based on numerous experiments are also plotted for the purpose of validating the derived velocity relations. At the innermost region the velocity profile tends towards a linear behaviour, but as the y^+ value increases the profile exhibits a logarithmic behaviour. The plot implies that the experimental data quite well follows the derived laws in the different regions. Thus the experimental data verifies the inner-, outer and overlapping laws, which is a mathematical interpretation of the different sublayers [18].

The Fluent code offers two different approaches when solving the near-wall region, namely the Wall Function Approach and the Near-Wall Model Approach. The first code is due to Launder and Spalding [21], and has advantages in terms of comparably low grid resolution and therefore saved computational resources. In this case the viscous sublayer is not resolved numerically. Instead, this region is modelled in terms of empirical equations. This places restrictions to the distance from the wall to the nearest grid cell. From figure 4–1 one can see that the log-law is valid for $y^+ > 30$. And although Fluent employs the linear law when $y^+ < 11.225$, corresponding to the viscous sublayer, using an excessively fine mesh near the walls should be avoided, because the wall functions cease to be valid in the viscous sublayer. In other words, the first grid cell must lie in the region where the log-law is valid. Due to the active wall function the first grid cell should be placed in the region $30 < y^+ < 60$, preferable as close to the lower bound as possible [20].

The second near-wall code, namely the Near-Wall Model Approach, resolves the viscous sublayer at the innermost wall region. In this case, experiments have shown that the first grid node should be placed at $y^+ = 1$. In addition, 10 grid nodes should be placed within the viscous sublayer to achieve accurate results. Due to the higher mesh resolution at the innermost region, this approach is more computer demanding compared to the near-wall function. It should however be mentioned that this approach is preferable in typical low Reynolds number flow, where the wall-effected zone is quite substantial.

When the mesh is fine enough to resolve the laminar sublayer, the wall shear stress is obtained from the laminar stress-strain relationship:

$$\frac{U}{U_\tau} = \frac{\rho U_\tau y}{\mu} \tag{4.2}$$

If the mesh is too coarse to properly resolve the laminar sublayer, corresponding to high y^+, it is assumed that the centroid of the wall-adjacent cells falls within the logarithmic region of the boundary. Thus a proper and valid flow solution is not obtained in the near-wall region [20].

In order to get a visual feeling of the mesh resolution, a mesh of the head cover is illustrated in figure 4–2. Also, the mesh resolution of the stay vane is included in figure 4–3.

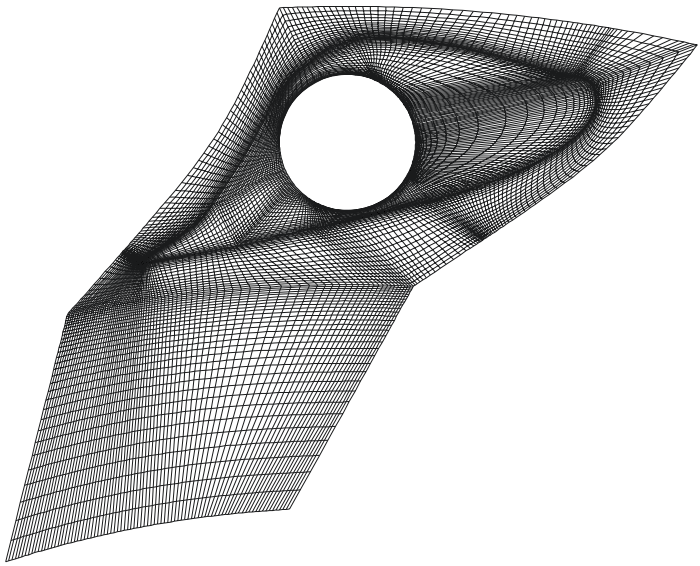

Figure 4–2: Grid resolution of the guide vane cascade.

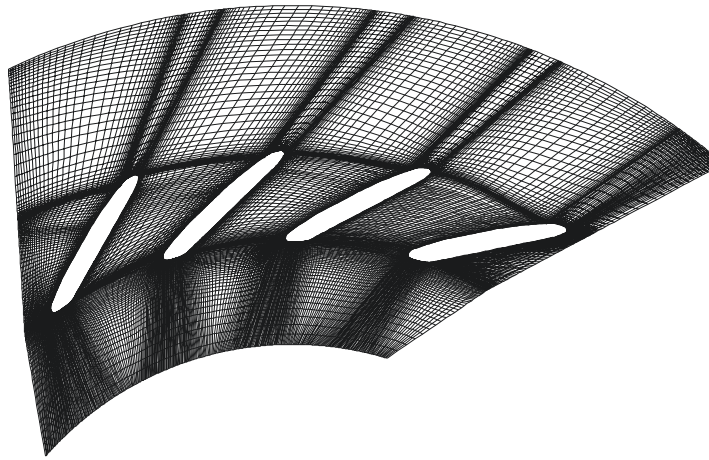

Figure 4–3: Grid resolution of the stay vane cascade.

4.3 Boundary conditions

For incompressible calculation it is common to apply velocity components as inlet boundary conditions. And in this particular case the radial and tangential velocity components are applied to the inlet of the stay vane domain. These flow parameters are unknown at the inlet domain of the computational volume, but since the volume flow through the turbine is known from measurements an average radial velocity can be calculated according to the following equation:

$$c_r = \frac{Q}{2\pi r B} \tag{4.3}$$

As can be seen from equation 4.3, the radial velocity at a given radius and height of turbine is a function of the net flow.

The tangential velocity, on the other hand, is a bit more complicated due to the complex flow conditions in the spiral casing. Thus a proper estimate of the tangential velocity component would require a complete analysis of the flow condition in the spiral casing [21]. But since we are not interested

in the detailed flow condition at the inlet of the stay vane it is adequate to calculate an average tangential velocity, expressed in terms of the radial velocity and the inlet velocity angle:

$$c_t = \frac{c_r}{\tan\alpha} \tag{4.4}$$

Also, since the stay vane and guide vane is computed separately, an interior surface at the immediate outlet of the stay vanes is defined as the inlet of the guide vane. Thus velocity data from the interior surface are retrieved and imposed at the corresponding inlet of the guide vane cascade. Consequently, the radial and tangential velocity is only computed at the inlet of the stay vane.

Because the solver code can extrapolate the pressure from the interior of the computational domain, a constant pressure field is applied as the boundary condition at the outlet of both the stay vane and guide vane domain.

In figure 4–4 the computational domain of the guide vane is illustrated to get a visual feel of the various boundary conditions applied to the different surfaces of the guide vane cascade. As can be seen from the bottom of figure 4–4, the guide vane is made with an extension on the pressure side around the guide vane shaft. This design is chosen for the purpose of strengthen.

The mid-span section of the blade is assumed to be a plane of symmetry. And the boundaries which separate two adjacent vanes are linked to each other by rotational periodic conditions.

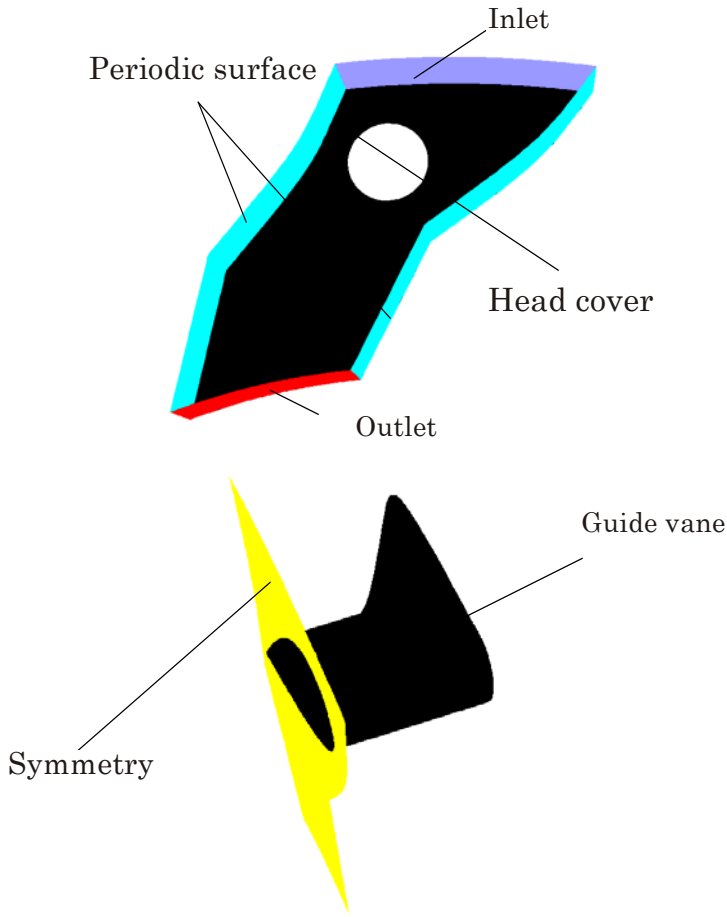

Figure 4–4: Computational domain of the guide vane cascade.

4.4 Flow condition & The solver setup

This chapter presents a short analysis of the flow condition in the entire guide vane cascade including the narrow gap between the guide vanes facing plate and the head cover. An analysis of the given flow condition is im-

perative in order to choose the right solver and to make the proper solver setup, which reflects the actual flow situation. For all flows, Fluent solves conservation equations for mass, momentum and energy[1] [23]. Additional transport equations are also solved when the flow is turbulent, as will be explained below. In order to choose the right solver one first of all has to decide whether the flow is turbulent or laminar. And in most cases it is sufficient to calculate the Reynolds number in order to establish whether the flow is turbulent or laminar.

4.4.1 The Reynolds number

The dimensionless Reynolds number is a primary parameter correlating the viscous behaviour of all newtonian fluids.

$$Re = \frac{\rho VL}{\mu} \tag{4.5}$$

and since the ratio μ/ρ in equation 4.5 is defined as the kinematical viscosity, υ, one can employ the following relation:

$$Re = \frac{VL}{\nu} \tag{4.6}$$

where V and L are characteristic velocity and length scales of the flow.

As mentioned above the Reynolds number is often used to decide whether the flow is turbulent or laminar. However, sometimes we are dealing with a transition between laminar and turbulent flow or vice versa, and it is difficult to predict the flow conditions by just employing the Reynolds number. But the overview below presents an approximate classification of the different flow condition as a function of the Reynolds number [18]:

$0 < Re <$ 1: Highly viscous laminar “creeping” motion

$1 < Re <$ 100: Laminar, strong Reynolds-number dependence

1. Since these governing equations are thoroughly presented in a wide range of literature, they will not be presented in this thesis.

$100 < Re < 10^3$: Laminar, boundary-layer theory useful

$10^3 < Re < 10^4$: Transition to turbulence

$10^4 < Re < 10^6$: Turbulent, moderate Reynolds-number dependence

$10^6 < Re < \infty$: Turbulent, slight Reynolds-number dependence

In general, turbulent flow occurs at high Reynolds number. Turbulence often originates as an instability of laminar flow when the Reynolds number becomes too large. These instabilities are related to the interaction of viscous terms and non-linear inertia terms in the governing Navier-Stokes equations [24]. The transition from laminar to turbulent flow is well a documented phenomena, but as mentioned above in some cases the flow might be subjected to a reverse transition or a so-called relaminarization of the turbulent flow. And the most important feature to bear in mind when regarding a relaminarization, is that even if the Reynolds number is lower than the critical value, a relaminarization is not obvious. Accordingly, a calculation of the Reynolds number is not satisfactory in order to establish whether the flow is turbulent or laminar. Thus a further investigating of the flow conditions must be performed [25].

The Reynolds number of the flow in the guide vane channel is calculated according to equation 4.6, where the characteristic length, L, is defined as the outlet diameter of the guide vane. And the velocity at the outlet is defined as the characteristic velocity. Also, the velocity at the outlet of the guide vane is known prior to the numerical computation. Based on this the value of the Reynolds number reads approximately $2 \cdot 10^8$, corresponding to a turbulent flow in the guide vane channel. However, in this particular case, the clearance gap and the guide vane channel have to be considered separately when the Reynolds number is calculated. The reason for this is that the flow situation in the guide vane channel does not in any way represent the flow condition in the clearance gap. The outlet diameter of the guide vane does not represent a characteristic length of the narrow clearance gap, nor does the velocity at the outlet of the guide vane represent the velocity in the clearance gap. Accordingly, the calculated Reynolds number for the guide vane channel does not apply for the clearance gap.

The characteristic length of the clearance gap domain is the height of the narrow gap. Furthermore, the characteristic velocity is defined as the av-

erage velocity at the outlet of each individual clearance gap. However, as opposed to the velocity at the outlet of the guide vane, the velocity at the outlet of the clearance gap is not known prior to the numerical computation. Thus the 1 mm clearance gap model was computed with both a laminar and a turbulent solver in order to establish knowledge of the velocity at the immediate outlet of the clearance gap[2]. And the results from both the solvers reported velocity corresponding to a turbulent flow. Subsequently, each model was computed with a turbulence solver. The characteristic parameters based on the results from the turbulence modelling and the Reynolds numbers associated with each clearance gap are summarized in table 4-1.

Clearance gap [m]	V [m/s]	L [m]	Re [-]
0,00025	12	0,00025	3000
0,001	22	0,001	22000
0,002	30	0,002	60000
0,004	40	0,004	160000

Table 4-1. Reynolds number in the different clearance gaps.

Based on the data in table 4-1, one can conclude that also the flow in each clearance gap clearly corresponds to a turbulent flow. Thus a further investigation of the flow condition is not necessary. And as can be seen from table 4-1, the Reynolds number increase rapidly with increasing clearance gap.

Turbulent flow is characterized by a fluctuating velocity profile. These fluctuation mix quantities such as momentum, energy and species concentration, resulting in a fluctuation of the listed quantities as well. Since these fluctuations can be of small scale and high frequency, they are overly expensive to compute directly in practical engineering calculations. Instead, the instantaneous governing equations can be manipulated, for instance time-averaged, resulting in a modified set of governing equations

2. For a given gap the velocity is the determinant factor whether the flow in the clearance gap is laminar or turbulent. Hence have chosen to base the calculation of the Reynolds number on the downstream part of the guide vane shaft, since the cross flow and thus the lowest velocity are confined to this region.

that are computational less expensive to solve. However, these modified equations contain additional unknown variables, and additional turbulence models are needed in order to solve these variables in terms of known quantities.

Since both the flow in the guide vane channel and in the narrow clearance gap between the head cover and guide vane facing plate is turbulent, one can employ a turbulence model to compute the flow pattern in the entire guide vane cascade. The commercial Fluent code offers five different turbulence models:

-Spalart-Allmaras

-k-epsilon

-k-omega

-Reynolds stress

-Large eddy simulation

The final choice of turbulence solver depends on details concerning the flow conditions, the level of accuracy required, the available computational resources and the amount of time available for the given problem. The theory and application of the different solvers is well documented, but is only partially presented in this thesis.

The standard k-ε model is the simplest complete model of turbulence, in which a solution of two independent equations is used to calculate the additional turbulence term of the modified governing equations. And in this case the additional transport equations calculate respectively the turbulent kinetic energy, k and the turbulence dissipation rate, ε.

The Spalart-Allmaras model was originally designed specifically for aerospace applications involving wall-bounded flows. Also, this model has shown to give good results for boundary layers subjected to adverse pressure gradients [20]. Thus in this particular case the Spalart-Allmaras model is chosen to calculate the flow in the guide vanes, since the guide vanes exhibit a wing profile. The flow in the guide vane is obviously also a

wall-bounded flow. The Spalart-Allmaras is a relatively simple model, and as opposed to the k-ε model, this model only involves solving one additional equation to calculate the additional turbulence term of the modified governing equations. However, in order for the given turbulence solver to retain acceptable result some turbulence parameters are required as input.

4.1.2 Determining turbulence parameters

When turbulent flow enters the computational domain, or at a far-field boundary, the solver code requires boundary values for the turbulent kinetic energy, k, and the turbulence dissipation rate, ε. There are four methods available for specifying the turbulence parameters [20]:

- Set k and ε explicitly

- Set the turbulence intensity and turbulence length scale

- Set the turbulence intensity and hydraulic diameter

- Set the turbulence intensity and viscosity ratio

In this particular case the turbulence intensity and hydraulic diameter is specified, from which the turbulent kinetic energy and the turbulent dissipation rate are calculated. The turbulence intensity was set to 3% and the hydraulic diameter was defined as the height of the individual clearance gaps.

4.2 Remarks

In any numerical calculation it will be of great importance to compare the results with analogous measurements of the corresponding model or prototype, in order to validate the numerical approach. And since there have been no measurements of the leakage flow in the given guide vane, it is difficult to know if the right solver and solver setup is made. Even so, the chosen solver and parameters are based upon previous experience and are believed to give a proper indication of the leakage flow in the clearance gap. One should also keep in mind that the main objective is to establish the sensitivity of the leakage flow against the extent of the clearance gap.

5 Results from the numerical modelling of the leakage flow

This chapter presents the results from a numerical computation of the leakage flow in the guide vanes with a nominal head of 525 m, flow of 65 m^3/s and a power output corresponding to 315 MW. The main objective is to illustrate how sensitive the leakage flow is to the extent of the clearance gap between the head cover and guide vanes facing plate. Consequently, the guide vanes have been modelled with four different clearance gaps corresponding to 0.25 mm, 1 mm, 2 mm and 4 mm. However, the results from the FEM analysis only reported a translation, due to the water pressure alone, between 0.045-0.55 mm at the inner radius. But due to the severe interaction between erosion and vortex flow, the modelling of a 2 mm and a 4 mm clearance gap are justified. In fact, in salt laden water circular grooves of about 10-12 mm deep and 30-65 mm wide have been detected [26]. One should also keep in mind the additional clearance due to the required dry clearance and finish tolerance, which lies between 0,05 - 0,1 mm depending on the unit size [27].

In addition, a validation of the results is completed with respect to the mesh generation and the solver code. Also, an analytical interpretation of the flow in the clearance gap has been carried out and compared to the numerical results.

5.1 Results

The influence from the leakage flow on the main flow and the natural course of the cross flow in the clearance gap is thoroughly examined in the following sub-chapters. Subsequently, the flow condition in the different sized clearance gaps are compared to underline the gravity of large or increasing clearance gaps.

5.1.1 The characteristic of the leakage flow

In figure 5–1 a vector plot of the magnitude velocity at the vicinity of the head cover is shown. Three distinct regions are marked with red circles. The flow pattern in these regions exhibits special features, which are found imperative in order to understand the substantial loss in efficiency due to the secondary flow.

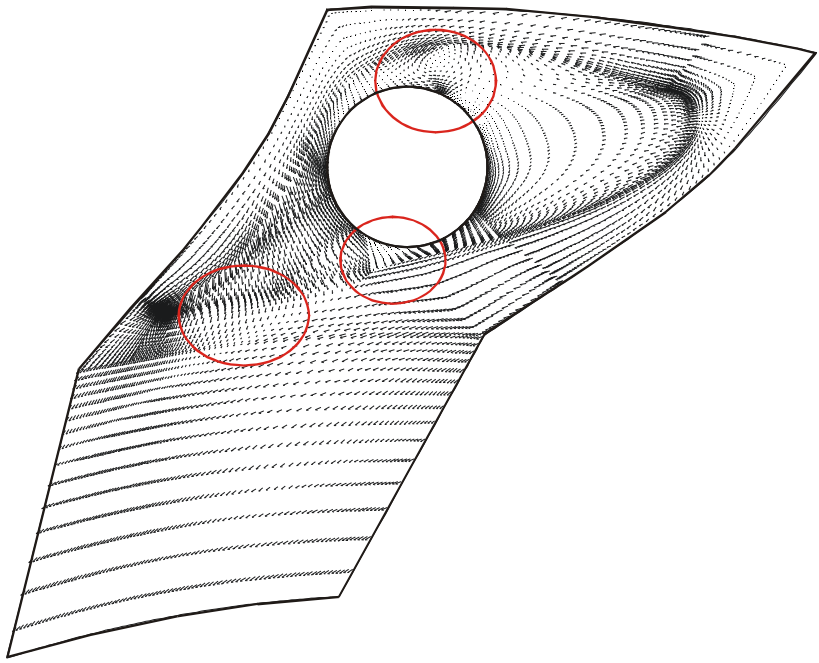

Figure 5–1: Vector plot of the magnitude velocity in the clearance gap of 1 mm.

In the encircled regions close to the shaft at respectively pressure side and suction side, a vortex flow is detected. While the encircled region at the suction side of the trailing edge shows a substantial impact on the main flow from the cross flow. Also, as can be seen from figure 5–1, the cross flow does not appear until the flow approaches the guide vane shaft. And from the mid-chord to the trailing edge of the guide vane the leakage flow increases. To enlighten this relation a static pressure contour of the flow in the middle of the guide vane is shown in figure 5–2. According to this plot, the pressure decreases with an uniform gradient along the surfaces. However, the pressure drop at the suction side is larger compared to the pressure drop at the pressure side. Thus the pressure difference between pressure side and suction side increases with decreasing radius. Hence at the leading edge the pressure difference is to low to give an evident cross flow, and the flow is rather heading in the radial direction. But as the flow approaches the guide vane shaft the pressure difference has obtained such a large value that a cross flow is inevitable. This relation is also supported by the measurements performed by Xin Chen [28], where measurements indicated no leakage near the leading edge of the guide vane, however an increasing leakage from mid-chord to the trailing edge was seen readily.

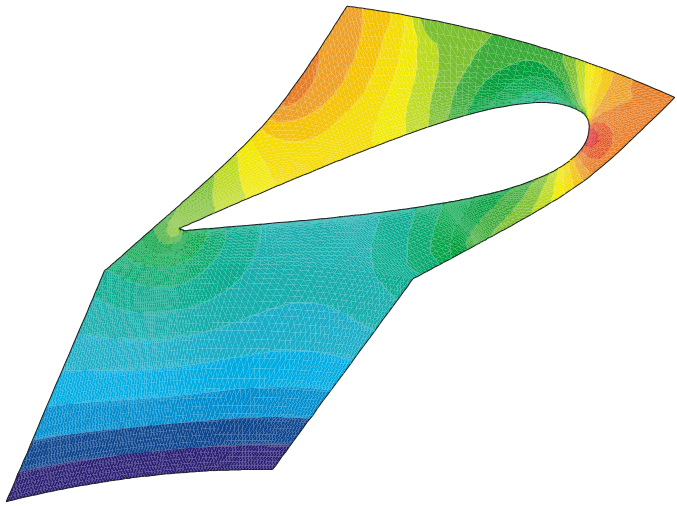

Figure 5–2: Static pressure contour in the middle of the guide vane channel.

However, in order to get a proper visual feel of the flow conditions in the clearance gap, the distinct regions in figure 5–1 are magnified and closely examined.

The guide vane shaft acts as an obstacle to the flow in the clearance gap and blocks the flow at the mid-chord of the guide vane. Thus the velocity close to the shaft is heavily reduced, as indicated in figure 5–3. However, the leakage flows alongside the circular shaft, giving rise to a swirl flow in the region where the leakage from the right and left side of the shaft meets, as illustrated at the right in figure 5–3. In addition, a swirl flow at the upper right side of the shaft is also detected as shown at the left in figure 5–3. In this region the cross flow interacts with the radial flow in the clearance gap, giving rise to a swirl flow.

As mentioned earlier, any swirl flow induces erosion in sand laden water, and should be avoided. But in this case the swirl flow is inevitably as long as the leakage flow is maintained.

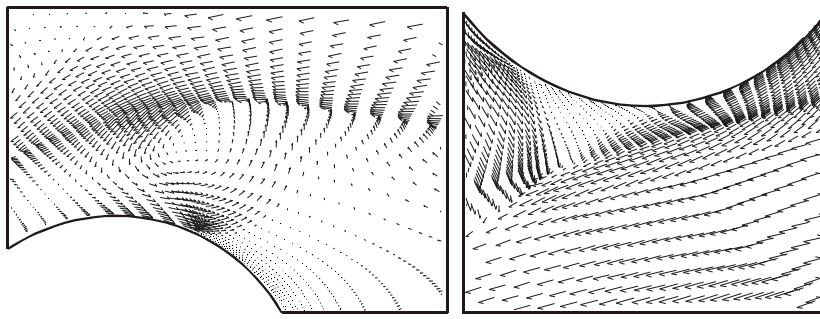

Figure 5–3: Guide vane shaft at the suction side and pressure side.

As the flow leaves the clearance gap on the suction side, it forms about 90 degree angle with the direction of the main flow. But at a certain distance from the suction side, the cross flow is not able to maintain its features and the properties of the main flow is attained, as shown in figure 5–4. Anyway, the disturbance of the main flow at the trailing edge on the suction side causes a non-uniform velocity profile at the inlet of the runner vane. And as shown figure 5–4, the disturbance is quite substantial, where a large part of the main flow in the outlet region is influenced. The worsened

flow pattern also propagates through the runner channel and further reduces the efficiency. Thus compared to the suction side the influence on the pressure side is not as significant, which is supported by H.Brekke et. al [29].

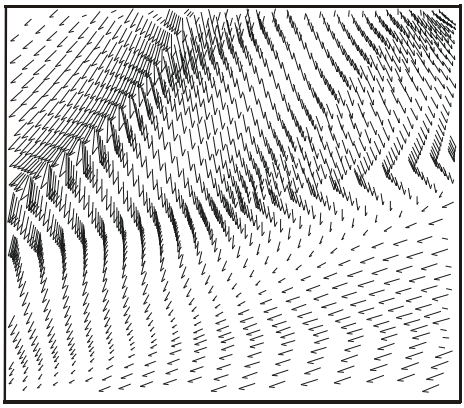

Figure 5–4: Cross flow at the suction side of the trailing edge, 1 mm.

To emphasize the extent of the influence on the main flow, velocity plots at varies distance from the head cover are shown in figure 5–5 and figure 5–6.

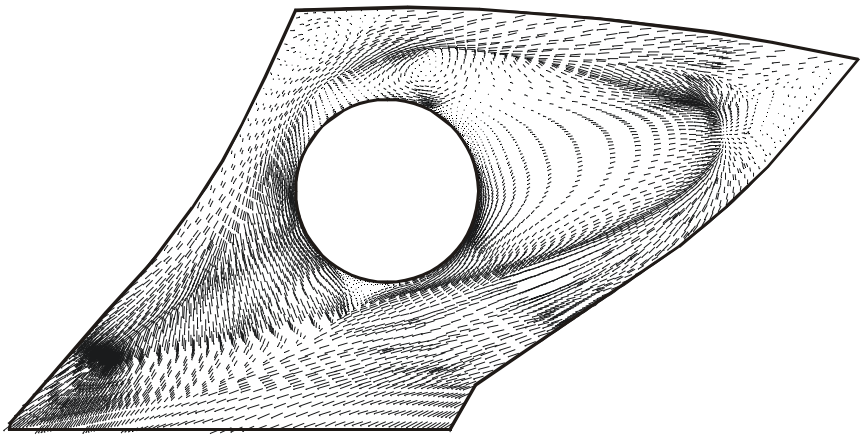

Figure 5–5: Vector plot of the magnitude velocity in the middle of the 1 mm clearance gap.

In figure 5–5 a plot of the magnitude velocity vectors in the middle of the 1 mm clearance gap is shown. The main flow at the suction side is clearly influenced by the cross flow at this distance from the head cover. And even at a distance 2.5 mm from the head cover, the main flow experience a significant influence from the cross flow, as shown in figure 5–6. In addition, the vortex flow detected at the pressure side in figure 5–3 is also present.

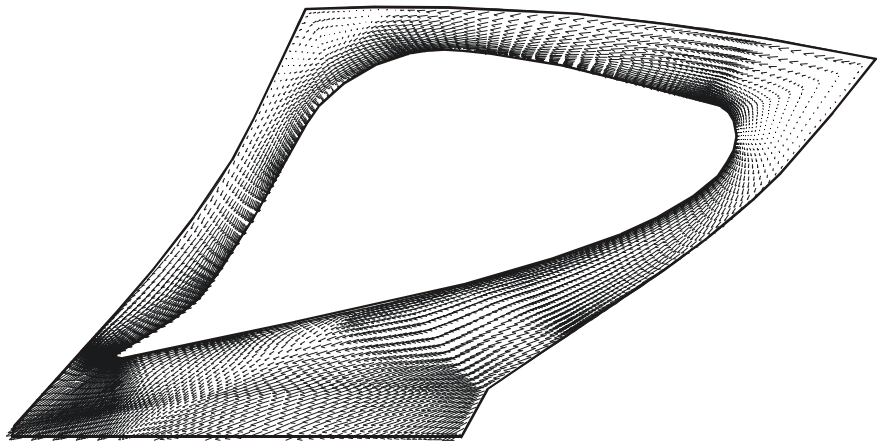

Figure 5–6: Flow pattern 2.5 mm from the head cover, 1 mm clearance gap.

The flow in the mid-span of the guide vane, on the other hand, is clearly not effected by the leakage flow in the guide vanes. Neither swirl flow nor disturbance of the flow at the outlet of the suction side is detected in figure 5–7, which illustrates the flow in the middle of the guide vane channel.

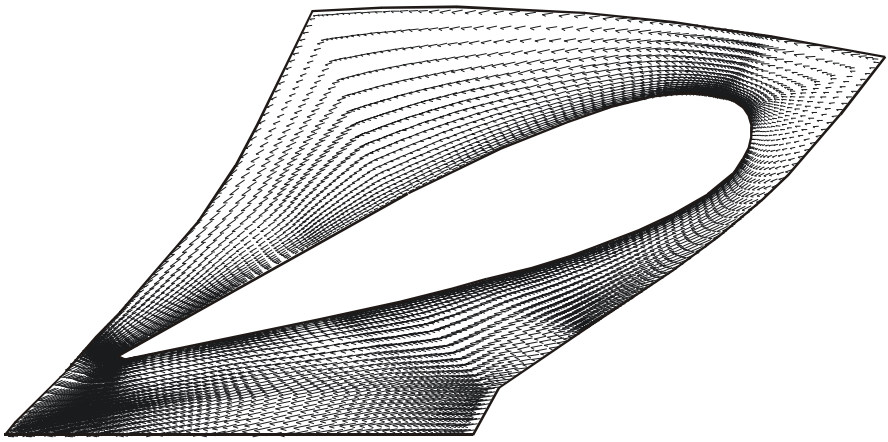

Figure 5–7: Flow condition in the middle of the guide vane channel, 1 mm gap.

5.1.2 Comparison of the flow in the different clearance gaps

As mentioned in the preface of this chapter, a comparison of the cross flow at the different clearance gaps is performed to enlighten the severity of large openings between the covers and the guide vane facing plates. Also, this comparison substantiates the presence of a potential efficiency increase by keeping the height of the gaps as small as possible.

In figure 5–8 a vector plot of the magnitude velocity in the 0.25 mm clearance gap is shown. The cross flow attains the same tendency in this gap as in the gap of 1 mm. However, since the velocity in the smallest gap is comparatively low, the cross flow almost immediately attains the feature of the main flow as it leaves the clearance gap. Hence the flow on the suction side of the trailing edge is barely influenced by the cross flow. In figure 5–9 a similar velocity plot is shown for the 4 mm clearance gap. And as opposed to the cross flow in the 0.25 mm clearance gap, the cross flow in the 4 mm clearance gap disturbs a rather substantial part of the main flow at the suction side. And along with the increased velocity, the vortex flow is heavily enhanced as the clearance gap is increased to 4 mm.

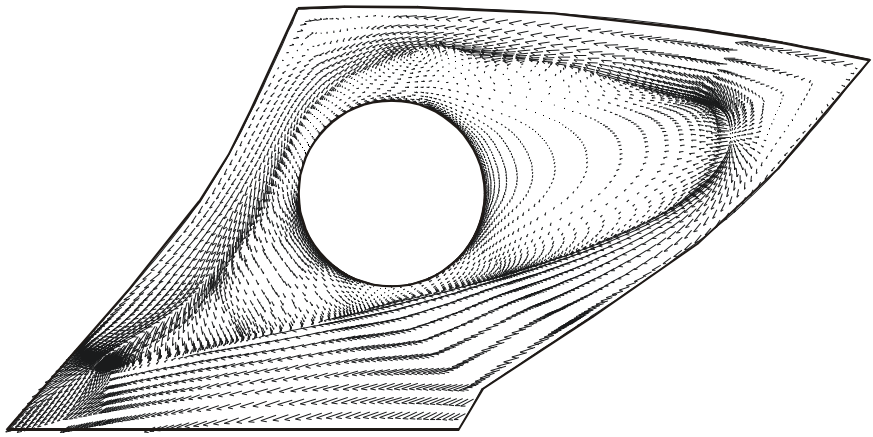

Figure 5–8: Vector plot of the magnitude velocity in the 0.25 mm clearance gap.

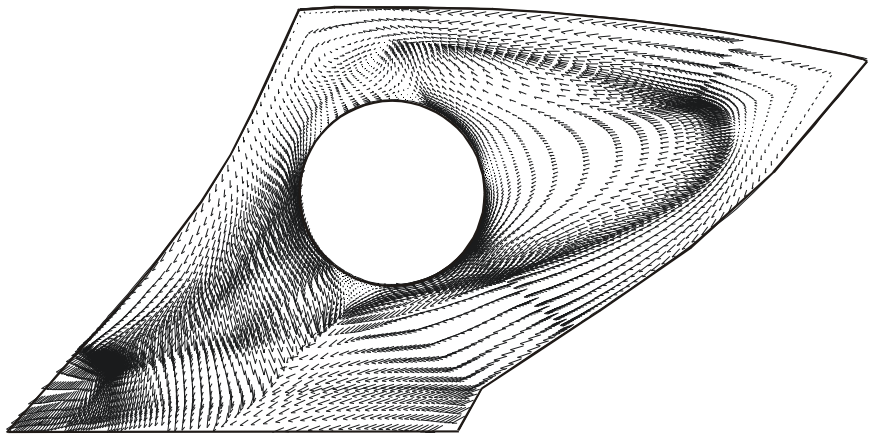

Figure 5–9: Vector plot of the magnitude velocity in the 4 mm clearance gap.

Also, a vector plot of the magnitude velocity at a distance 2.5 mm from the head cover of the 0.25 mm model is shown in figure 5–10.

In this region the disturbance on the main flow at the suction side is minimal. And just a weak vortex flow at the pressure side is detected.

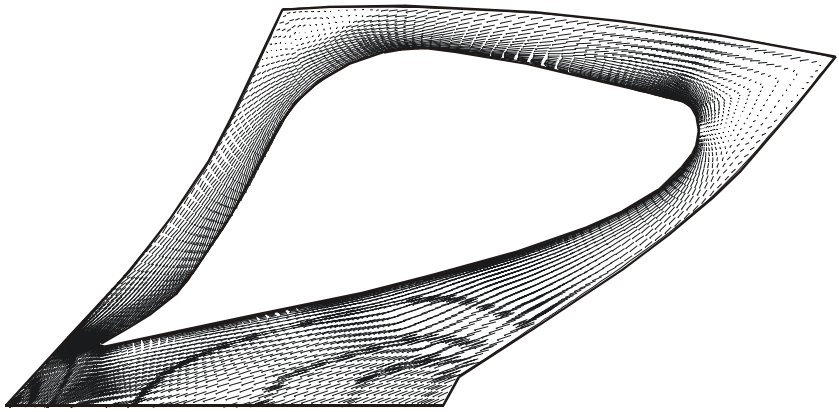

Figure 5–10: Flow condition 2.5 mm from the head cover, 0.25 mm clearance.

And for the purpose of comparison, a similar plot of the 4 mm model is given in figure 5–11.

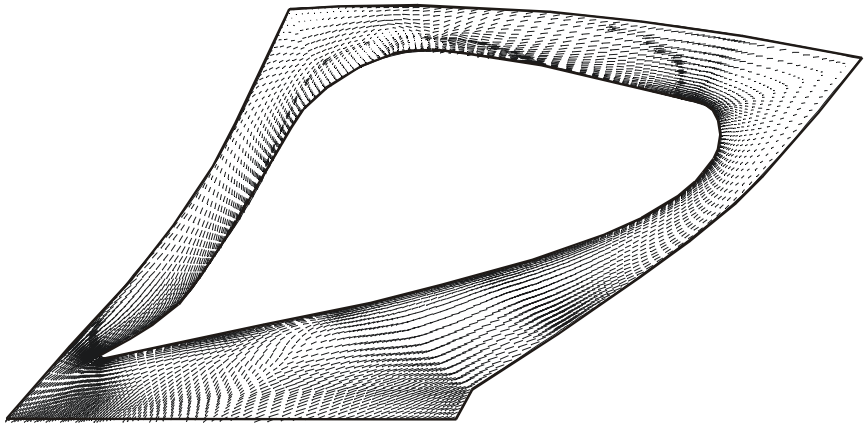

Figure 5–11: Flow condition 5 mm from the head cover, 4 mm clearance.

However, in this case the distance from the head cover is increased to 5 mm. And a noticeable influence on the main flow at the trailing edge is still

detected at this distance. Also, a weak vortex flow at the pressure side is observed.

The different flow conditions in the 0.25 and 4 mm clearance gap are quite evident. And in addition to the higher velocities in the 4 mm clearance gap, the disturbance on the main flow is quite worsened in the case of a 4 mm clearance gap.

However, to better visualize the different flow conditions in the various clearance gaps, three particles have been dropped at different radii in the middle of each clearance gap. And in figure 5–12 and figure 5–13 the particle paths coloured by velocity magnitude are illustrated

The particle traces in the 0.25 mm clearance gap also show that the main flow in the guide vane channel is little influenced by the cross flow. The particles almost perfectly follow the direction of the guide vane as they leave the clearance gap. But as the height of the clearance gap increases a significant disturbance of the main flow at the suction side is detected. The particle trajectories in figure 5–12 and figure 5–13 show that the path length, in which the velocity makes an almost 90 degree angle with the direction of the main flow, increases significantly with increasing gap height. Thus a larger part of the main flow is disturbed by the cross flow.

As the leakage flows towards the suction side, the velocity decreases due to the increased viscosity. However, a further investigation of the velocity in the clearance gaps has been performed as the magnitude velocity of the particle drop at the largest radius is plotted against the elapsed time in figure 5–14 and figure 5–15.

The particles attain the lowest velocity at the immediate outlet of the clearance gap, according to the increased viscous effect at the outlet. But as the particles enter the main flow in the guide vane channel, the velocity increases in accordance with the flow condition in the guide vane channel. However, the velocity plot of the particle drop in the 0.25 mm clearance gap shows a significant drop in velocity approximately 0.015 seconds after the particle has been dropped. But this can be explained by regarding figure 5–12 and noticing that at a certain radius the particle approaches a zone, which is influenced by the cross flow. Thus the particle velocity in this region decreases according to the cross flow velocity.

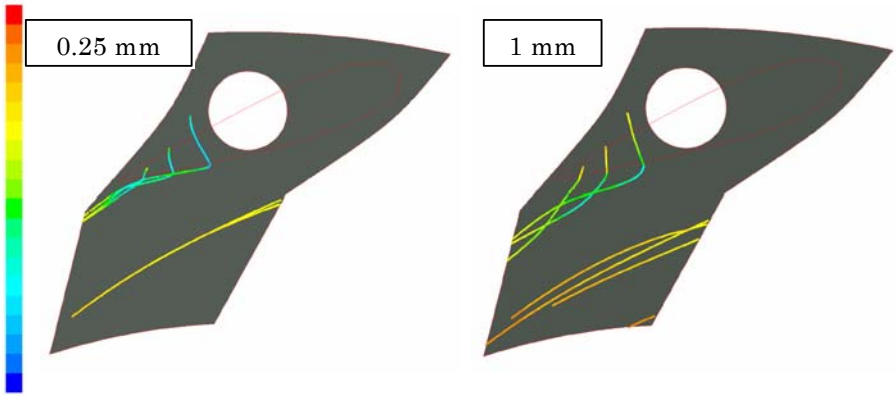

Figure 5–12: Particle traces coloured by velocity magnitude in respectively 0.25 mm and 1 mm clearance gap.

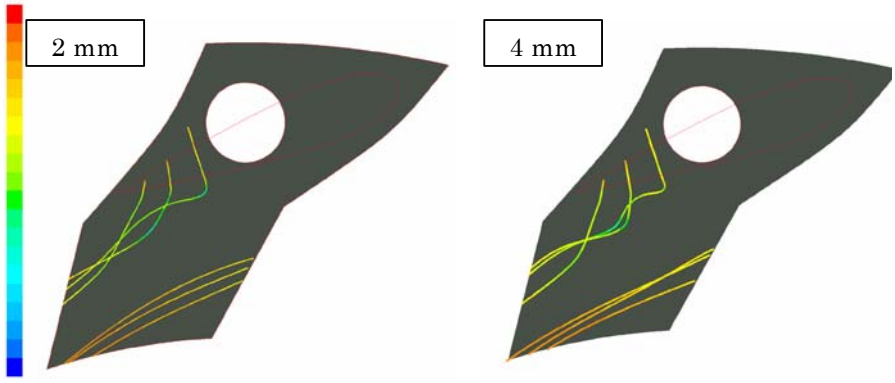

Figure 5–13: Particle traces coloured by velocity magnitude in respectively 2 mm and 4 mm clearance gap.

Furthermore, the velocity plots show that the magnitude velocity increases significantly as the height of the clearance gap increases. The velocity at the outlet of the smallest clearance gap is approximately 12 m/s, whereas the velocity in the largest gap amounts to approximately 32 m/s. Thus the pressure distribution on the suction side decreases with increasing clearance gap. This phenomenon is also supported by Moore et. al [31],

where a test rig consisting of five blades and a pair of adjustable end pieces were used to investigate the leakage flow at different clearance gaps. However, pressure measurements showed that the pressure distribution on the suction side of the blade with clearance was lower than the pressure on the suction side without clearance. Also Storer et. al [32] detected a similar tendency as experimental measurements in a linear cascade with tip clearance reported a substantial reduction of the static pressure near the tip on the suction side.

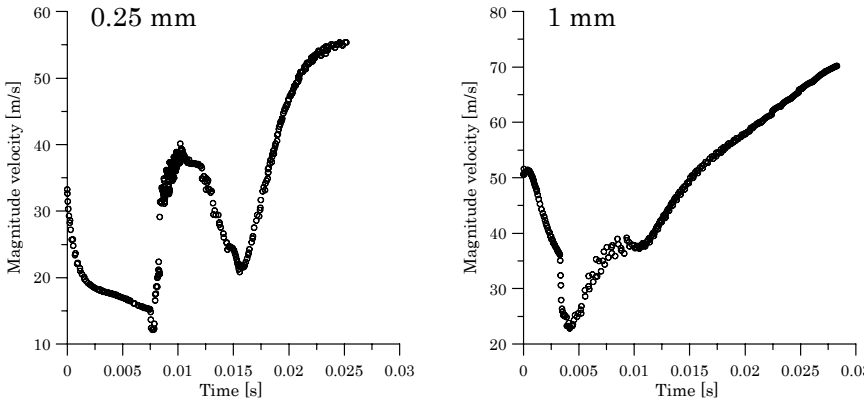

Figure 5–14: Velocity distribution in the 0.25 mm clearance gap on the left and 1 mm on the right.

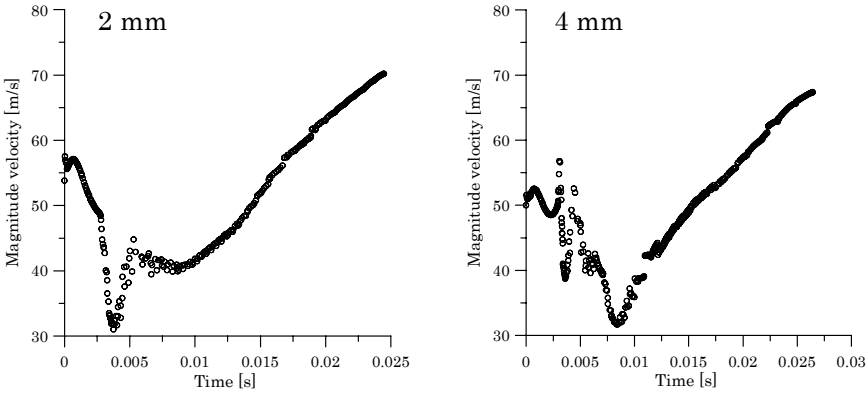

Figure 5–15: Velocity distribution in the 2 mm clearance gap on the left and 4 mm clearance gap on the right.

Thus far, the velocity in the clearance gap and in the guide vane channel has been investigated to substantiate the loss related to the disturbance of the main flow. The actual value of the loss related to the disturbance of the main flow is difficult to calculate and has not been estimated in this thesis. However, the loss related to the actual loss of water is quite simple to calculate. The power which can be utilized by a given flow and net head is calculated according to the following equation:

$$P = \rho g Q H \tag{5.1}$$

Correspondingly, the loss in efficiency due to the loss of water can be expressed in terms of the nominal flow rate through the guide vane cascade and the actual loss of water:

$$j_{Leak} = \frac{Q_{Leak}}{Q_{Nom}} \tag{5.2}$$

This term is also recognized as the relative leakage flow, and is plotted against the height of the clearance gap in figure 5–16. The leakage tends towards a linear behaviour with respect to the size of the clearance gap. As shown in figure 5–16, the amount of lost water is not substantial compared to the total flow through the turbine. Thus the loss related to the disturbance of the main flow must have a greater impact on the efficiency.

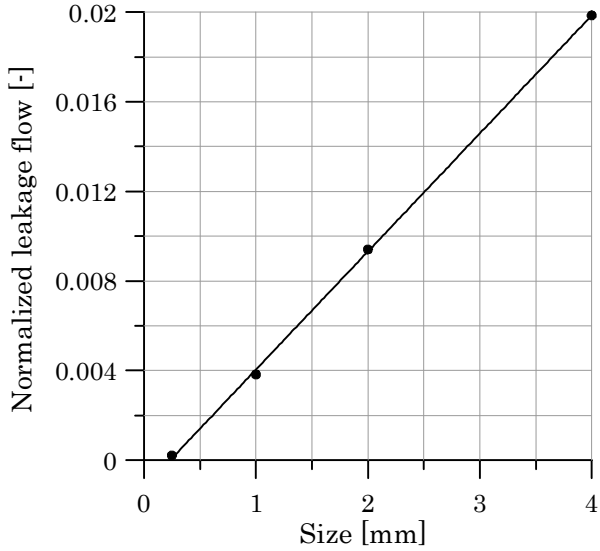

Figure 5–16: Relative leakage flow plotted against the size of the clearance gap.

5.2 Validation

In any numerical computation it is imperative to validate the results in order to establish trustworthy results. And especially flow computations involving large gradients are vital to evaluate. Consequently, the mesh resolution and the chosen solver is further examined in the following subchapters. In addition, an analytical interpretation of the flow condition in the clearance gap is included to further investigate the validity of the numerical computation.

5.2.1 Convergence

The first 100 iterations were carried out with the first order upwind discretization scheme[1]. However, for flows with large gradients first order upwind discretization scheme should be avoided due to excessive smoothing of the results [30]. Thus the remaining part of the iteration process was

conducted by means of the second order upwind discretization scheme. And the convergence of the solutions was monitored by looking at residuals of mass flow and velocity. In addition, the mass flow balance was also monitored.

5.2.2 Mesh

The flow in the clearance gap is highly turbulent according to the calculated value of the Reynolds number. Accordingly, the computational domain should be properly resolved to account for the pressure and velocity gradients. However, the mesh size can not be smaller than the geometric tolerance, and ordinary this is not a problem. But since the height of the clearance gap is quite small the geometric tolerance plays a dominant role in restriction of the mesh resolution in the clearance gap, especially the 0.25 mm clearance gap [33]. Hence it is difficult to make a proper mesh resolution of the near-wall region. However, the Spalart-Allmaras model has been implemented to use wall functions when the mesh resolution is not sufficiently fine in the near-wall area. Thus the Spalart-Allmaras is a good choice for relatively crude simulations on coarse mesh where accurate turbulent flow computations in the near-wall region are not critical.

Anyway, the final choice of mesh resolution in the clearance gap is validated by comparing the final results with an additional computation of each model, where a finer mesh resolution has been employed. In this case the mesh in the clearance gap was doubled compared to the initial mesh resolution. Fortunately, the differences in result were less than 1%, and the flow pattern was identical. Thus the original mesh resolution was acceptable. Still, the results presented in this thesis is retrieved from the latest grid resolution.

5.2.3 Solver

Initially, the Spalart-Allmaras was chosen to compute the flow in the guide vane. But to validate this choice of solver, the standard k-ε solver was employed for the model corresponding to the 1 mm clearance gap. Similar to the previous particle injections, three particles were also dropped in the model, in which the k-ε solver was used. The result is presented in figure

1. Fluent may experience some problems with obtaining a converged solution if the iteration is initiated with a second order discretization scheme.

5–17, where both the results from the Spalart-Allmaras and the k-ε solver are shown for the purpose of comparison. The particle trajectories in the two different models exhibit quite similar tendency. However, to better point out any differences in result, the magnitude velocity is plotted against the elapsed time in figure 5–18 and figure 5–19.

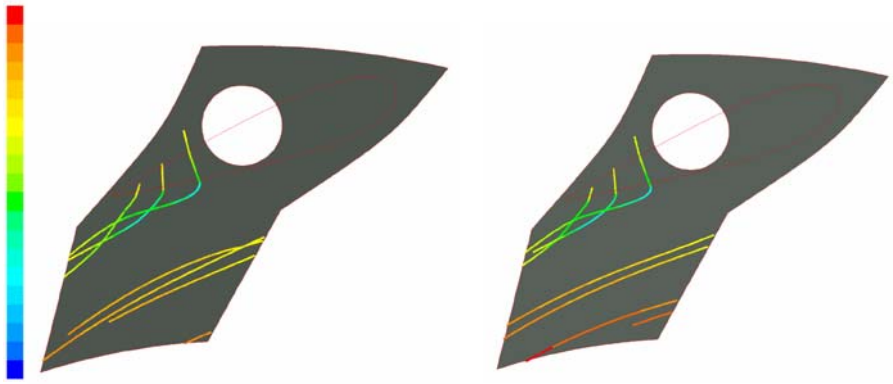

Figure 5–17: Particle traces coloured by velocity magnitude. Spalart-Allmaras on the left and k-ε model on the right.

In accordance with figure 5–17, the particle trajectories, calculated by both the solvers, exhibit quite similar tendency. However, the Spalart-Allmaras arrives at a somewhat higher absolute value of the magnitude velocity than the k-ε solver, corresponding to a 10% higher value.

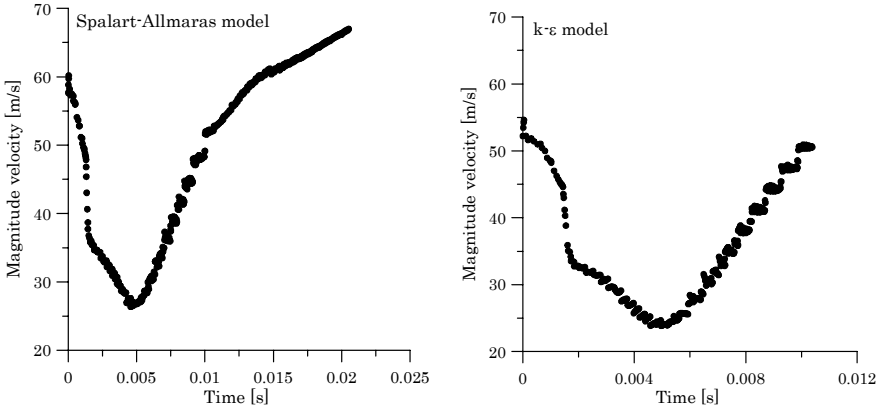

Figure 5–18: Development of the magnitude velocity of the first particle drop, close to the guide vane shaft.

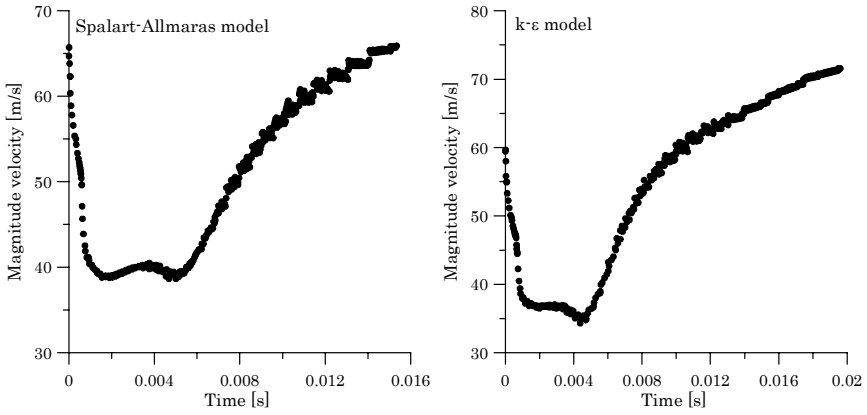

Figure 5–19: Development of the magnitude velocity of the second particle drop.

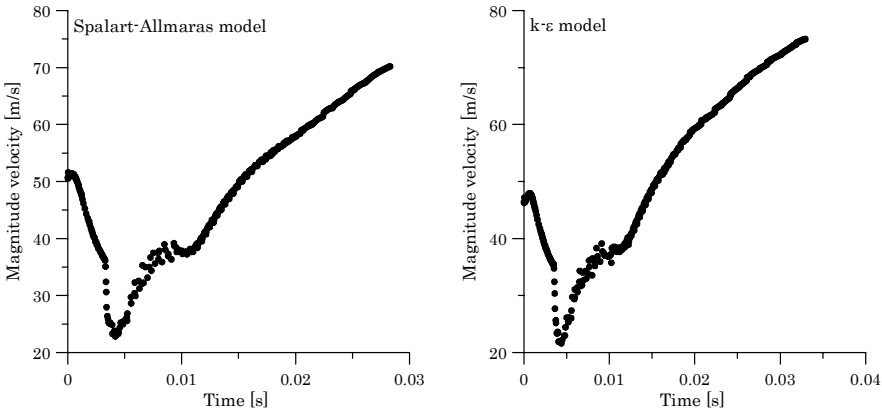

Figure 5–20: Development of the magnitude velocity of the third particle drop, close to the outlet of the guide vane.

5.3 Analytical interpretation

The flow in the clearance gap is quite complicated due to the smallness of the gap, when considering the boundary layer and the substantial viscous effect. The importance of validating the chosen mesh resolution is obvious, but it will also be valuable to relate the flow condition to simplified analogous flow models, which are based on differentiating the continuity, momentum and energy equation.

5.3.1 Flow between two fixed plates

In this case the secondary flow between the head cover and the guide vane facing plate is compared to the well documented Couette flow between two fixed plates. The Couette flow can be explained by considering the viscous flow between two parallel plates a distance 2h apart, as illustrated in figure 5–21. The plates are fixed and assumed to have an almost infinite length and with, so that the flow is essentially axial and fully developed [16]. In this case the flow is induced by the pressure gradient in the x-direction, analogous to the pressure gradient from pressure side to suction side in the guide vane channel.

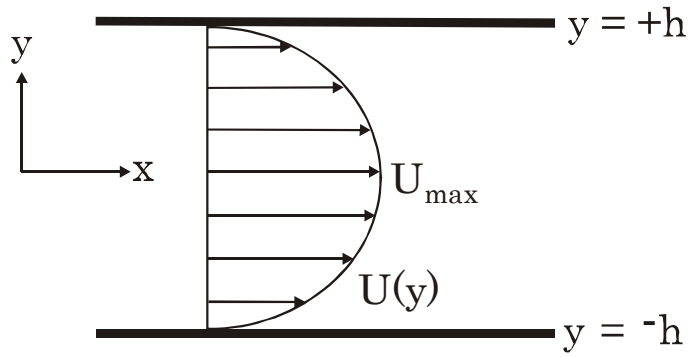

Figure 5–21: Incompressible viscous flow between two fixed plates.

Since the flow is considered to be axial, the velocity component in the x-direction differs from zero while the velocity components v and w in respectively y- and z-direction equals zero. Also, this flow model is regarded as a two-dimensional problem, thus $\delta/\delta z = 0$. And by relating these assumptions to the continuity equation we get the following relation:

$$\Delta \bullet V = \frac{\partial u}{\partial x} + \frac{\partial v}{\partial y} + \frac{\partial w}{\partial z} = 0 \Rightarrow \frac{\partial u}{\partial x} = 0 \tag{5.3}$$

Since the derivative of the remaining velocity component with respect to x equals zero, the velocity can only be a function of y, thus u = u(y). In order to relate the pressure to the velocity, the Navier-Stokes momentum equation is employed:

$$\rho \frac{d\vec{V}}{dt} = \rho \vec{g} - \vec{\nabla} p + \mu \vec{\nabla}^2 \vec{V} \tag{5.4}$$

Since this flow condition is regarded as a two-dimensional problem, the z-component of the Navier-Stokes momentum equation is omitted. The x-component of this equation, however, leads to the following expression:

$$\rho\left(u\frac{\partial u}{\partial x}+v\frac{\partial u}{\partial y}\right) = -\frac{\partial p}{\partial x}+\rho g_x+\mu\left(\frac{\partial^2 u}{\partial x^2}+\frac{\partial^2 u}{\partial y^2}\right) \tag{5.5}$$

And since the gravity is neglected the final expression is given as:

$$\mu\frac{d^2 u}{dy^2} = \frac{\partial p}{\partial x} \tag{5.6}$$

The only term left in the y-momentum equation, when gravity is neglected, is:

$$\frac{\partial p}{\partial y} = 0 \tag{5.7}$$

According to equation 5.7 the pressure is only a function of x, thus p = p(x). Based on this, equation 5.6 can be rewritten as:

$$\mu\frac{d^2 u}{dy^2} = \frac{dp}{dx} = const < 0 \tag{5.8}$$

In equation 5.8 dp/dx is said to be constant according to the theory of separation of variables: If two quantities are equal, where each quantity is a function of two different variable, respectively x and y, then they must both equal the same constant. Otherwise they would not be independent of each other [12]. Also, the constant is said to be negative, because the pressure must decrease in the flow direction in order to drive the flow against the resisting wall shear stress.

The solution to equation 5.8 is found by double integration and applying the no-slip condition at each wall to calculate the integration constants, and the final expression is then given by equation 5.9.

$$u = -\frac{dp \cdot h^2}{dx \cdot 2\mu}\left(1 - \frac{y^2}{h^2}\right) \tag{5.9}$$

The flow forms a Poiseuille parabola of constant negative curvature, where the maximum velocity occurs at the center line y = 0:

$$u_{max} = -\frac{dp \cdot h^2}{dx \cdot 2\mu} \tag{5.10}$$

The wall shear stress is found according to the definition of a newtonian fluid [16]:

$$\tau_{wall} = \tau_{xy,\,wall} = \left(\frac{\partial u}{\partial y} + \frac{\partial v}{\partial x}\right)\Bigg|_{y = \pm h} \tag{5.11}$$

And by employing this definition to the derived expression of the velocity profile between the two fixed plates, the following relation is deduced:

$$\tau_{wall} = \pm\frac{dp}{dx}h = \mp\frac{2\mu u_{max}}{h} \tag{5.12}$$

In this particular case, the wall shear stress in the clearance gap is calculated according to equation 5.12, and compared to the shear stress obtained from the numerical result.

Since the corresponding length and with of the clearance gap is far from infinite, the assumption of a pure axial flow fails. However, if the theory from the Couette flow modelling is employed at the outlet of the clearance gap, where the flow has been able to develop, the error due to the false assumption will be reduced to a minimum. This is because the flow at the outlet is closest to a fully developed flow. Although the result from the Couette flow calculation is a rough estimate, it will give an indication of the validity of the numerical results.

5.3.2 Shear stress in the clearance gap

Consider two paths in the middle of the clearance gap from the pressure side to the suction side near the trailing edge, as illustrated in figure 5–22.

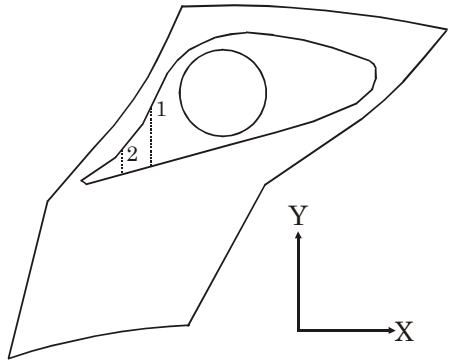

Figure 5–22: Sketch of a head cover illustrating the region where the shear stress is considered.

According to the second term in equation 5.12, the pressure gradient in the flow direction is to be calculated to estimate the shear stress in the clearance gap. Subsequently, the static pressure at path one and two in figure 5–22 is plotted against the y-coordinate[2] in figure 5–23. The static pressure tends towards a linear behavior with respect to the y-coordinate. Thus the pressure gradient is simply found as the value of $\Delta p/\Delta y$. And then the estimated value of the shear stress at path 1 and path 2 respectively reads 1250 Pa and 1420 Pa.

However, the third term in equation 5.12 suggests a different approach to calculate the shear stress, with respect to the velocity. The results from this calculation are plotted against the y-coordinate at the left in figure 5–24. Furthermore, the shear stress from the numerical computation is retrieved along the similar paths at the wall, and plotted at the right in

2. The x-coordinate in equation 5.3 corresponds to the y-coordinate in the numerical modelling. And the y-coordinate in equation 5.3 corresponds to the z-coordinate in the numerical modelling. Thus the z-coordinate in equation 5.3 corresponds to the x-coordinate in the numerical modelling.

figure 5–24. The numerical value of the shear stress is quite larger than both the analytical calculation.

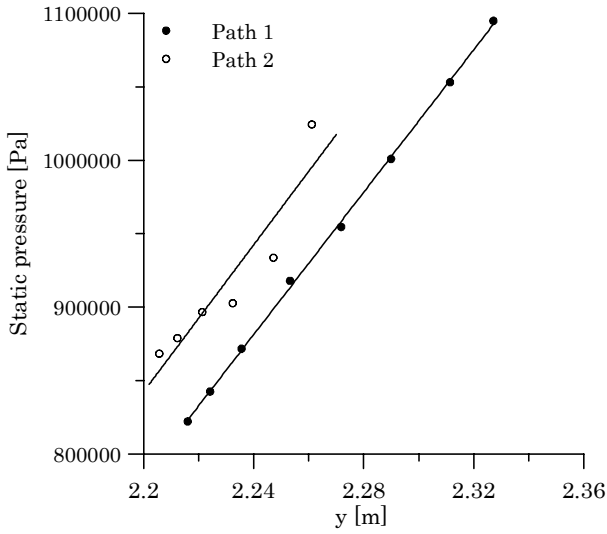

Figure 5–23: Static pressure distribution in the clearance gap.

The first analytical computation estimates a constant value of the shear stress, because the pressure gradient and the height of the clearance gap is a constant. The numerical results, on the other hand, reports a decreasing shear stress as the flow approaches the suction side. The absolute value of the shear stress obtained from the second term in equation 5.12 agrees more with the numerical result, than the results obtained from the third term in equation 5.12. This can be explained by remembering that the derivation of the third term is based on a second assumption, in which the velocity is assumed to attain the highest value in the middle of the clearance gap. However, the last computation of the shear stress exhibits a similar trend as the shear stress obtained from the numerical result.

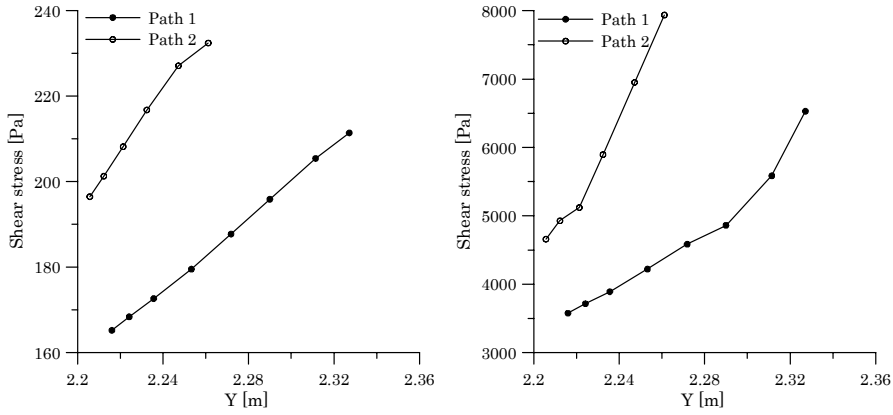

Figure 5–24: Calculated shear stress at the left and the shear stress obtained from the numerical calculation at the right.

And for the purpose of comparison, the ratio between the numerical value and the second analytical calculation is plotted against the y-coordinate in figure 5–25. And as was assumed, the difference between the numerical result and the analytical calculation attains the lowest value at the outlet of the clearance gap, where the flow has been able to develop the most.

The ratio at the outlet is still quite considerable. However, the smallness of the height of the clearance gap combined with the large velocity provokes a quite complicated flow situation. The smallness of the clearance gap might also cause an interaction between the viscous boundary layer at respectively the guide vane facing plate and at the head cover [34]. Thus a further investigation of the velocity in the clearance gap is performed to emphasize the validity of the analytical interpretation of the flow in the narrow clearance gap. Accordingly, the velocity in respectively x-, y- and z-direction is plotted against the y-coordinate, to compare the values with the assumptions made when the analytical model is developed.

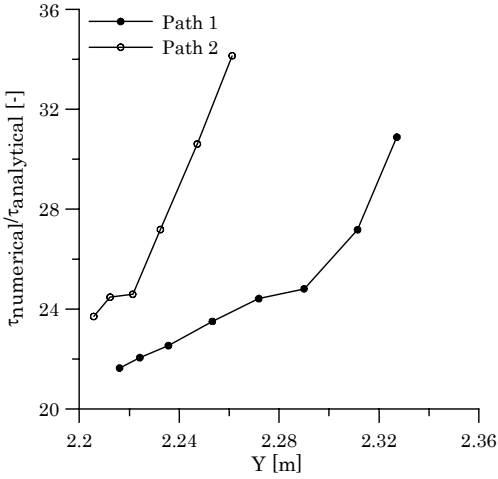

Figure 5–25: The ratio between the numerical shear stress and the second analytical calculation.

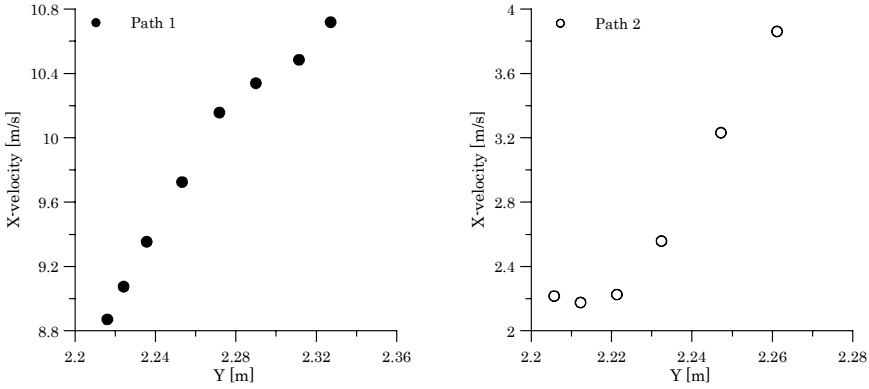

Figure 5–26: The x-velocity at respectively path 1 and path 2.

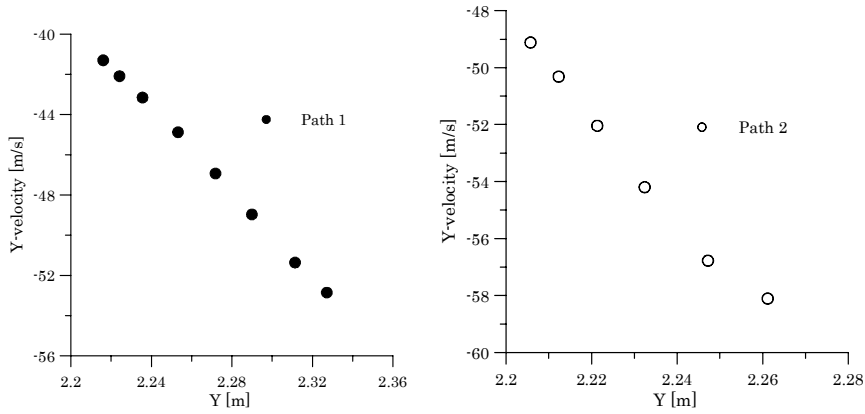

Figure 5–27: The y-velocity at respectively path 1 and path 2.

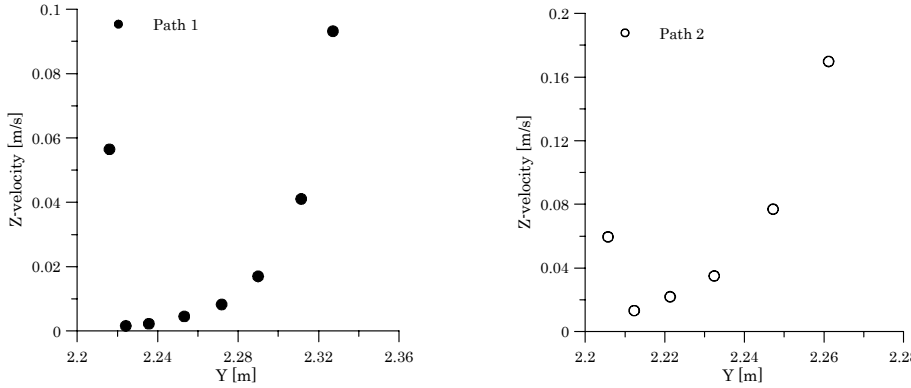

Figure 5–28: The z-velocity at respectively path 1 and path 2.

According to the analytical model the velocity in the x- and z-direction should equal zero. Also, the velocity in the y-direction is assumed to be a constant with respect to y. In the first plot, nearest to the guide vane shaft, the x-velocity varies between approximately 9-10 m/s with respect to the y-coordinate. In the second plot, however, the x-velocity only varies between roughly 4-2 m/s. Still, the x-velocity in neither of the two plots are zero. However, the velocity in the z-direction in both the plots is approximately zero, as shown in figure 5–28. Furthermore, the plot in figure 5–27 clearly shows that the y-velocity does not equal a constant. Instead, the velocity in

plot 1 and plot 2 respectively differs between 50-40 m/s and 60-50 m/s. Also, the velocity at the inlet of the clearance gap varies with the radius, as can be seen by comparing the velocity at the two different plots in figure 5–26 through figure 5–28. Hence the flow in the clearance is a complete 3-D problem.

Finally, by considering the vector plot of the magnitude velocity, in for instance figure 5–4, one can see that the velocity in the clearance gap deviates from the vertical direction, represented by the y-axis. Hence the flow direction is not represented by the y-coordinate, as was assumed when the analytical calculation was performed. However, since the velocity components in the x- and z-direction are comparably small, the assumption of a pure vertical flow is employed to simplify the problem. Otherwise, a new coordinate system based on the actual flow direction had to be made.

Thus the assumptions in which the analytical model is based on is only partially fulfilled in the clearance gap. Accordingly, one can not expect the analytical calculation of the shear stress to agree with the numerical computation.

However, the plot in figure 5–25 clearly indicates an increasing consistence as the flow approaches the suction side. This implies that the flow is closer to a fully developed state at the suction side, and the analytical interpretation of the flow on the suction side predicts a more accurate value of the shear stress. Still, as mentioned above, the difference between the numerical shear stress and the analytical shear stress at the suction side is quite large. But by regarding the substantial differences between the flow in the clearance gap and the flow between two fixed plates, this large ratio can be justified.

5.4 Concluding remarks

Primarily, it should be mentioned that since the four individual clearance gaps are constant in each model, the actual increasing clearance gap towards decreasing radius is not accounted for. This modelling approach is chosen for the purpose of simplification.

The results from the numerical computation indicate a strong influence from the leakage on the main flow in the guide vane channel. The results also show a quite worsened flow situation as the clearance gap increases.

And in cases of heavy deterioration due to sand particles in the flow, the clearance gap between the guide vane and the head covers increases rapidly due to a substantial interaction between the vortex flow and the sand particles. This relation makes it imperative to reduce the initial clearance gap to an absolute minimum in order to avoid a constantly increasing clearance gap. And in order to achieve this, a careful choice of material and head cover design has to be made to keep the deformation on a minimum. Accordingly, it will be vital to develop a numerical tool, which predicts the head covers deformation within a certain order of accuracy.

6 Conclusions

The different losses developed in a high head Francis turbine are presented in this thesis in order to put the loss in the guide vanes in perspective. This analysis showed that the leakage loss contributed to a rather substantial part of the total loss developed in a high head Francis turbine. The covers deflection is the primary cause of the leakage flow in the guide vane. And in the presented work a numerical modelling of the head covers deflection is performed in both a 3-D and a 2-D view. The main purpose of the additional 2-D analysis was to develop a simplified and less time-demanding numerical approach. Despite the substantial simplification considering the analysis of the 2-D models, the results from the 2-D analysis show good agreement with the 3-D results. Thus a 2-D modelling of the head covers deflection may be employed to obtain reliable results in predicting the head covers deflection.

The results from the finite element analysis reported a decreasing deflection with increasing unit size, according to the design philosophy. Also, a further examination of the deflection parameter indicates that the angle of deflection does not describe the actual size of the clearance gap. And this relation made the basis of a further investigation of the absolute translation. And as was expected, a further investigation of the absolute translation showed an increasing translation with increasing unit size. And since the absolute translation describes the actual extent of the clearance gap, the leakage flow is expected to increase with increasing unit size, which is in conflict with the current design philosophy.

Results from efficiency measurements with different clearance gaps and also efficiency measurements of eroded and repaired turbines are included to underline the severity of the clearance gap between the covers and the guide vanes facing plate. These measurements show a clear drop in efficiency as the clearance gap increases.

Also, a numerical calculation of the flow in the guide vanes is presented in this thesis to visualize the effect from the clearance gap. The main objective was to illustrate how sensitive the leakage flow is to the extent of the clearance gap between the head cover and guide vanes facing plate. Consequently, the flow in the guide vanes has been computed with four different clearance gaps, respectively 0.25 mm, 1 mm, 2 mm and 4 mm. The result from this calculation showed that in the case of a 0,25 mm clearance gap, the main flow is barely influenced from the leakage flow. But as the clearance gap is increased the influence on the main flow is clearly enhanced, underlining the importance of keeping the covers deflection on an absolute minimum.

7 Further work

Completing this thesis, a few suggestions regarding future work are included. The main focus is placed on validating both the numerical calculation of the head covers deformation and the numerical calculation of the leakage flow in the guide vanes.

Obviously, it will be of great importance to conduct measurements of the head covers deformation when the power plant is operating. Only based on such measurements a proper and thorough evaluation of the numerical approach is achieved. As the accuracy of the numerical tool is revealed, the tool can be included at the design stage to give an accurate prediction of the head covers deformation.

In addition, it will be of great significance to conduct measurements of the pressure acting on the head cover as the turbine is operating. By doing this, proper knowledge of the pressure distribution is gained. Thus based on such measurements a more accurate pressure distribution may be implemented in the numerical model.

Regarding the leakage flow in the guide vanes, it will be of great interest to carry out measurements of the leakage flow with the purpose of comparing the result with a numerical calculation. Based on these measurements, an accurate numerical approach may be established, involving the right choice of solver and model constants.

The flow in the clearance gap is quite complicated due to the high velocities

and the smallness of the height of the gap. These special features of the clearance gap make it difficult to predict the influence from the boundary layer. Thus a more extensive investigation of flow in narrow gaps should be carried out to better visualize the flow in the guide vanes.

The primary conclusion of this thesis is to keep the deformation of the covers as small as possible, by designing the covers with an adequate stiffness and also achieve a proper prestressing of the covers. However, since the pressure difference between pressure side and suction is said to be the driving force for the cross flow in the guide vanes, a further research on how to reduce this driving force will also be of great interest.

Finally, analysis of the flow in the guide vanes at different loads should also be performed to establish the flow conditions at various loads. This is especially important because it is more and more common to produce electricity at various load operation. Consequently, it is vital to emphasize the loss at different part loads.

Bibliography

[1] Hermod Brekke. Grunnkurs i hydrauliske strømningsmaskiner. Lecture notes, NTNU, Trondheim, Norway, 1998. In norwegian.

[2] Hermod Brekke. Undersøkelse av ledeapparatet for turbinene til Svartisen. Lecture V.R Bergen 1991.

[3] Hermod Brekke. Konstruksjon av pumper og turbiner. Lecture notes, NTNU, Trondheim, Norway, 1998. In norwegian.

[4] A.F. Mills. Heat and mass transfer. Richard D. Irwin, Inc., 1995, USA, ISBN 0-256-11443-9.

[5] Hermod Brekke. Analysis of losses in hydraulic turbines, Hydropower Conference, Lausanne, July 1996.

[6] Hermod Brekke. Pumper og turbiner. Lecture notes, NTNU, Trondheim, Norway,1999. In norwegian.

[7] Hermod Brekke. The influence of the guide vane clearance gap on efficiency scale effect. IAHR Symposium, September 1990, Beograd.

[8] Hermod Brekke. The influence from guide vane clearance gap on efficiency and scale effect for Francis turbines. 14 IAHR Symposium, Trondheim, 1988.

[9] Reiner Mack, Peter Drtina and Egon Lang. Numerical prediction of erosion of guide vanes and in labyrinth seals in hydraulic turbines.

[10] Marit Bjordal. Erosion and corrosion of ceramic-metallic coatings and stainless steel. Ph.D thesis, Norwegian university of science and technology, 1995.

[11] Niels Ottosen and Hans Petersson. Introduction to the finite element method. Prentice Hall,. New York, 1992.

[12] Algor User's Guide, Software documentation, 2003.

[13] Sølvi Eide and Ole G. Dahlhaug. Analysis of the leakage flow and wear in guide vanes. The IAHR conference, Lausanne, Switzerland, 2002.

[14] Edwards & Penney. Calculus, 4. edition. Prentice Hall 1994.

[15] Fridtjov Irgens. Fasthetslære. Tapir forlag, Trondheim, 5. edition, 1996. ISBN 82-519-1212-1.

[16] Erwin Kreyszig. Advanced engineering mathematics, 7. edition. John Riley & Sons. Inc, 1993.

[17] Geir Holm. Innflytelse på virkningsgradsskalaeffekten fra ledeskovlklaringene mot trommelokkene på høytrykks Francis-turbiner. Project work, Norwegian university of science and technology, 1994.

[18] Frank M. White. Fluid Mechanics. McGraw-Hill, Inc., New York, third edition, 1994. ISBN 3-540-59434-5.

[19] Roar Vennatrø. An experimental and theoretical analysis of non-steady turbulent flow in circular smooth pipes. Ph.D thesis, Norwegian university of science and technology, 2000.

[20] Fluent Inc. Fluent 5 User's Guide, volume 2. Fluent Inc. Lebanon, NH 03766, USA, August 1998.

[21] B.E. Launder and D. B. Spalding. The numerical computation of turbulent flows. Computer methods in applied mechanics and engineering, 3:269-289, 1974.

[22] Mats Conny Larsson. Experimental and theoretical analysis of inlet flow of a Francis Turbine Runner. Ph.D thesis, Norwegian university of science and technology, 2003.

[23] Jr. John D. Anderson. Computational fluid dynamics; The basics with applications. McGraw-Hill, Inc,. New York, NY 10020, 1. edition, 1995.

[24] H. Tennskes and J. L. Lumley. A first course in turbulence. The MIT Press, Massachusetts, 1972, ISBN 0-262-20019-8.

[25] Frank M. White. Viscous Fluid Flow. McGraw-Hill, Inc., New York,

third edition, 1994, Second edition, ISBN 0-07-100995-7.

[26] Li Xue-Zhong. Guide vane erosion ta Mao Tiao He. Waterpower & Dam Construction, February, 1982.

[27] Hermod Brekke. Design of hydraulic machinery working in sand laden water. Published in Abrasive Erosion & Corrosion of Hydraulic Machinery, vol. 2 edit by C.G Duan and V.Y Karelin. Imperial College Press, 2002 London.

[28] Xin Chen. Theoretical and experimental study of flow through the double cascade of a Francis turbine. Ph.D thesis, Norwegian university of science and technology, 1992.

[29] H. Brekke, C. Xin and J.T Billdal. A study of the guide vane flow and the influence from the leakage flow. IAHR Symposium, Sao Paulo, 14. September 1992.

[30] Gotfred Severin Berntsen. Numerical analysis of the two-phase Pelton jet flow using a single-phase model and analytical discussions of the Pelton jet surface break-up phenomenon. Ph.D thesis, Norwegian university of science and technology, 2002.

[31] Moore. J and Tilton. J. S. Tip leakage flow in a linear turbine cascade, Journal of Turbomachinery, ASME, Vol. 110, January 1988, pp. 18-26.

[32] Storer. J and Cumpsty. N. A. Tip leakage flow in axial compressors, ASME Paper NO. 90-GT-127.

[33] Fluent Inc. Gambit 1, Modeling Guide. Lebanon, NH 03766, USA, May 1998.

[34] Junichi Kurokawa and Masato Sakuma. Flow in narrow gap along an enclosed rotating disk with through-flow.

Appendix A

A Paper presented at IAHR 2002

ANALYSIS OF THE LEAKAGE FLOW AND WEAR IN GUIDE VANES

Sølvi Eide Ph.D. Student at the Norwegian University of Science and Technology, Trondheim, Norway
Ole G. Dahlhaug Associate Professor at the Norwegian Institute of Science and Technology

ABSTRACT

The losses due to the secondary leakage flow in the guide vanes of Francis turbines represents a relative large part of the total loss of the turbine efficiency. This leakage flow arises due to the head covers deflection, which increases the gap between the guide vanes and the head cover, when it is pressurized.

A 2-D simulation of a pressurized head cover will be introduced in this paper. The simulation, based on finite element method, is performed in the software program Algor. This simulation gives the stress distribution and the displacement of the pressurized head cover. The displacement results obtained from the simulation will be used to calculate the deflection of the head cover. Since the calculation time and the preliminary work are highly reduced it is preferable to run a 2-D simulation instead of a 3-D simulation. Furthermore the validity of the 2-D simulation will be analyzed when compared to a complete 3-D simulation.

In order to establish the influence from the clearance gaps on the turbine efficiency, previous measurements of the efficiency at different clearance gaps will be presented in this paper.

Since the clearance is also influenced by the wear of the guide vanes, previous measurements of the turbine efficiency on sand eroded and repaired turbines are presented. These measurements show the importance of reducing the possibilities of wear from a design point of view and also the importance of repairing any raised erosion.

RESÚMÉ

Les pertes de fuite dues à l'écoulement secondaire dans le disributeur des turbines de Francis représentent une grande partie relative à toute les pertes de la turbine. Cet écoulement surgit en raison dû à la déflexion du fond superieur, qui augmente l'espace entre les aubes directrice et la flasque superiur, le moment où il est pressurisé.

Un 2-D simulation d'un fond superieur pressurisée sera présenté en cet article. La simulation, basée sur la méthode d'élément fini, est effectuée avec le logiciel Algor. Cette simulation donne la distribution des efforts supportés et le déplacement du fond superieur pressurisée.

Les résultats de déplacement obtenus à partir de la simulation seront employés pour calculer la déflexion du fond superieur. Depuis le temps de calcul, et le travail préliminaire sont fortement réduits, il est préférable de courir un 2-D simulation au lieu d'un 3-D simulation. En outre la validité du 2-D simulation sera analysée quand comparé à un 3-D simulation complet.

Afin d'établir l'influence des lacunes de dégagement sur le rendement de la turbine, des mesures précédentes de l'efficacité à différentes espace de dégagement seront présentées en cet article. Puisque cet espace de dégagement est également influencé par l'usure du distributeur, des mesures précédentes de l'efficacité de turbine sur

la turbine érodée de sable sont présentées. Ces mesures montrent l'importance de réduire les possibilités d'usure d'un point de vue de conception et également l'importance de réparer n'importe quelle érosion manifesté.

NOMENCLATURE

Term	Symbol	Definition
Deflection	Z [m]	
Angel of deflection	Φ [rad]	
Height of the runner	B [m]	
Absolute velocity	C [m/s]	
Angular velocity	ω [rad/s]	
Flow rate	Q [m^3/s]	
Diameter	d [m]	
Diameter of the shaft	D [m]	
Area of the crossectional area	A [m^2]	
Radius	r [m]	
Absolute tangential velocity	c_u [m/s]	
Absolute meridional velocity	c_m [m/s]	
Gravitational constant	g [m/s^2]	

INTRODUCTION

The demand of energy and power is constantly increasing, and this makes it important to exploit the already existing hydropower installation to the fullest extent. To achieve this one have to emphasize the losses connected with the operation of the turbine and make use of technology which reduce the losses. In addition to friction and impact loss the leakage flow in the guide vanes is a part of the main losses developed in the turbine. As shown in figure 3 the efficiency is highly depending on the clearance gap, and this relation makes it vital to identify the extent of the clearance gap. It is on the basis of this knowledge one can decide how to do the proper repairs.

The main objective of this work is to validate the numerical 2-D simulation as a tool to predict the deflection of the head cover. A cross section of a Francis turbine and the location of the head cover is shown in figure 1. It should also be mentioned that the head cover in figure 1 is made of ribs, and is not solid as the head cover in this paper. As shown in figure 3 the mentioned leakage flow will be significant with a proven drop in efficiency. The secondary leakage flow does not only reduce the efficiency because of lost water, it also disturbs the main flow in the runner. This is because it flows across the main flow from the pressure side to the suction side and creates a swirl flow. In figure 2 the flow pattern of the leakage is illustrated.

The leakage is governed by the extension of the gap between the guide vanes and the head cover, and the available net head. When the head and bottom covers and the guide vanes are designed it is originally made with a certain clearance gap to prohibit grinding. But when the turbine is pressurized the originally gap, and hence the leakage flow, increases. This gap-increase is mainly a function of the net head, but it is also influenced by the dimensions and the wear of the machinery.

The high head Francis turbines are exposed to serious wear from sand erosion due to the high velocities and accelerations. The wear of the machinery caused by sand particles in the flow can make an uneven increased gap surface between the head covers and guide vanes, and further increase the gap.

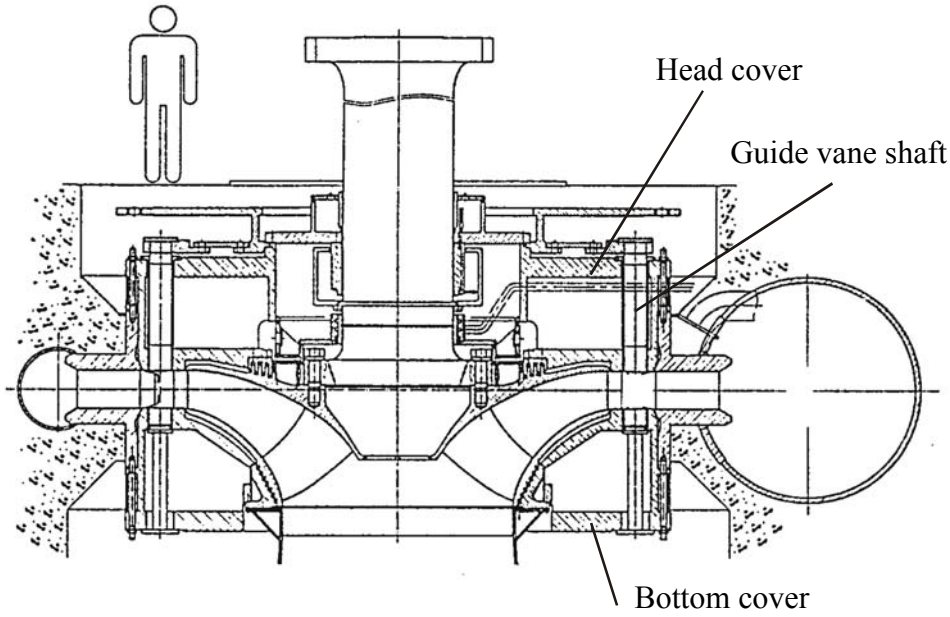

Fig. 1 Francis turbine

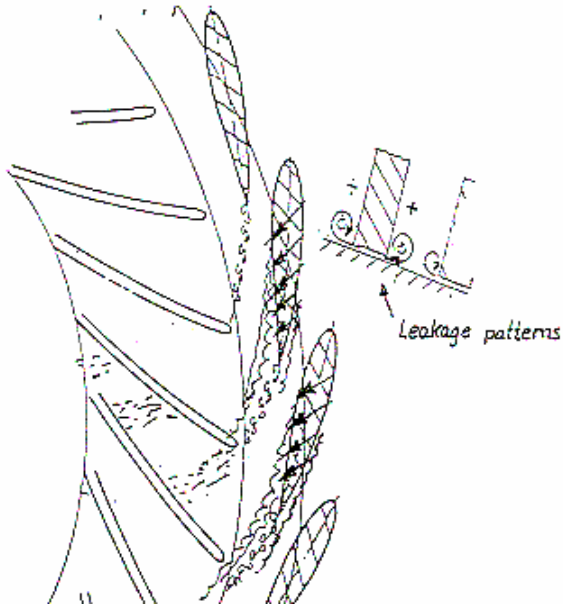

Fig. 2 Leakage patterns in the guide vanes Hermod Brekke (Ref. 3).

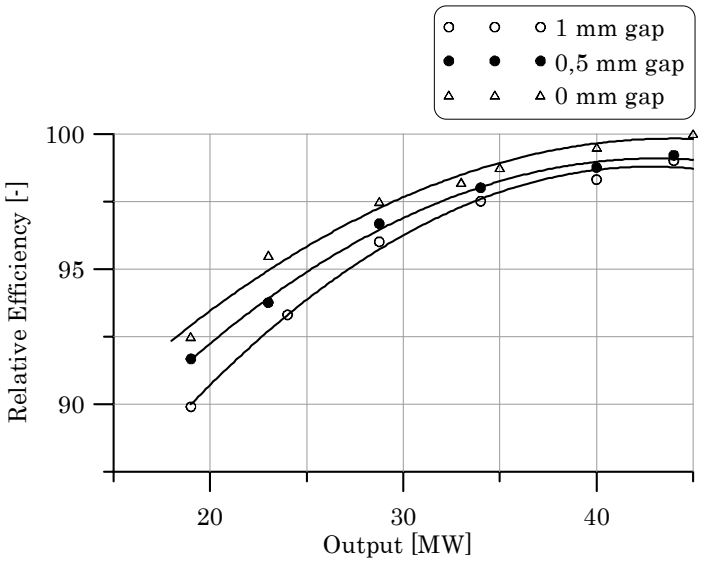

Fig. 3 Efficiency test with different clearance gaps Hermod Brekke (Ref. 2).

MODELLING IN ALGOR

As mentioned in the abstract the numerical calculation of the displacement of the head cover is made in Algor. This numerical program uses the FEM (Finite Element Method) to calculate the stress and displacement of the given pressurized geometry. When numerical computation is carried out it is adequate to make some simplifications of the geometry. If these simplifications are done properly a significant gain in calculation time can be achieved without effecting the result too much. In addition there are some simplifications which are necessary to perform when a 2-D axe symmetrical simulation of a geometry, which is not axe symmetrical, is executed. In this particular case the geometry is made with 24 holes where the 24 guide vanes are located. In order to run a 2-D simulation these holes are neglected and the head cover is completely solid with forces acting on every nodes.

Because there are no stress gradients involved in this simulation the demand of a fine mesh to get reliable results, is diminished. Despite this condition, two different meshes are generated, where the second mesh is twice as fine as the first mesh. The simplified geometry is considered to be axe symmetrical and has a finite thickness of one radian.

CALCULATION OF THE FORCES ACTING ON THE HEAD COVER

The head cover is divided into three different regions where different formula is used to calculate the values of the forces acting on the head cover. The net head of this particular turbine is 435 m and the nominal flow is about 7.7 m3/s and accordingly the power is about 25 MW. From the inlet to the outlet of the guide vanes there

are no rotational parts and the static pressure in every node made by the mesh is calculated according to Bernuollis equation:

$$h_{Static} = H_{Stagnation} - \frac{1}{2}\frac{c^2}{g}$$

where $c^2 = c_u^2 + c_m^2$ and $c_m = Q/A = Q/(2\pi rB)$

Furthermore $H_{Stagnation}$ is the total local pressure, thus $H_{Stagnation}$ is a constant according to Bernoulli. From the inlet of the runner to the radius where the labyrinth sealing begins the following formula, based on Newtons second law, is used to calculate the pressure distribution on the different nodes:

$$h_{i+1} = h_i - \frac{\omega^2\left(r_i^2 - r_{i+1}^2\right)}{8g}$$

Across the labyrinth seals the pressure distribution is considered to be linear and therefore a function of the radius. The pressure at the end of the seal is assumed to be equal to the cool water pressure, which is 20 m in this case.

The calculated forces at every node are implemented in Algor and the 2-D axe symmetrical simulation gave the displacement results given in figure 4. The displacement at the guide vane shaft (Point 1 and 2 in figure 4) is obtained from the result and the deflection of the head cover is calculated from the following formula:

$$\arctan\phi = \frac{z_1 - z_2}{D}$$

RESULTS FROM THE 2-D SIMULATION

In figure 4 both the displaced geometry and the indisposed geometry is shown in order to illustrate how the head cover deflects. It should be mentioned that the displacement of the geometry in figure 4 is scaled in order to see how it deflects. Table 1 clearly indicates that there is little to gain by generating a finer mesh. The lower displacement of the coarse meshed geometry is due to the fact that a coarse meshed geometry acts as a stiffer body when finite element analysis is performed.

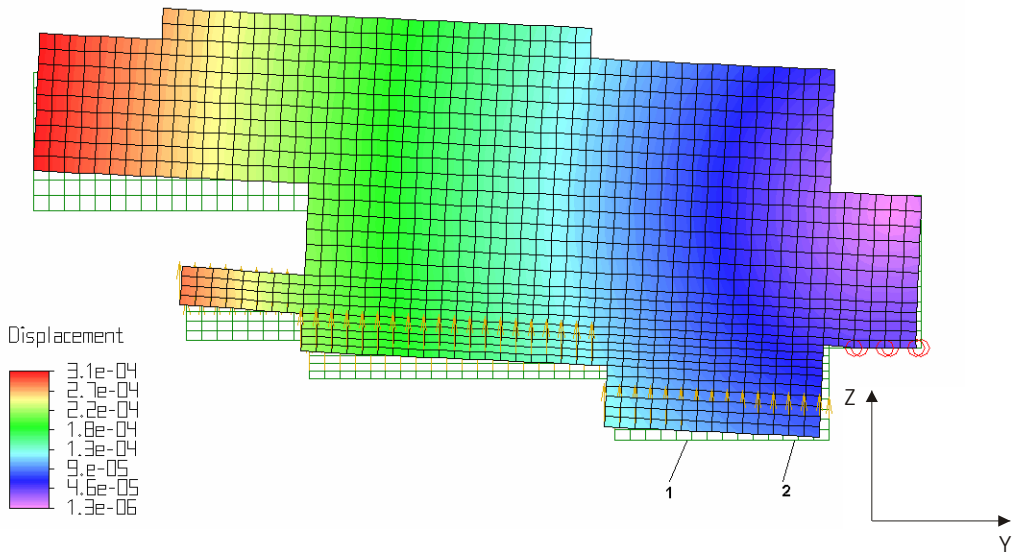

Fig. 4 Displacement contours of the head cover.

Mesh	Z_1 [m]	Z_2 [m]	ϕ [radian]
Coarse mesh	1,07E-04	8,49E-05	2,76E-04
Fine mesh	1,12E-04	8,87E-05	2,90E-04

Table 1. Results from the 2-D simulation.

A 3-D simulation has previously been carried out by Geir Holm (Ref. 1) and this gave the deflection results given in table 2. The difference in the results is relatively large, but it can partly be accounted for due to the different ways of modelling. The 3-D simulation was carried out with about 15 percent lower pressure distribution, and also the modelling did not allow for any translation in any direction at the boundary. This assumption does not correspond to the reality, because there will always be some extent of displacement even at the boundary. To emphasize how much this incorrect boundary condition effects the results, a 2-D simulation with this assumption is carried out, and as shown in table 3, quite different results were obtained. The displacement is reduced by a factor of 2 when no translation is permitted at the boundary.

	Z_1 [m]	Z_2 [m]	ϕ [radian]
2D	1,12E-04	8,87E-05	2,90E-04
3D	7,84E-05	3,89E-05	4,90E-05

Table 2. 2-D versus 3-D.

	Z_1 [m]	Z_2 [m]	ϕ [radian]
Translation in Y-direction	1,12E-04	8,87E-05	2,90E-04
No translation is allowed	5,26E-05	3,62E-05	2,05E-04

Table 3. Different boundary conditions.

WEAR IN THE GUIDE VANES

As mentioned in the introduction the high head Francis turbines experience serious damage from sand erosion due to the high velocities and accelerations developed in the turbine. The highest absolute velocities and accelerations arise in the guide vane cascade outlet and at the pressure side of the runner.

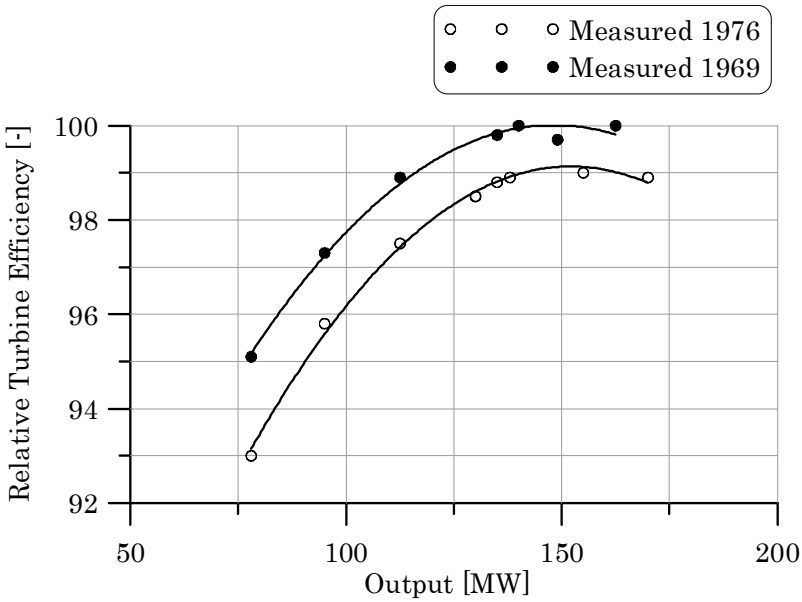

Fig. 5 Efficiency of sand eroded and repaired turbine Hermod Brekke (Ref. 3)

The sand erosion of the turbine in figure 6 caused an erosion of 2 mm, and both figure 5 and 6 shows that there is a lot to gain by repairing the sand eroded turbines.

To minimize the degree of erosion smoothest possible acceleration, reduction of the clearance gap between the guide vanes and the facing plates is recommended in general. In addition a careful choice of the stay vane outlet angles bringing the guide vane in a neutral position at the normal operation point is an important feature to achieve. But when the erosion is a fact, installation of guide vane seals in order to prevent the leakage flow will also reduce the erosion until the turbulence and secondary flow erosion has created a waviness surface between the seals and the facing plates. Figure 7 shows the gain in efficiency when seals have been mounted in the guide vanes.

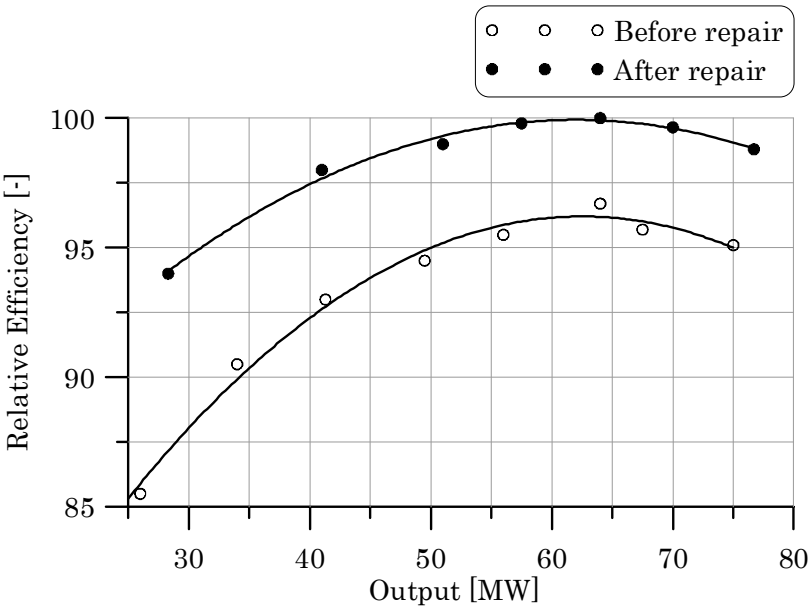

Fig. 6 Efficiency of a sand eroded and repaired turbine Hermod Brekke (Ref. 3)

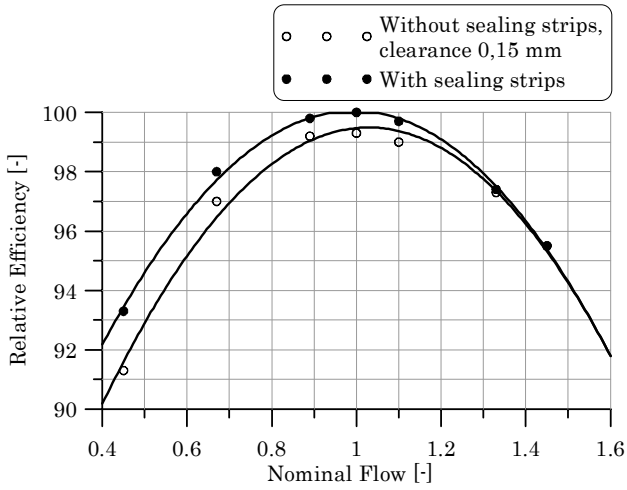

Fig. 7 Efficiency measurements with and without seals Hermod Brekke (Ref. 3).

Nevertheless the best preventive step is to use new materials and particular the ceramic materials, or coatings on the material. As an example the use of a ceramic coating of the guide vanes has been developed for high head Francis turbines. It should however be emphasized that for a new turbine, because of the small clearance, one must be careful when coating the facing plates in order to obtain the necessary tolerances and surface finish Hermod Brekke (Ref. 4).

CONCLUSION

A 2-D simulation of a pressurized head cover in a Francis turbine has been presented in this paper. It has been shown how the head cover deflects when it is pressurized, and the importance of calculating and emphasize the displacement of the head cover is pointed out in figure 5. Furthermore the gain in efficiency by repairing the gap is shown to be highly noticeable. Based on these conclusions simulations of head cover will be an important tool in investigating the amount of deflection.

The 2-D simulation gave displacement results at the same order of magnitude as the previous 3-D simulation, and consequently the 2-D simulation can be a relevant tool in predicting the displacement of a pressurized head cover. Some improvements of the 2-D geometry can be made if the model is made with a smaller E-modulus at the region where the holes for the bolts are supposed to be. One will achieve a more correct overall stiffness of the geometry. All things considered, a 2-D simulation will be a preferable tool in calculating the expected displacement of a head cover already at the design phase. The 2-D simulation is not only preferable due to the simplicity concerning the drawing and meshing of the model, but also because of the fact that the calculating time is seriously diminished compared to a 3-D simulation.

REFERENCES

Ref. 1 Geir Holm, 1994, "The influence from the guide vanes clearance gap on the efficiency scale effect in high head Francis turbines", A project work written in Norwegian at The Norwegian University of Science and Technology.

Ref. 2 Hermod Brekke, "The influence from Guide Vane Clearance Gap on Efficiency and Scale Effect for Francis Turbines", 14th I.A.H.R Symposium, 20-23 June 1988, Trondheim.

Ref. 3 Hermod Brekke, "Inspection of the guide vanes of the turbines installed in Svartisen powerplant", Lecture V.R Bergen, Norway 1991.

Ref. 4 Hermod Brekke, 1992 "Erosion and Corrosion of Hydraulic Machinery. Chapt. 6. Design of Hydraulic Machinery Working in Sand Laden Water.

Appendix B

B Paper presented at IAHR 2004

ANALYSIS OF THE HEAD COVERS DEFLECTION AND THE LEAKAGE FLOW IN THE GUIDE VANES

Sølvi Eide Ph.D. Student at the Norwegian University of Science and Technology, Trondheim, Norway
Hermod Brekke Professor Emeritius at the Norwegian Institute of Science and Technology

Abstract

The losses due to the secondary leakage flow in the guide vanes of Francis turbines represent a relative large part of the total loss developed in the turbine. This leakage flow arises due to the head covers deflection, which increases the gap between the guide vanes and the head cover, when it is pressurized.

A 2-D simulation of 20 pressurized head covers will be introduced in this paper. The simulation, based on finite element method, is performed by use of the software program Algor. This simulation gives the stress distribution and the displacement of the pressurized head covers. The displacement results obtained from the simulation will be used to calculate the angle of deflection of the head cover. The validity of the 2-D simulation will be analyzed when compared to a complete 3-D simulation of the same head covers. A 2-D analysis is preferable compared to a 3-D analysis, because the computer time and the preliminary work are highly reduced.

Since the extent of the clearance gap is highly influenced by the wear of the guide vanes and covers, previous measurements of the turbine efficiency on sand eroded and repaired turbines are presented. These measurements show the importance of reducing the possibilities of wear from a design point of view and also the importance of repairing surfaces exposed to wear.

In addition to measurements of sand eroded turbines, efficiency measurements of covers with different clearance gaps are presented. According to both of these results the efficiency is highly influenced by the extent of the clearance gap, and therefore a numerical computation of the flow in the guide vanes with four different clearance gaps will be presented in order to emphasise how sensitive the leakage flow is to the extent of clearance gap.

Résumé

Les pertes dues au débit secondaire de fuite dans les aubes directrices de turbine Francis représentent une grande partie relative à la perte totale développée dans la turbine. Ce débit de fuite surgit à cause de la déflexion du fond supérieur qui augmente l'espace entre les aubes directrices et le fond supérieur, quand il est sous pression.

Une simulation à 2-D de vingt fonds supérieurs sous pression sera présentée dans cet article. La simulation, basée sur la méthode des éléments finis, est effectuée au moyen du logiciel "Algor". Cette simulation donne la distribution des tensions dues au déplacement des fonds supérieurs. Les résultats de déplacement obtenus à partir de la simulation seront employés pour calculer la déflexion du fond supérieur. La validité de la simulation à 2-D sera analysée et comparé avec une simulation à 3-D appliquée sur le même fond supérieur. L'analyse à 2-D est préférable comparée à l'analyse à 3-D, parce que la durée du calcul numérique et le travail préliminaire sont fortement réduits.

Puisque l'ampleur de l'espace de dégagement est fortement influencée par la dégradation des aubes directrices et du fond supérieur, des mesures préalables de l'efficacité de turbine sur des turbines érodées de sable sont présentées. Ces mesures montrent l'importance de réduire les possibilités d'usage d'un point de vue de conception et également l'importance de réparer des surfaces exposées à l'usage.

En plus deux mesures d'efficacité sur des turbines érodées avec différent espace de dégagement sont présentées. Selon ces deux mesures, l'efficacité de la turbine est fortement influencée par l'ampleur de l'espace de dégagement, et par conséquent un calcul numérique de l'écoulement dans les aubes directrices avec quatre espaces de dégagement différentes sera présenté. Cela pour montrer comment l'écoulement de fuite est sensible au degré de l'espace de dégagement.

Introduction

The demand of energy and power is constantly increasing, and this makes it important to extract the most of the available energy potential of the stored water. To achieve this one have to emphasize the losses connected with the operation of the turbine and make use of technology which reduces the losses. The water power plants are initially designed to give a continuous production at best efficiency point. But the last few years there has been a change in this production pattern. A continuous expansion of electrical cables to neighbor countries is defining a new marked for the water power industry, where the price of electricity is the most important parameter in governing the production pattern. This involves a more fluctuating and demanding production pattern. The water power plant is now delivering electricity at full load, best efficiency point as well as at part load, all depending on the electricity price.

As opposed to the Pelton turbine, the Francis turbine is not well suited for variable load operation outside best efficiency point. Still, the Francis turbine has a higher peak efficiency than the Pelton turbine, but the efficiency curve of a Francis runner is quite steep, causing a large drop in efficiency as the operation is moved just a few percentage below best efficiency point.

The loss in a Francis turbine constitutes of different flow and friction losses, where the leakage flow between the covers and the guide vanes represents a rather large part of the main losses. A cross section of a Francis turbine and the location of the head and bottom covers are shown in figure 1. When the head and bottom covers and the guide vanes are designed it is originally made with a certain dry clearance gap to prohibit grinding. But when the turbine is pressurized the originally gap, and hence the leakage flow, increases. As illustrated in figure 2, the leakage flows from the pressure side to the suction side, disturbing the main flow and generating vortex flow, which again increases the degree of erosion.

As shown in figure 3 the efficiency is highly depending on the clearance gap, and this relation makes it vital to identify the extent of the clearance gap. It is on the basis of this knowledge one can decide how to do the proper repairs and design of head and bottom covers.

The main objective of this work is to validate the numerical 2-D simulation as a tool to predict the deflection of the head cover.

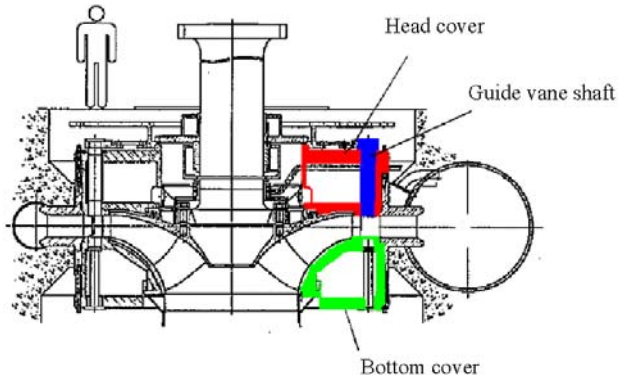

Figure 1. A cross section of a high head Francis turbine.

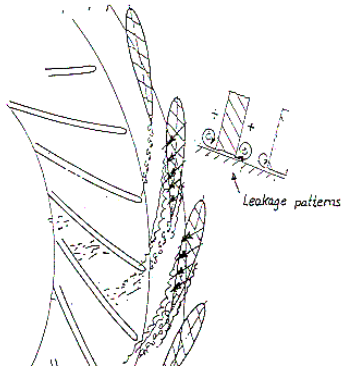

Figure 2. Leakage flow in the guide vanes. (Ref.1)

In addition to the knowledge of the deflection it is also important to gain knowledge of the gaps influence on the flow conditions in the turbine. Subsequently a CFD analysis of the flow in a guide vane with four different clearance gaps is performed to illustrate how sensitive the leakage is to the extent of the clearance gap. The net head of the chosen turbine is 525 meters and the total flow through the turbine is 64 m^3/s.

Leakage flow in the guide vanes

The leakage flow in the guide vanes is governed by the extension of the gap between the guide vanes and the covers and the pressure difference between the pressure side and suction side. When the head and bottom covers and the guide vanes are designed it is originally made with a certain clearance gap to prohibit grinding. But when the turbine is pressurized the originally gap, and hence the leakage flow, increases. The extent of the gap is mainly a function of the net head, but it is also influenced by the dimensions and the wear of the machinery.

Especially high head Francis turbines are exposed to serious wear from sand erosion due to the high velocities and accelerations. The wear of the machinery caused by sand particles in the flow can make an uneven increased gap surface between the covers and guide vanes, and further increase the gap. The erosion of the facing plates underneath the edges of the guide vanes is further enhanced by the vortex lines caused by the leakage flow. The reinforced erosion increases the gap between the guide vanes and the covers even more, which again enhances the vortex flow in the guide vanes.

As mentioned above the leakage flow is highly depending on the pressure difference between the pressure side and suction side. This pressure difference is mainly a result of the demand of a uniform flow through the guide vane and runner vane channel in order to exploit the most of the energy potential of the stored water. This demand makes the pressure difference between suction side and pressure side inevitable. Correspondingly one has to focus on how to reduce the clearance gap between the guide vane and the covers in order to reduce the leakage flow.

There have been done some experiments with different clearance gaps on the same head cover to illustrate the influence on the efficiency (Ref. 2). The results from these experiments are shown in figure 3, and it clearly illustrates that the leakage flow will be significant with a proven drop in efficiency as the gap increases. In addition there have been performed experiments with sealing strips between the covers and the guide vane facing plate to reduce the leakage flow. These results are presented in figure 4, and shows a clear improvement in the efficiency when sealing strips are used.

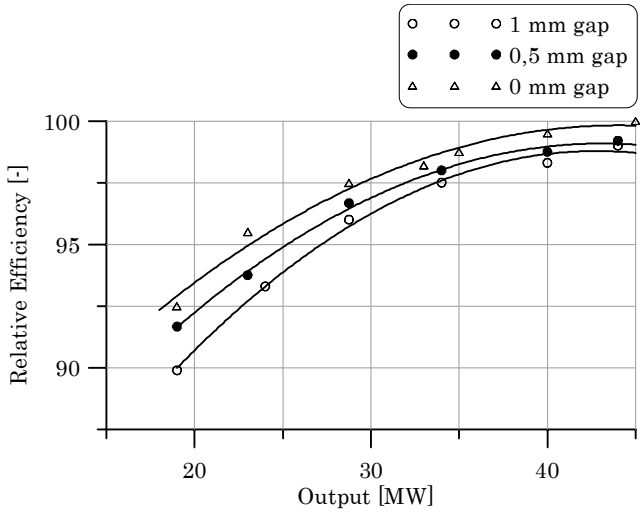

Figure 3. Efficiency test with different clearance gaps (Ref.2)

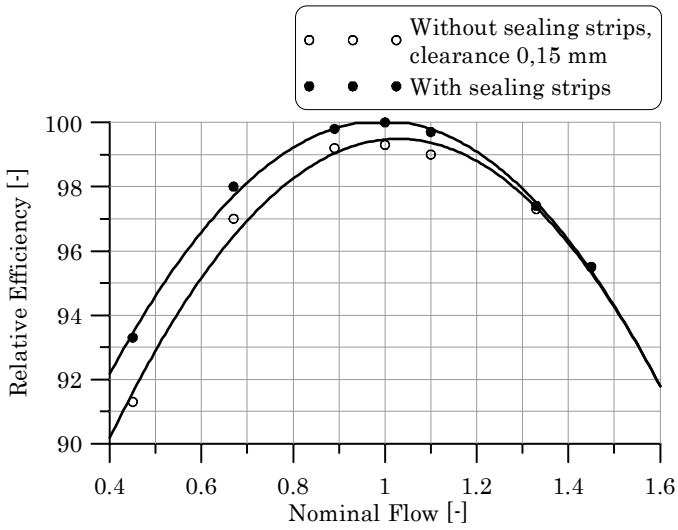

Figure 4. Efficiency measurements with and without sealing strips. (Ref.1)

Calculation of the head covers deflection by finite element method

The guide vanes and the runner blades lies between the head and bottom cover, and the main purpose of the covers are to keep the turbine together. Consequently the covers have to be quiet stiff to minimize any deformation due to the water pressure. As a consequence of this criterion the stiffness of the suggested geometry is often emphasized by performing a preliminary analytical calculation of the covers deflection.

This analytical calculation neglects the shear and bend deformation of the covers, but when the shear and bend stresses are accounted for the actual deflection is 1.5-2 times higher than the result from the simplified stress calculation (Ref. 3). A final numerical calculation is usually carried out by means of a finite element method, which will be presented below.

It should however be mentioned that the disturbance from the leakage flow reduces the efficiency even more for high head Francis turbine compared to a low head Francis. This is most likely due to the fact that the height of the guide vanes in high head turbines is much lower than for a low head turbine. Subsequently the leakage flow disturbs a larger part of the main flow. The long runner blades in high head Francis turbine also makes the runner more sensitive to local disturbance. In addition the guide vane opening for a high head Francis turbine is also smaller than for a low head turbine, making the pressure difference between pressure side and suction side larger than for a low head turbine. As a consequence of this, the design criteria of the covers for high head and low head turbines somewhat differs. And as a rule when designing the covers the angle of deflection for high head Francis turbines should be less than $5 \cdot 10^{-4}$ radians, but for low head Francis turbines it is sufficient to keep the deflection below $8 \cdot 10^{-4}$ radians (Ref. 4).

General assumptions

Most of the head covers in this paper are made with ribs with a certain thickness, where the number of ribs is equal to the number of guide vanes. In order to simulate a 2-D geometry with an acceptable value of the stiffness corresponding to the actual stiffness of the 3-D geometry, a soft area is introduced in the 2-D model in the same region where the ribs are supposed to be. In figure 5 the soft area is represented by the grey region and the solid part of the head cover is marked with black. This soft area is modelled with a somewhat lower E-module than the rest of the geometry, which is modelled with the E-module of the actual material. The calculation of the E-module at the soft region is based on how large part of the circumference the ribs occupy at certain radius, r, corresponding to the centre of mass, indicated by the arrow in figure 5:

$$E_{Soft} = \frac{X \cdot t}{2 \cdot \pi \cdot r} \cdot E_{3D}$$

where X is the number of ribs and t is the thickness of the ribs.

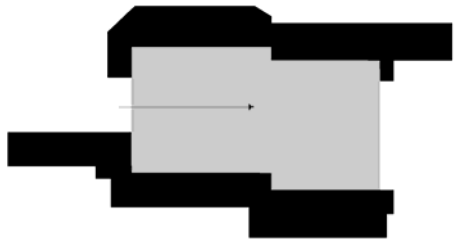

Figure 5. A 2-D model of a head cover illustrating the soft area.

Results from the finite element calculation

The main objective is to find a relation between the 3-D results and the 2-D results. Accordingly the ratio between the deflection results from the 2-D simulation and the 3-D simulation is calculated and presented in figure 6. With the exception of two points it seems like the ratio roughly lies between 0.9-1.3. In the authors opinion this is a quiet high order of accuracy, especially when regarding the extensive assumption which is made when the 2-D simulation is made.

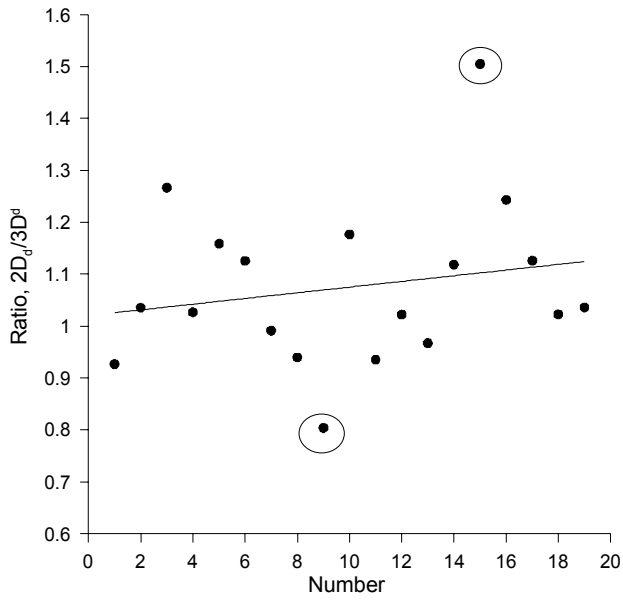

Figure 6. The ratio between the 2-D and the 3-D results.

It should also be mentioned that among the 20 head covers two of them were solid, and not made with ribs. The difference between the 2-D and 3-D result in these particular cases was less than 4%, which, not surprisingly, indicates that most of the differences between the 2-D and 3-D results are caused by the simplification of the stiffness of the 2-D geometry.

Discussion of the efficiency

The Reynolds number of a Francis turbine is described in terms of the outlet diameter, D of the runner and the velocity, v at the outlet of the runner:

$$\mathrm{Re} = \frac{v \cdot D}{\nu}$$

where μ is the kinematical viscosity of the water.

According to equation 2 the Reynolds number describes the size of the runner. The Reynolds number of the 20 Francis turbines referred to in this paper is calculated, and plotted against the best efficiency. The result is shown in figure 7 and clearly indicates that the efficiency increases by increasing Reynolds number. Thus the efficiency increases by increasing unit size. This relation can first of all be explained be regarding the friction loss in a small and large Francis turbine unit. Because a larger percentage of the flow in a small runner is in contact with the surface than in a larger runner, the friction loss in percentage is higher in a smaller unit than in a larger unit.

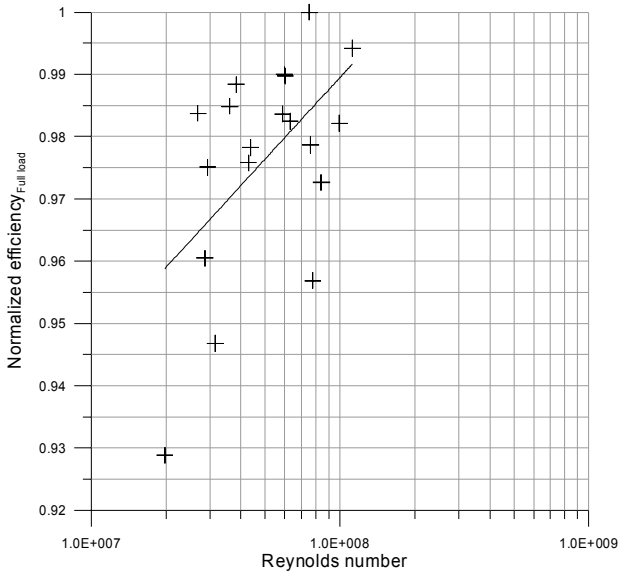

Figure 7. The efficiency at full load plotted against the Reynolds number.

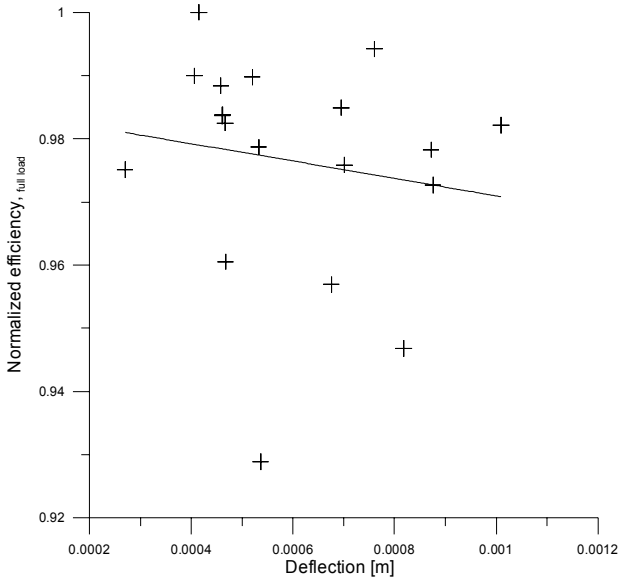

Figure 8. The normalized efficiency plotted against the deflection.

In figure 8 the efficiency at full load is plotted against the angle of deflection. This plot shows a tendency of increasing angle of deflection as the efficiency decreases. Bearing in mind the relationship between the effi-

ciency and the Reynolds number, this means that the angle of deflection increases as the turbine unit decreases, which is in accordance with the design criteria of head covers, as mentioned above.

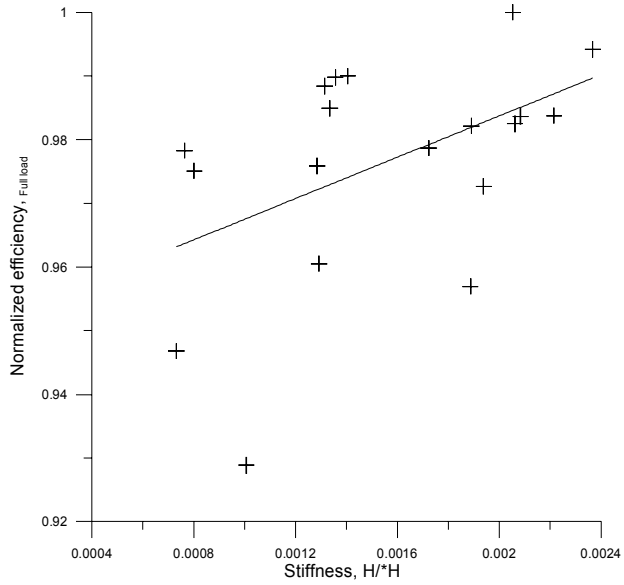

Figure 9. The efficiency plotted against the stiffness of the head cover.

Furthermore the efficiency is also plotted against the stiffness of the head cover, as shown in figure 9. And since the speed number of most of the regarded units only differs between 0.27-0.33 it is accurate to define the stiffness of the head cover as the ratio between the height of the head cover, H, and the net head, *H. And this plot indicates an increased stiffness as the efficiency increases, emphasizing the efficiency`s dependence on the covers stiffness.

It should be mentioned that in figures 6-9 a linear trend line is added to better visualize the behavior of the retrieved data.

Numerical computation of the flow in guide vanes

As mentioned in the introduction the leakage flow in the guide vane is governed by the extension of the clearance gap and the pressure drop from pressure side to suction side. The pressure drop across the guide vane facing plate is given by the design of the guide vane and stay vanes. Whereas the clearance gap between the guide vane and the covers depends on the net head, design of the covers and also the degree of erosion. The flow through the guide vane channels is highly dependent on the flow conditions at the inlet of the guide vane, making it important to gain proper knowledge of the velocity profile at the inlet of the guide vane cascade. Consequently a numerical calculation of the flow in the stay vanes is included, where the flow condition at the outlet of the stay vane cascade is used as the inlet condition at the guide vane domain. The software program Fluent has been employed to compute the flow in the guide vane. The Fluent code offers several turbulence models, but the turbulence model used was the Spalart-Allmaras model. However, to validate the chosen solver the k-ε model was also employed. But the differences in results were marginal and therefore the original turbulence

model was retained. Also, to obtain an accurate resolution of the computational domain different mesh resolutions have been generated and solved numerical for comparison.

Discussion of the result

As the flow approaches the guide vane shaft the pressure drop from pressure side to suction side is so large that a cross flow is inevitably, and the cross flow keeps increasing towards a decreasing radius. Near the leading edge the pressure drop is to low to give an evident cross flow and the flow is rather heading in the radial direction, as can be seen in the inlet region of the guide vane. This relation was also detected by Xin Cheng in her thesis, where measurements showed no leakage flow near the leading edge, but an increasing leakage from mid-chord to the trailing edge was detected (Ref. 5).

The guide vane shaft acts as an obstacle to the flow in the clearance gap. And close to the shaft the leakage flows alongside the circular shaft, giving rise to a vortex flow in the region where the leakage from the right and left side of the shaft meets. In addition a vortex flow at the upper right side of the shaft is also detected in figure 12. In this region the cross flow interacts with the radial flow in the clearance gap, giving rise to a vortex flow.

Still, the disturbance on the main flow at the pressure side is not as evident as the influence on the main flow at the suction side. The disturbance at the trailing edge on the suction side causes a non-uniform velocity profile at the inlet of the runner vane cascade, as shown in figure 13.

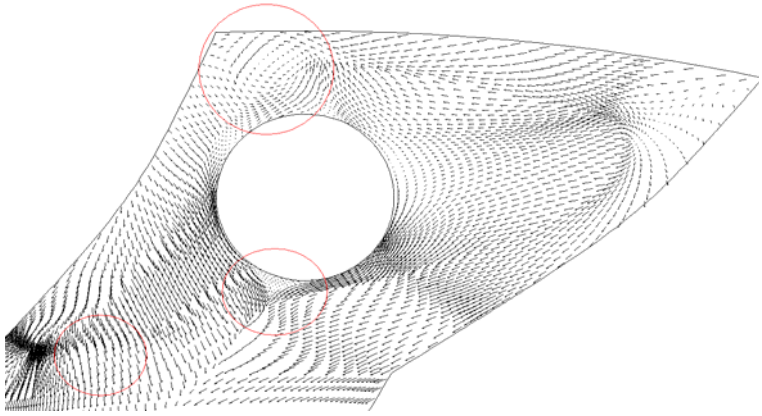

Figure 10. Leakage flow at the head cover facing plate, 4 mm clearance.

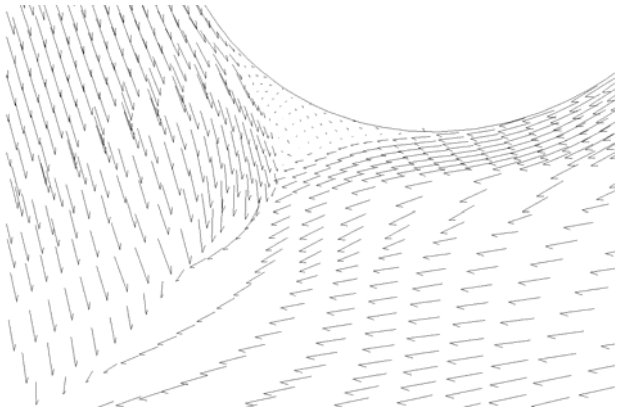

Figure 11. Vortex flow in the vicinity of the guide vane shaft, 4 mm clearance.

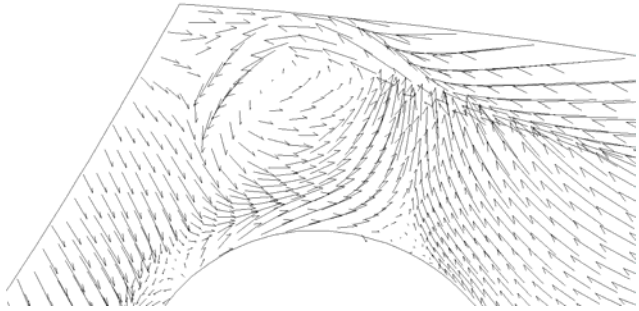

Figure 12. Secondary flow at the pressure side, 4 mm clearance.

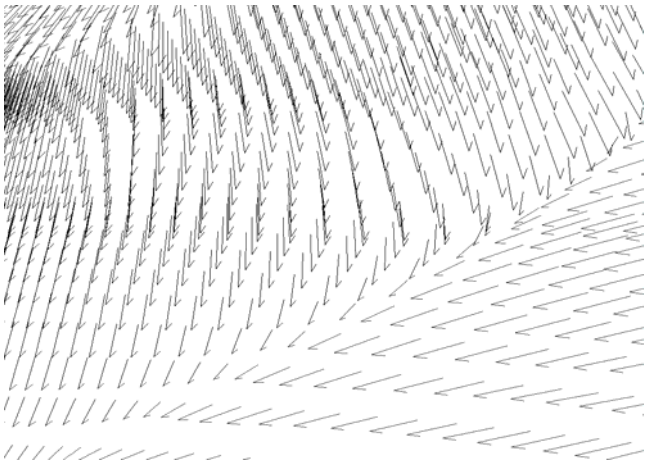

Figure 13. Disturbance from the leakage flow at the trailing edge of the suction side, 4 mm clearance.

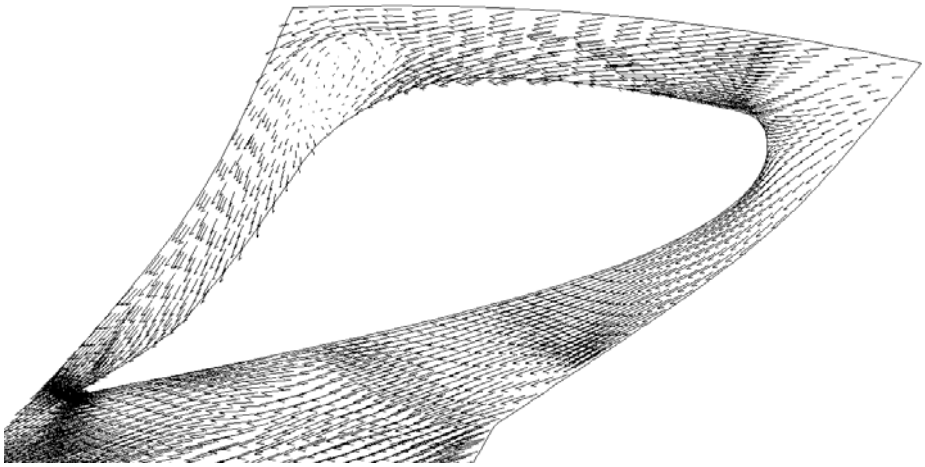

Figure 14. The velocity profile 2 cm from the guide vane facing plate, 4 mm clearance.

Even 2 cm from the guide vane facing plate one can see a clear disturbance on the main flow, as illustrated in figure 14. However, in the middle of the guide vane channel the main flow is not effected by the leakage flow, as can be seen from figure 15.

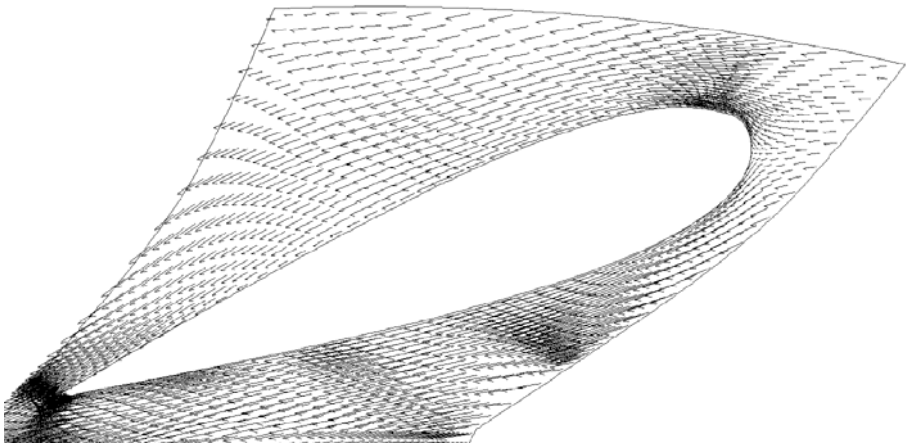

Figure 15. The velocity profile in the middle of the guide vane channel, 4 mm clearance.

Since the efficiency is highly depending on the extent of the clearance gap, a numerical calculation of the flow in guide vanes with four different gaps corresponding to 0.25 mm, 1 mm, 2 mm and 4 mm has been performed.

In figure 17 and 18 the leakage flow in respectively 4 mm and 0.25 mm sized gaps are illustrated. The vortex flow at the largest gap is fully developed and disturbs a rather large part of the main flow. As opposed to the vortex flow in the largest gap, the vortex flow in the smallest gap is barely recognizable, and only a small part of the main flow is influenced by this secondary flow. These results clearly states the importance of keeping the clearance gap between the guide vanes and the covers as small as possible due to the influence from the vortex flow.

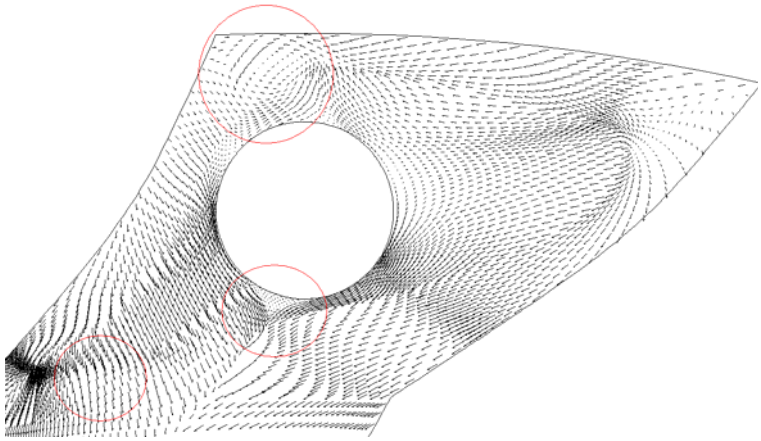

Figure 17. Leakage flow at the head cover facing plate with 4 mm clearance gap.

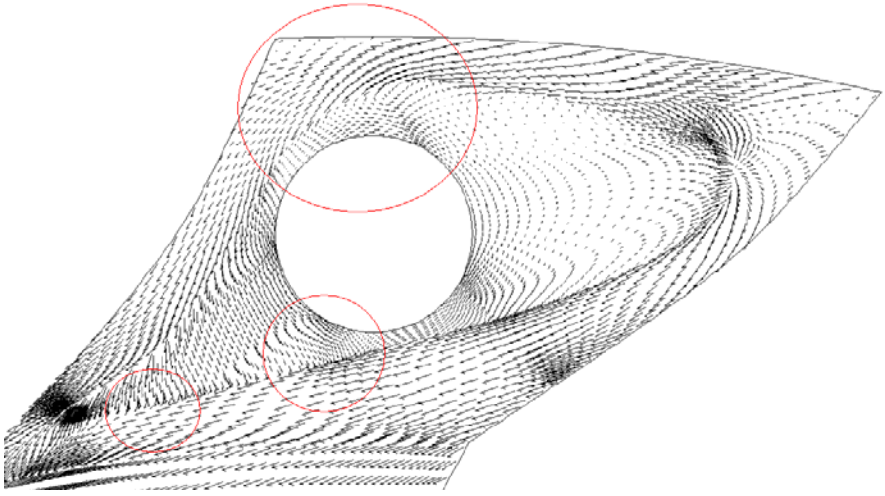

Figure 18. Leakage flow at the head cover with 0.25 mm clearance gap.

Conclusion

A 2-D simulation of the head covers deflection has been proven to be sufficient without a significant loss in accuracy. First of all this numerical 2-D tool makes it easy to do changes in the already suggested geometry in order to calculate deflections at different dimensions. Secondly, the demand of computer power is noticeable reduced by the use of a 2-D model instead of a 3-D model.

Measurements of the efficiency at different clearance gaps show that the efficiency is highly depending on the extent of the clearance gap. The results from the numerical computation of the leakage flow in guide vanes at different clearance gaps shows that in addition to the increased leakage flow, the extent of the vortex flow is enhanced as the clearance gap increases, both resulting in a lower efficiency.

To minimize the leakage flow smallest possible clearance gap is recommended in general to avoid or at least reduce the vortex flow, which enhances sand erosion. But when the erosion is a fact, installation of guide vane seals in order to prevent the leakage flow will reduce the erosion until the turbulence and secondary flow erosion has created a waviness surface between the seals and the facing plates. Such waviness surface may cause dangerous galling between the seals and the facing plates and therefore cause a reduction of the reliability of the turbine.

The conclusion is to keep the deflection at a minimum level to avoid vortex flow, which enhances erosion in sand laden water. Development of new stronger materials and in particular new ceramic materials, which can be used as coating on the facing plates will be crucial in reducing the leakage flow in the guide vanes.

REFERENCES

Ref. 1 Hermod Brekke, “Inspection of the guide vanes of the turbines installed in Svartisen propellant”, Lecture V.R Burgeon, Norway 1991.

Ref. 2 Hermod Brekke, "The influence from Guide Vane Clearance Gap on Efficiency and Scale Effect for Francis Turbines", 14th I.A.H.R Symposium, 20-23 June 1988, Trondheim.

Ref. 3 Geir Holm, 1994, "The influence from the guide vanes clearance gap on the efficiency scale effect in high head Francis turbines", A project work written in Norwegian at The Norwegian University of Science and Technology.

Ref. 4 Hermod Brekke, Konstruksjon av pumper og turbiner. NTNU, Trondheim, 1998.

Ref. 5 Xin Cheng, Theoretical and experimental study of flow through the double cascade of a Francis turbine. A Ph.D thesis at the Norwegian Institute of Technology, 1992, Trondheim.